

Aerosol characteristics and particle production in the upper troposphere over the Amazon Basin

Meinrat O. Andreae^{1,12}, Armin Afchine², Rachel Albrecht³, Bruna Amorim Holanda¹, Paulo Artaxo⁴, Henrique M. J. Barbosa⁴, Stephan Borrmann¹, Micael A. Cecchini^{5,3}, Anja Costa², Maximilian Dollner^{9,13}, Daniel Fütterer⁶, Emma Järvinen¹⁰, Tina Jurkat⁶, Thomas Klimach¹, Tobias Konemann¹, Christoph Knöte⁹, Martina Krämer², Trismono Krisna⁸, Luiz A. T. Machado⁵, Stephan Mertes⁷, Andreas Minikin^{6,16}, Christopher Pöhlker¹, Mira L. Pöhlker¹, Ulrich Pöschl¹, Daniel Rosenfeld¹⁴, Daniel Sauer⁶, Hans Schlager⁶, Martin Schnaiter¹⁰, Johannes Schneider¹, Christiane Schulz¹, Antonio Spanu^{6,13}, Vinicius B. Sperling⁵, Christine Voigt^{6,15}, Adrian Walser^{9,6}, Jian Wang^{1,11}, Bernadett Weinzierl^{6,13}, Manfred Wendisch⁸, and Helmut Ziereis⁶

¹Biogeochemistry, Multiphase Chemistry, and Particle Chemistry Departments, Max Planck Institute for Chemistry, Mainz, Germany

²Forschungszentrum Jülich, Jülich, Germany

³Instituto de Astronomia, Geofísica e Ciências Atmosféricas, Universidade de São Paulo, São Paulo, Brazil

⁴Institute of Physics, University of São Paulo, São Paulo, Brazil

⁵National Institute for Space Research (INPE), São José dos Campos, Brazil

⁶German Aerospace Center (DLR), Institute of Atmospheric Physics (IPA), Weßling, Germany

⁷Leibniz Institute for Tropospheric Research, 04318 Leipzig, Germany

⁸Leipzig Institute for Meteorology, Leipzig University, Leipzig, Germany

⁹Meteorological Institute, Ludwig Maximilian University, Munich, Germany

¹⁰Institute for Meteorology and Climate Research, Karlsruhe Institute of Technology, Karlsruhe, Germany

¹¹Brookhaven National Laboratory, Upton, New York, USA

¹²Scripps Institution of Oceanography, University of California San Diego, La Jolla, California, USA

¹³University of Vienna, Aerosol Physics and Environmental Physics, Wien, Austria

¹⁴Institute of Earth Sciences, The Hebrew University of Jerusalem, Israel

¹⁵Institute of Atmospheric Physics (IPA), Johannes Gutenberg University, Mainz, Germany

¹⁶German Aerospace Center (DLR), Flight Experiments, Oberpfaffenhofen, Germany

Abstract

Airborne observations over the Amazon Basin showed high aerosol particle concentrations in the upper troposphere (UT) between 8 and 15 km altitude, with number densities (normalized to standard temperature and pressure) often exceeding those in the planetary boundary layer (PBL) by one or two orders of magnitude. The measurements were made during the German-Brazilian cooperative aircraft campaign ACRIDICON-CHUVA on the German High Altitude and Long Range Research Aircraft (HALO). The campaign took place in September–October 2014, with the objective of studying tropical deep convective clouds over the Amazon rainforest and their interactions with atmospheric trace gases, aerosol particles, and atmospheric radiation.

Aerosol enhancements were observed consistently on all flights during which the UT was probed, using several aerosol metrics, including condensation nuclei (CN) and cloud condensation nuclei (CCN) number concentrations and chemical species mass concentrations. The UT particles differed in their chemical composition and size distribution from those in the PBL, ruling out convective transport of combustion-derived particles from the BL as a source. The air in the immediate outflow of deep convective clouds was depleted of aerosol particles, whereas strongly enhanced number concentrations of small particles (<90 nm diameter) were found in UT regions that had experienced outflow from deep convection in the preceding 5–72 hours. We also found elevated concentrations of larger (>90 nm) particles in the UT, which consisted mostly of organic matter and nitrate and were very effective CCN.

Our findings suggest a conceptual model, where production of new aerosol particles takes place in the UT from biogenic volatile organic material brought up by deep convection, which is converted to condensable species in the UT. Subsequently, downward mixing and transport of upper tropospheric aerosol can be a source of particles to the PBL, where they increase in size by the condensation of biogenic volatile organic compound (BVOC) oxidation products. This may be an important source of aerosol particles for the Amazonian PBL, where aerosol nucleation and new particle formation has not been observed. We propose that this may have been the dominant process supplying secondary aerosol particles in the pristine atmosphere, making clouds the dominant control of both removal and production of atmospheric particles.

1. Introduction

Aircraft measurements in the upper troposphere (UT) have consistently shown large regions with very high aerosol particle number concentrations, typically in the tens of thousands of particles per cm^3 , with the strongest enhancements reported in tropical and subtropical regions (Clarke et al., 1999; Andreae et al., 2001; de Reus et al., 2001; Krejci et al., 2003; Lee et al., 2003; Young et al., 2007; Ekman et al., 2008; Yu et al., 2008; Froyd et al., 2009; Weigelt et al., 2009; Borrmann et al., 2010; Clarke and Kapustin, 2010; Mirme et al., 2010; Ekman et al., 2012; Waddicor et al., 2012; Reddington et al., 2016; Rose et al., 2017). Twohy et al. (2002) observed particle concentrations up to $45,000 \text{ cm}^{-3}$ in the UT over North America and suggested that they had been formed in situ from gas-phase precursors brought up by deep convection. Weigel et al. (2011) found similar concentrations in the UT over tropical America, Africa, and Australia,

74 which they attributed to new particle formation from sulfuric acid and possibly organics. Most of
75 these elevated aerosol concentrations are in the nucleation and Aitken mode size ranges, i.e., at
76 particle diameters smaller than about 90 nm, with maxima typically between 20 and 60 nm (e.g.,
77 de Reus et al., 2001; Lee et al., 2003; Weigel et al., 2011; Waddicor et al., 2012). They generally
78 occur as layers of a few hundred to thousand meters in thickness, often extending over large hor-
79 izontal distances, and they are found over continents as well as over the most remote oceanic re-
80 gions. The high concentrations of these aerosols in the UT are of great significance for the cli-
81 mate system, because they make this region an important reservoir of particles for the transport
82 either downward into the planetary boundary layer (PBL) (Clarke et al., 1999; Clarke et al.,
83 2013; Wang et al., 2016a) or upward into the Tropical Transition Layer (TTL) and the lower
84 stratosphere (Brock et al., 1995; Weigel et al., 2011; Randel and Jensen, 2013), where they can
85 grow into the optically and cloud-microphysically active size range.

86 Based on observations over the remote Pacific and supported by extensive subsequent in-
87 vestigations, Clarke and coworkers proposed an aerosol life cycle model in which convection
88 lifts boundary layer air with nucleation precursor molecules into the upper troposphere, where
89 nucleation takes place in the detrainment zone, followed by aerosol growth and descent through
90 the troposphere into the boundary layer (Clarke, 1992; Clarke, 1993; Clarke et al., 1998). These
91 measurements were carried out over the oceans and implied sulfuric acid, likely from dimethyl
92 sulfide and sulfur dioxide oxidation, as the molecule driving aerosol nucleation. Clarke and
93 Kapustin (2002) wrote that "the tropics commonly have low aerosol mass but very high number
94 concentrations in the upper free troposphere (FT) that appear to form from sulfuric acid (nuclea-
95 tion) in convective regions and near cloud edges. These age and subside to become effective
96 cloud condensation nuclei (CCN) when mixed into the marine boundary layer."

97 When enhanced particle concentrations in the accumulation mode (larger than about 90
98 nm) have been observed, the enrichment was frequently attributed to sources of sulfur dioxide
99 (SO_2) and other combustion emissions, especially biomass burning (BB), based on correlations
100 with combustion tracers, such as carbon monoxide (CO), and air mass trajectories (e.g., Andreae
101 et al., 2001; Clarke and Kapustin, 2010; Weigel et al., 2011; Clarke et al., 2013). After having
102 been lofted to the UT by deep convection, particles in this size range can be transported over
103 hemispheric distances, because removal processes are very inefficient at these altitudes (Andreae
104 et al., 2001; Clarke and Kapustin, 2010).

The enhanced particle concentrations in the ultrafine (UF) size range (here defined as particles smaller than 90 nm), on the other hand, cannot be explained by transport from the lower troposphere, since they far exceed typical concentrations in the PBL and generally are too short-lived to survive deep convection and long-range transport. Therefore, nucleation and new particle formation (NPF) from gas phase precursors brought into the UT by the outflow from deep convection have been proposed as the source of these enhanced particle concentrations (Clarke et al., 1999; Twohy et al., 2002; Krejci et al., 2003; Lee et al., 2003; Young et al., 2007; Froyd et al., 2009; Merikanto et al., 2009; Weigel et al., 2011; Waddicor et al., 2012). High actinic flux, low preexisting aerosol surface area, and low temperatures make the UT an environment that is highly conducive to nucleation and NPF.

The nature of the gaseous species involved in particle nucleation and growth has been the subject of some debate (Kulmala et al., 2006). Most of the earlier papers attributed the nucleation to H_2SO_4 in combination with H_2O and NH_3 , especially in marine and anthropogenically influenced regions, where a sufficient supply of sulfur gases from either DMS oxidation or pollution sources is available (e.g., Clarke et al., 1999; Twohy et al., 2002; Lee et al., 2003; Merikanto et al., 2009). However, there is growing evidence that, in most cases, there is not enough H_2SO_4 available to explain the observed rates of growth. Therefore, the condensation of organics has been proposed to dominate particle growth after nucleation, especially over unpolluted vegetated areas such as the Amazon Basin (Ekman et al., 2008; Weigel et al., 2011; Waddicor et al., 2012; Murphy et al., 2015).

In fact, H_2SO_4 does not even have to be the initially nucleating species in all cases. Recent studies conducted as part of the Cosmics Leaving OUtdoor Droplets (CLOUD) project have shown that organic vapors alone can produce particle nucleation (Kirkby et al., 2016) and that nearly all nucleation throughout the present-day atmosphere involves ammonia or biogenic organic compounds (Dunne et al., 2016). Highly oxygenated multifunctional organic compounds (HOMs) formed by ozonolysis of α -pinene were found to nucleate aerosol particles, especially when aided by ions. Extremely low volatility organic compounds (ELVOCs, which may be at least in part identical to HOMs) are also produced from the O_3 - or OH-initiated oxidation of biogenic volatile organic compounds (BVOCs) (Jokinen et al., 2015). Following nucleation by the lowest-volatility species, with increasing particle size the condensation of progressively more volatile compounds is facilitated by the decrease in the Kelvin effect (Tröstl et al., 2016). These

laboratory studies were confirmed by field observations at a mountain site in the free troposphere, where NPF was found to take place through condensation of HOMs, in this case from anthropogenic precursor VOCs, within 1–2 days after being lofted from the PBL (Bianchi et al., 2016).

The production of particles in the UT may be a key component of the atmospheric budget of optically and cloud-microphysically active aerosols, especially in pristine or relatively unpolluted regions, as was suggested in a modeling study by Merikanto et al. (2009). Studies in the Amazon have shown that NPF almost never takes place under clean conditions in the PBL over the Amazon Forest (Zhou et al., 2001; Martin et al., 2010; Andreae et al., 2015) and rarely occurs over the taiga forest in remote Siberia (Heintzenberg et al., 2011). Over the Amazon, downward transport of aerosols from the free troposphere (FT) has been identified as an important, if not the dominant, source of particles to the lower troposphere (LT) (Zhou et al., 2001; Roberts and Andreae, 2003; Wang et al., 2016a). In turn, the concentrations of aerosols in the PBL have a pronounced influence on the characteristics of convection and thereby influence cloud radiative forcing and atmospheric dynamics (Sherwood, 2002; Rosenfeld et al., 2008; Fan et al., 2012; Rosenfeld et al., 2014; Stolz et al., 2015; Cecchini et al., 2017).

Understanding the processes that control the aerosol burden in the pristine atmosphere is an essential prerequisite for assessing the magnitude of the climate forcing by anthropogenic aerosols, since it forms the baseline from which anthropogenic forcing is derived. Because of the strong non-linearity of the relationship between particle number concentration and cloud-mediated aerosol effects, the uncertainty regarding the aerosol burden of the pristine atmosphere is the largest contributor to the uncertainty in estimates of anthropogenic aerosol climate forcing (Carslaw et al., 2013; Carslaw et al., 2017). For example, model calculations suggest that the inclusion of ion-induced particle formation from biogenic HOMs in the natural atmosphere reduces the cloud-albedo radiative forcing by about one-third because of the higher albedo calculated for the clouds in the pre-industrial atmosphere (Gordon et al., 2016).

In this paper, we present the results of aerosol measurements made in the upper troposphere across the Amazon Basin during the ACRIDICON–CHUVA campaign on the German HALO aircraft during September and October 2014 (Wendisch et al., 2016). ACRIDICON

stands for “Aerosol, Cloud, Precipitation, and Radiation Interactions and Dynamics of Convective Cloud Systems”; CHUVA is the acronym for “Cloud Processes of the Main Precipitation Systems in Brazil: A Contribution to Cloud Resolving Modeling and to the GPM (Global Precipitation Measurement)”. We characterize these UT aerosol particles in terms of their microphysical and chemical properties, and contrast them with the LT aerosols. From their spatial distribution and their relationship to deep convection and convective outflow, we derive hypotheses about their mode of formation. Finally, we discuss the role of upper tropospheric aerosol formation in the life cycle of the atmospheric aerosol.

2. Methods

The observations discussed in this paper were collected aboard the HALO aircraft (<http://www.halo.dlr.de/>), a modified Ultra Long Range Business Jet G 550 (manufactured by Gulfstream, Savannah, USA). Because of its high ceiling altitude (up to 15 km) and long endurance (up to eight hours with a scientific payload), HALO is capable of collecting airborne measurements of cloud microphysical and radiative properties, aerosol characteristics, and chemical tracer compounds in the upper troposphere, in and around tropical deep convective clouds. The aircraft and its instrumentation are described in the ACRIDICON–CHUVA overview paper by Wendisch et al. (2016).

In-situ meteorological and avionics data were obtained at 1 Hz from the BASeic HALO Measurement And Sensor System (BAHAMAS). This data set includes pressure, temperature, wind direction and speed, humidity, water vapor mixing ratio, aircraft position, and altitude. All concentration data have been normalized to standard temperature and pressure ($T = 273.15$ K and $p = 1000$ hPa).

2.1. The HALO aerosol submicrometer inlet (HASI)

All aerosol sampling was conducted using the HALO aerosol submicrometer inlet (HASI), designed for HALO by the German Aerospace Center (DLR) in collaboration with enviroscope GmbH (Frankfurt, Germany) with the aim of providing up to 30 l min^{-1} sample air flow (divided over four sample lines) to aerosol instruments mounted inside the aircraft cabin. HASI samples the air on top of the fuselage outside of the aircraft boundary layer. The air stream is

aligned in the inlet using a front shroud and decelerated by a factor of approximately 15. Four sample tubes with 6.2 mm outer diameter and frontal diffusors protrude into the decelerated air stream. The design goal is to allow regulating the sample airflow in each of the four sample lines to achieve isokinetic sampling conditions according to the actual speed of the aircraft. Since the automatic adjustment had not been implemented at the time of the field experiment, the flow was fixed to values providing near-isokinetic sampling for typical flight conditions based on geometric considerations and preliminary flow simulations for the initial design of the inlet. The geometric design should prevent large cloud droplets and ice crystals from entering the sample lines directly. The inlet position is located in the shadow zone for larger ice crystals, which precludes artifacts by shattering and break-up of larger ice particles at the inlet tip (Witte, 2008). Judging from the first measurements with HASI, it appears that measurements of interstitial aerosol in liquid clouds are affected by artifacts, while in ice clouds there is no indication for such artifacts. The data selection procedures to exclude artifacts are discussed in section 2.2.

2.2. Condensation nuclei

Condensation nuclei (CN) number concentrations (N_{CN}) were measured using the Aerosol Measurement System (AMETYST). This system was designed to provide an instrument package for HALO to measure basic microphysical properties of the ambient atmospheric aerosol (integral number concentration, sub-micrometer size distribution, fraction of non-volatile particles, and particle absorption coefficient). AMETYST includes four butanol-based condensation particle counters (CPCs, modified Grimm CPC 5.410 by Grimm Aerosol Technik, Ainring, Germany) with flow rates of 0.6 and 0.3 l min⁻¹, configured with different nominal lower cutoff diameters at 4 nm and 10 nm (set via the temperature difference between saturator and condenser). In addition, two differential mobility analyzers (Grimm M-DMA) with a nominal size range between 5.5 and 350 nm using ²⁴¹Am radioactive sources as aerosol neutralizers are part of the system.

Two of the four CPCs are generally set to measure the integral particle concentrations, while for the two other CPCs the configuration is selectable depending on measurement priorities. They can be used either as detectors for the DMAs or for additional integral concentration measurements. The DMAs can either be set to select specific diameters or operated as a DMPS (differential mobility particle sizer) system scanning the size distribution at predefined diameter

steps. The integration times at each step have to be chosen such that meaningful statistics can be achieved depending on the measurement strategy. AMETYST also includes an optional thermodenuder, which heats a section of the sample line to 250°C for the measurement of the non-volatile particle fraction.

The raw CPC data are corrected using an empirical, pressure-dependent flow correction to account for changes in the volume flow at different flight altitudes (D. Fütterer, PhD thesis, in preparation). Particle losses in the sampling lines have been estimated with the particle loss calculator by von der Weiden et al. (2009). Accounting for these effects leads to an increase of the effective cutoff diameter for all CPCs. The effective cutoffs are calculated as a convolution of the pressure-dependent CPC counting efficiency and the size-dependent transmission efficiency of the sample lines. The data reported here were taken by the CPC operated at 0.6 l min⁻¹, with a nominal cutoff of 4 nm. Due to inlet losses, the effective cutoff diameter increases to 9.2 nm at 1000 hPa, 11.2 nm at 500 hPa, and 18.5 nm at 150 hPa. This implies that the present setup of AMETYST essentially does not detect nucleation mode particles below 10 nm at low altitudes and below 20 nm in the UT. Typical uncertainties of CPC number concentration measurements are estimated to be of the order of 5 to 10% (Petzold et al., 2011).

To eliminate artifacts from cloud hydrometeors and bias from local pollution, we excluded measurements using the following criteria: (1) All cloud passages below 6 km were removed. During passages through water clouds, the CPCs showed erratic, unreasonably high number concentrations that are probably caused by droplet shattering at the probe tip. Cloud passages were identified from the observation of elevated concentrations of particles >3 µm using the hydrometeor probes (see below). (2) In the mixed phase and ice phase regimes, all cloud passages were inspected for possible shattering artifacts, and suspect data were rejected. Cloud passages through pure ice clouds did not show evidence of hydrometeor shattering. (3) The flight segments during departure and approach to Manaus airport were removed to avoid pollution from the airport and its surroundings. (4) Flights segments through the Manaus urban plume, which was sampled during joint flight experiments with the DOE G1 aircraft and in the course of tracer studies in the PBL, were excluded in order to provide a sampling representative of the dry season atmosphere over the Amazon Basin away from local pollution. (5) Fire plumes that were sampled deliberately to study fresh emissions were not analyzed for this paper. (6) Segments where the aircraft passed through its own exhaust were also excluded from the analyzed data set.

2.3. Aitken mode aerosol size spectra

To obtain aerosol size spectra for particle sizes up to 300 nm, the DMAs within AMETYST were connected to two of the CPCs and operated in scanning mode for selected flight sequences (especially during longer flight legs, where relatively homogeneous conditions can be assumed). The size range covered by the scans was typically between 20 and 300 nm diameter in nine steps. To improve the time resolution, the two DMPS were usually set to scan the same sequence in opposite direction. The DMPS data were then analyzed by taking into account a correction for multiple charges following Wiedensohler (1988) after correcting the measured concentrations to standard atmospheric conditions. To derive modal parameters for the particle size distribution, a bi-modal log-normal fit to the data points was computed.

2.4. Accumulation mode aerosol particles

For the purposes of this paper, we define the accumulation mode as the particle size range from 90 nm to 600 nm and the total number concentration in this size class as the accumulation mode number concentration, N_{acc} . The particle concentrations in this range were measured with an optical particle counter (OPC), the Ultra High Sensitivity Aerosol Spectrometer (UHSAS; Droplet Measurement Technologies, Inc., Longmont, CO) (Cai et al., 2008; Brock et al., 2011). The UHSAS combines a high-power infrared laser ($\lambda=1054$ nm) and a large solid angle range in sideways direction for the detection of light scattered by individual particles. Due to the resulting almost monotonic increase of instrument response with particle size, the UHSAS enables high-resolution measurements (100 selectable channels). The high laser intensity enables the detection of particle diameters down to about 60 nm, with the upper limit being approximately 1 μm . Due to changes in the laser and instrument parameter settings during the campaign, only the size range from ~ 90 nm to ~ 600 nm is considered here. Particle concentrations of up to 3000 cm^{-3} are recorded without significant counting coincidence losses (Cai et al., 2008). The airborne instrument version is mounted in an under-wing canister and equipped with a forward facing diffusor inlet. The slowed airflow is subsampled by a second inlet at approximately isokinetic conditions. The sample is not actively dried before the measurement, but due to combined heating effects the measured diameters can be assumed to be close to their dry diameters (Chubb et al., 2016). The UHSAS was calibrated with monodisperse polystyrene latex (PSL) spheres of known refractive

index and size. The evaluation of the OPC calibration results and the derivation of realistic uncertainty estimates for the OPC size distributions is outlined in a recent study by Walser et al. (2017).

2.5. Cloud condensation nuclei

The number concentration of CCN (N_{CCN}) was measured with a continuous-flow stream-wise thermal gradient CCN counter (CCNC, model CCN-200, DMT, Longmont, CO, USA) (Roberts and Nenes, 2005; Rose et al., 2008). The CCN-200 consists of two columns, in which particles with critical supersaturations (S) above a preselected value are activated and form water droplets. Droplets with diameters $\geq 1 \mu\text{m}$ are detected by an OPC at the exit of the column. The inlet flow rate of the column was 0.5 l min^{-1} with a sheath-to-aerosol flow ratio of 10. The water pump was operated at the CCNC setting of “high” liquid flow. Variations in ambient pressure have a strong influence on S inside the CCNC. For this purpose, a novel constant pressure inlet without significant particle losses was deployed on HALO. The instrument was calibrated before, during, and after the campaign at different pressures and flow rates according to Rose et al. (2008). For the data used in this study, we sampled from the HASI inlet and measured at $S = 0.52 \pm 0.05\%$ and a time resolution of 1 Hz.

Since the flow in the instrument was kept constant for the data used here, the error in S was dominated by the calibration uncertainty, as described by M. Pöhlker et al. (2016); it is estimated to be in the range of 10%. According to Krüger et al. (2014), the error in N_{CCN} is based on the counting error of the measured particle number and is 10% of N_{CCN} for large concentrations; given that mostly low concentrations prevailed, the mean error was about 20% of N_{CCN} .

2.6. Cloud droplet and ice particle measurements

While measurements of liquid water and ice hydrometeor concentrations are not a subject of this paper, they were used to determine whether the aircraft was sampling inside clouds and if so, whether the cloud particles were liquid or frozen. For this purpose, we used data from the Cloud Droplet Probe (CDP) and the Cloud and Aerosol Spectrometer (CAS-DPOL), both of which are based on the principle of forward scattering detection. The CDP detects particles with sizes from $3 \mu\text{m}$ to $50 \mu\text{m}$, and classifies them into size histograms of bin widths between 1 and $2 \mu\text{m}$. The CAS-DPOL covers the size range of $0.6\text{--}50 \mu\text{m}$ in 17 bins of varying width. The

probes are described in Voigt et al. (2017) and probes and data correction techniques in Weigel et al. (2016).

Information regarding the ice particle properties was obtained from the Particle Habit Imaging and Polar Scattering Probe (PHIPS-HALO), a single-particle cloud probe that measures microphysical and angular light scattering properties of individual particles (Abdelmonem et al., 2016). The instrument is composed of a stereoscopic imager that takes two brightfield images from the particles under a viewing angle difference of 120° . Simultaneously to collecting the images, the scattering component of the instrument measures the angular scattering function of the particles from 18° to 170° with an angular resolution of 8° . The optical resolution of the imager is about $2.5\text{ }\mu\text{m}$.

2.7. Aerosol mass spectrometer

For in-situ chemical analysis of submicrometer aerosol particles a compact time-of-flight aerosol mass spectrometer (C-ToF-AMS) (Drewnick et al., 2005; Schmale et al., 2010) was operated onboard HALO. The C-ToF-AMS was sampling from the HASI inlet for ambient aerosol measurements. The aerosol particles enter the instrument via a pressure-controlled inlet and are focused into a narrow beam by an aerodynamic lens. In the vacuum chamber, the particles are flash-vaporized and the resulting gas-phase molecules are ionized by electron impact. The ions are guided into the Time-of-Flight mass spectrometer, separated by their mass-to-charge ratio, and detected by a microchannel plate detector. The C-ToF-AMS was operated with a time resolution of 30 seconds, providing mass concentrations of particulate organics, nitrate, sulfate, chloride, and ammonium.

2.8. Refractory black carbon

An eight-channel Single Particle Soot Photometer (SP2; Max Planck Institute for Chemistry) was used to detect and quantify refractory black carbon (rBC) particles using laser-induced incandescence (Stephens et al., 2003; Schwarz et al., 2006). The instrument measures the time-dependent scattering and incandescence signals produced by individual aerosol particles when crossing a Gaussian-shaped laser beam (Nd:YAG; $\lambda = 1064\text{ nm}$). The particles containing rBC cores absorb the laser light and evaporate within the optical chamber emitting thermal radiation

(incandescence). The peak intensity of the incandescence signal, recorded by two photomultiplier tubes over two different wavelength intervals, is linearly proportional to the mass of the rBC in the particle (Laborde et al., 2013). At the detector settings used, the instrument is sensitive to rBC cores in the nominal size range of 70–500 nm mass-equivalent diameter, assuming a density of 1.8 g cm^{-3} . The SP2 also detects the intensity of the light scattered by the particles using an avalanche photo-detector in order to determine the optical size of purely scattering particles in the diameter range of 200–400 nm.

The SP2 incandescence signal was calibrated several times (at the beginning, during, and at the end of the campaign) using size-selected fullerene soot particles. The scattering signal was calibrated using either spherical polystyrene latex size standards (208, 244, and 288 nm) or ammonium sulfate particles of different diameters selected by a differential mobility analyzer (DMA).

2.9. Trace gases

Ozone (O_3) was measured by a dual-cell ultraviolet (UV) absorption detector (TE49C, Thermo Scientific) operating at a wavelength of 254 nm. Signal differences from a cell with the sample air and a parallel cell with ozone-scrubbed air are used to infer the concentration of O_3 . Sample air was drawn into the instruments through the standard HALO gas inlet via a Teflon PFA line using an external pump at a nominal flow rate of 1 l min^{-1} . The calibration of the instrument is traceable to the O_3 standard of the Global Atmosphere Watch station at Hohenpeißenberg, Germany. The data output of the instrument is corrected for the temperature and pressure in the absorption cells. The precision of the O_3 measurements is 2% or 1 ppb, whichever is larger, the accuracy is 5%. Details on the use of this instrument can be found in Huntrieser et al. (2016).

Carbon monoxide (CO) was detected with a fast-response fluorescence instrument (AL5002, Aerolaser, Garmisch, Germany) (Gerbig et al., 1999). The detection of CO is based on the excitation of CO at 150 nm using a CO_2 resonance UV lamp. The fluorescence light is detected by a UV-sensitive photomultiplier. The CO detector was calibrated in-flight using onboard calibration and zero gas sources. Data are recorded at 1 Hz. The precision and accuracy are 3 ppb and 5%, respectively.

Nitrogen monoxide (NO) and total reactive nitrogen (NO_y) were measured by a dual-channel chemiluminescence detector (CLD-SR, Eco Physics). For the NO_y channel, the chemiluminescence detector is combined with a custom-built Au converter which reduces all oxidized reactive nitrogen species to NO (Ziereis et al., 2000). Detection of ambient NO is performed via reaction with O₃ in a chamber and the luminescence signal of the excited NO₂ produced by this reaction. Both detector channels are equipped with a pre-reaction chamber for determination of cross-reactions of O₃ with interfering species. Sampling of ambient air is conducted via a standard HALO gas inlet using a Teflon line. The precision and accuracy of the measurements depend on the ambient concentrations, typical values are 5% and 7% (NO) and 10% and 15% (NO_y), respectively.

2.10. Trajectories and air mass history analysis

Backtrajectories were calculated for each minute, starting at the location of the HALO aircraft and using the FLEXPART (“FLEXible PARTicle”) Lagrangian Particle Dispersion Model version 9.02 (Stohl et al., 1998; Stohl and Thomson, 1999; Seibert and Frank, 2004; Stohl et al., 2005). Trajectories were driven by six-hourly analyses, interlaced with the three-hour forecasts, from the Global Forecast System (GFS) of the National Centers for Environmental Prediction (NCEP), provided on a 0.5 x 0.5 degree horizontal grid (<http://www.nco.ncep.noaa.gov/pmb/products/gfs/>, last accessed 8 Sep 2016). For each trajectory, 10,000 ‘particles’ (infinitesimally small air parcels) are released and followed back in time for 10 days. Sub-grid-scale processes like convection and turbulence act stochastically on each ‘particle’, resulting in a trajectory location probability distribution at each point in time. For convenience, the location probability distribution is simplified using a clustering algorithm, calculating five cluster centers of most probable trajectory locations (Stohl et al., 2002). Additional trajectory calculations were performed using the HYSPLIT model (Stein et al., 2015) with NCEP GDAS1 data and model vertical velocities. For simplicity, out of the five clusters, we consider only the center cluster given by FLEXPART. Therefore, all trajectories mentioned hereafter refer to the center trajectory.

We examined the history of the sampled airmasses for interactions with deep convection using the FLEXPART trajectories and GOES (Geostationary Operational Environmental Satellite) imagery. Every one-minute flight position was traced back in time in one-hour steps up to

120 hours. Each position was then matched in time to the closest GOES-13 (Geostationary Operational Environmental Satellite) infrared brightness temperature (T_b). As a proxy for deep convection, we searched for cloud top T_b below $-30\text{ }^{\circ}\text{C}$ and looked up the minimum T_b in a $1^{\circ}\times 1^{\circ}$ box around the center of the back-traced parcel. An example of this procedure is available in the Supplement (Figs. S1-S3). From these data, we recorded the time difference between the moment that HALO was sampling the airmass and its encounter with deep convection, possibly including multiple contacts with deep convection. We also noted the “deepest convection” (minimum T_b) encountered by the parcels and their height at the time of the encounter, as well as the number of hours that the parcel was within boxes with deep convection ($T_b < -30\text{ }^{\circ}\text{C}$).

3. Results and Discussion

3.1. The ACRIDICON-CHUVA campaign

The ACRIDICON-CHUVA flights covered most of the Amazon Basin, reaching from the Atlantic coastal waters in the east to near the Colombian border in the west, and from the Guyanas border in the north to the arc of deforestation in the south. The flight tracks of the flights analyzed in this paper are shown in Fig. 1, where the flight segments at altitudes $>8\text{ km}$ are shown as heavier lines. The dates of the flights and other supporting information are given in the overview paper by Wendisch et al. (2016)

3.2. Synoptic situation and chemical context

3.2.1. Meteorological overview

During boreal summer, the Intertropical Convergence Zone (ITCZ) undergoes a seasonal northward shift towards the northernmost part of South America, so that almost all of the Amazon Basin is in the meteorological Southern Hemisphere. Examination of cloud top height and precipitation images showed that the ITCZ was located between about 4 and $12\text{ }^{\circ}\text{N}$ during the campaign (6 Sep to 1 Oct 2014), but was often not very well defined over South America (worldview.earthdata.nasa.gov, last accessed 13 Jan 2017). This seasonal shift establishes the large-scale thermodynamic conditions that define the dry season over the Amazon Basin, characterized by synoptic-scale subsidence, a relatively dry planetary boundary layer (PBL) and mid-troposphere, and warm temperatures at the top of the PBL, resulting in elevated convective inhibition energy (CINE) (Fu et al., 1999; Wang and Fu, 2007; Collow et al., 2016). During the dry

season, there is less shallow convection, cloud cover, and rainfall than in the wet season, but the convection that does occur is more organized with pronounced vertical development because of the simultaneous presence of high convective available potential energy (CAPE) and high CINE (Machado et al., 2004; Collow et al., 2016; Giangrande et al., 2017; Zhuang et al., 2017). The deep convective cloud fraction peaks in the late afternoon and evening (1600LT to 2400LT) with a cloud fraction maximum between 9 and 13 km altitude and a minimum near and above the freezing level between 4 and 7 km (Collow et al., 2016; Zhuang et al., 2017).

During the ACRIDICON-CHUVA campaign, the intense warm sea-surface temperature (SST) anomaly that had earlier prevailed in the southern South Atlantic and a less intense cold SST anomaly in the northern South Atlantic and near the Equator were strongly reduced, and a warm SST anomaly in the equatorial Pacific was building to form the 2015 El Nino (see also Martin et al., 2016). Consequently, the pattern of wind and omega (vertical motion) field anomalies decreased to nearly normal conditions. However, during the campaign there was a clear northeast-southwest contrast with drier conditions in the northeast and wetter ones in the southwest, as seen in the columnar precipitable water anomaly data from the NCEP Climate Forecast System Version 2 Reanalysis (Fig. 2) (Saha et al., accessed 20 March 2017). The majority of HALO flights were over the drier anomaly or the neutral region. As a consequence of this drier anomaly, these regions presented warmer temperatures and lower relative humidity than the normal climatology. The synoptic pattern during the campaign resulted in a spatial rainfall distribution with a meridional pattern, with more intense rainfall in the west, around 300 mm in September, and less than 100 mm in the eastern Amazon (Fig. 3). Nine cold fronts penetrated into Brazil during September, however, only two moved northward and they had little interaction with Amazon convection. Only the cold front on 20 to 23 September was able to organize convection in the south of the Amazon Basin.

Figures 4a and 4b show the low (850 hPa) and high (200 hPa) level wind fields during September 2014. The mean low-level flow at 850 hPa shows the typical easterly winds throughout the Amazon Basin (Fig. 4a), decelerating near the Andes and curving to the subtropics. At high levels (Fig. 4b), there is a weak anticyclonic circulation over the southern basin, featuring the initial increased deep convection in the transition from the dry to the wet season (September) and the development of the Bolivian High during the onset of the wet season (December to March) (Virji, 1981; Zhou and Lau, 1998).

During the research flights, HALO reached maximum altitudes of 12.6 to 14.4 km a.s.l., corresponding to potential temperatures between 352 and 360 K (Fig. 5), i.e., the bottom of the tropical tropopause layer (TTL). The vertical profiles of temperature and potential temperature were remarkably consistent between the flights, showing a fairly stable stratification up to about 8 km and a slightly weaker gradient in potential temperature above this altitude. Relative humidity shows a broad minimum in the region between 6 and 10 km. For comparison, the data from radiosonde soundings at Manacapuru (a site southwest of Manaus) are provided in the supplement (Fig. S4).

Based on the soundings, the mean height of the thermal tropopause during the campaign was 16.9 ± 0.6 km (unless mentioned otherwise, we use the notation “arithmetic average \pm standard deviation” to indicate mean and variance in this paper), corresponding to a potential temperature of about 380 K. During September 2014, the mean CAPE was 1536 J kg^{-1} and the mean CINE value was 37 J kg^{-1} , the precipitable water was 42 mm, the lifting condensation level 919 hPa, and the bulk shear 4.8 m s^{-1} (difference between the mean wind speed in the first 6 km and 500 meters). These values give a clear idea about the typical cloud base expected, the high instability, the need of a forcing due to the CINE, the high shear, and the amount of integrated water vapor.

In this paper, we use the following terminology to describe the different layers of the tropical atmosphere: The region from the surface to the convective cloud base (typically about 1.2 to 1.7 km during mid-day) is the planetary boundary layer (PBL), above which is the convective cloud layer (CCL), which typically reached to altitudes of about 4–5 km during our campaign. The region between the CCL and the TTL is the free troposphere (FT), which we subdivide into the middle troposphere (MT) between about 5 km and 9 km and the upper troposphere (UT) above ca. 9 km.

3.2.2. Airmass origins and history

For an overview of airmass movement in the UT over the central Amazon during the campaign, we obtained trajectory frequency statistics for airmasses arriving at altitudes between 7 and 14 km over the central Amazon Basin. The frequency analysis indicated that airmass movement in the upper troposphere was generally relatively slow and tended to follow anticyclonic patterns (Fig. 6), consistent with the 200 hPa streamlines shown in Fig. 4b. The frequency diagram for the 72-h trajectories initialized at 12 km altitude (Fig. 6a) shows that most airmasses

had remained over the basin for the preceding three days (only about 1% of the endpoints fall outside of the basin), and therefore had a high probability of encountering deep convection outflow. The 10 and 14 km statistics show essentially the same patterns (Supplement Figs. S5–S6), as do the individual trajectories calculated from the aircraft positions along the flight tracks (not shown).

The 120-h trajectory statistics (Fig. 6b) and the examination of the individual trajectories along the flight tracks indicate that the air sampled in the UT had followed a number of different general flow patterns before being sampled by HALO: 1) flow from the Pacific with an anticyclonic loop of variable extent over the basin, ranging from almost zonal west-to-east flow (type A in Table 1) to a huge loop going as far south as Argentina and as far east as the Atlantic, and then returning to the basin (type B, the southernmost trajectories in Fig. 6b), 2) flow from the Atlantic, often almost zonal (type C), 3) internal circulation within the basin, usually along anticyclonic loops, but sometimes erratic (type D), and 4) flow from the Caribbean, often following an anticyclonic pattern (type E, the northernmost trajectories in Fig. 6b). These flow patterns are also evident in the streamlines shown in Fig. 4. Inflow from the Pacific is evident south of 10° S, which can merge with the dominant anticyclone centered at about 8° S, 62° W, whereas inflow from the Atlantic and Caribbean is important mostly north of the Equator. The flow pattern types of the UT airmasses that were enriched in aerosol particles are given in Table 1.

3.2.3. Atmospheric chemical environment

The atmospheric chemical environment over the Amazon Basin shows a pronounced seasonal variation (Talbot et al., 1988; Andreae et al., 1990b; Talbot et al., 1990; Andreae et al., 2002; Artaxo et al., 2002; Martin et al., 2010; Andreae et al., 2012; Artaxo et al., 2013; Andreae et al., 2015). During the rainy season, regional biomass burning is at a minimum and biological sources dominate trace gas and aerosol emissions in the basin, resulting in often near-pristine conditions. The most significant pollution input during this season is long-range transport from North and West Africa, which brings in a mixture of mineral dust and emissions from biomass and fossil fuel burning (Talbot et al., 1990; Wang et al., 2016b). In contrast, ACRIDICON–CHUVA took place during the dry season, when the Amazon Basin is impacted by a mixture of pollution from regional and remote sources (Andreae et al., 1988; Talbot et al., 1988; Artaxo et al., 2013). Deforestation and pasture-maintenance burning occurs throughout the basin, with the

highest intensity along the southern periphery, the so called “arc of deforestation”. This creates a steep gradient of pollutant concentrations from the relatively moist and less densely developed northern and western basin to the drier and highly deforested and developed southern basin (Andreae et al., 2012).

Long-range transport from Africa affects pollution levels over the Amazon, in addition to regional sources. In the northern part of the basin, part of the 10-day backtrajectories arriving at the aircraft positions in the lower troposphere come from West Africa, where biomass burning and fossil-fuel emissions are prevalent, while other trajectories follow the northeastern coast of Brazil, which is densely populated. As one moves south, the influence of long-range transport from Southern Africa becomes more prevalent. This was clearly observed during flight AC19, much of which took place over the Atlantic Ocean east of the Brazilian coast. On this flight, an extended, 300-m thick layer of pollution at 4 km altitude was identified over the Atlantic with elevated rBC concentrations up to $2 \mu\text{g m}^{-3}$ (see section 3.4.4). The backtrajectories from the Amazon south of the Equator very frequently end in the central and eastern tropical Atlantic (see Fig. 3 in Andreae et al., 2015), where high levels of ozone, aerosols, and other pollutants from biomass burning have been documented by in-situ and satellite observations, starting in the 1980s (Watson et al., 1990; Fishman et al., 1991; Andreae et al., 1994; Browell et al., 1996; Fishman et al., 1996).

3.3. Vertical distribution of aerosol particle number concentrations over the Amazon Basin

Figure 7a shows a statistical summary of all CN number concentrations (N_{CN}) observed during the campaign. Data affected by local pollution and cloud artifacts have been removed as discussed in section 2.2. (Additional information about the flight segments on which elevated N_{CN} were encountered is provided in Table 1, and average concentrations for the particle concentrations in the different size classes and altitude regions are given in Table 2.) In the PBL, which typically reached heights of 1.4 to 1.8 km during the afternoon, mean N_{CN} ranged from $\sim 750 \text{ cm}^{-3}$ on the least polluted flights to $\sim 4500 \text{ cm}^{-3}$ in the most polluted regions over the southern part of the basin. Above the PBL, CN concentrations typically remained relatively high within the lower troposphere up to about 3–4 km, and then declined with altitude. N_{CN} reached a minimum of $\sim 700 \text{ cm}^{-3}$ at about 4–5 km altitude everywhere over the basin. This aerosol minimum coincides with the minimum in cloud cover that has been observed at and above the freezing

level, which has been suggested to be associated with rain development by the Wegener-Findeisen-Bergeron process at this level (Collow et al., 2016).

Above this level, we found a general increase in particle concentrations, such that above 8 km, N_{CN} were typically in the range of 2000 to 19,000 cm^{-3} (i.e., the range of quartiles above 8 km in Fig. 7a). On average, N_{CN} in the UT were almost five times as high as in the LT. The 8-km altitude level corresponds approximately to the 340 K potential temperature level, above which elevated CN concentrations had also been found in previous studies (Borrmann et al., 2010; Weigel et al., 2011).

While the statistical plot in Fig. 7a shows a general particle enrichment in the UT, individual vertical profiles show more complex structures (Fig. 7b). The highest N_{CN} , sometimes reaching up to 65,000 cm^{-3} , were encountered in thin layers often only a few hundreds of meters thick. A typical example for such a layer is seen in the descent profile (segment A2) from flight AC09 (Fig. 4b), with peak CN concentrations of ca. 35,000 cm^{-3} . Other profiles, e.g., the descent profile from flight AC07 (segment G), show enhancements over a layer about 3 km thick, with N_{CN} of 10,000 – 20,000 cm^{-3} .

The CN enrichments in the UT consist predominantly of ultrafine particles in the size range below 90 nm. In contrast to N_{CN} , the enhancement of accumulation mode particles (N_{acc} , defined here as the particles in the size range 90 to 600 nm) in the UT is much less pronounced. The concentration of accumulation mode particles in the LT typically ranged from ~500 to ~3000 cm^{-3} , depending on the level of pollution (Fig. 8a). Like the vertical profile of N_{CN} , the profile of N_{acc} also shows a decrease above the LT to a minimum around 4–5 km, followed by an increase towards the upper troposphere. Over the more polluted regions in the southern basin, N_{acc} in the UT was often considerably lower than in the LT. On average, N_{acc} in the UT was only about half the concentration measured in the LT.

Figure 8b illustrates the different behavior of CN and accumulation mode particle number concentrations at the example of a sounding in the central Amazon Basin from flight AC19. In the LT, N_{CN} and N_{acc} have similar values and decline to a minimum at about 4.7 km. Above this altitude, N_{CN} shows several sharp concentration peaks, with one at about 7.4 km reaching concentrations around 65,000 cm^{-3} . These peaks are only weakly, if at all, reflected in N_{acc} , which shows a broad enhancement in the UT to values around 1000 cm^{-3} . Consequently, we find two

types of aerosol enrichments in the UT: at one extreme, thin layers with extremely high N_{CN} values but no significant increase in particles larger than 90 nm, at the other, broad overall particle enrichments with modest values of both N_{CN} and N_{acc} .

3.4. Differences between UT and LT aerosols

The high concentrations of particles in the UT over the Amazon Basin beg the question of their origin. Three different mechanisms can be considered: vertical transport of particles from the PBL by deep convection, horizontal long-range transport from remote source regions, and in-situ new particle formation in the outflow from deep convection. To assess these possibilities, we discuss in the following sections the chemical and physical properties of the UT aerosols and contrast them with the LT aerosol. In section 3.4, we will compare the physical and chemical properties of the aerosols in the LT and UT to examine the role that vertical transport may have played as a source for the UT aerosol enrichments. Long-range transport and new particle formation in the UT will be discussed in section 3.5.

A first argument against vertical transport as the dominant source mechanism for the large particle concentrations in the UT comes simply from the observed CN concentrations. Since we are using concentrations normalized to standard temperature and pressure, N_{CN} should not change with vertical transport alone, and the values measured in the UT should not exceed those measured in the PBL. The fact that CN concentrations in the UT across the entire Amazon Basin are higher than the PBL values we measured anywhere in the basin, often by very large factors, rules out vertical transport of particles from the Amazon PBL as the dominant source of UT particles.

3.4.1. Particle size

The particles in the UT have a very different size distribution from those in the LT, which confirms that they could not have originated from upward transport of PBL aerosols by deep convection. Unfortunately, a detailed analysis of the size distribution of the particles in the UT is hampered by the significant losses of small particles in our inlet system. As discussed in section 2.2, the particle losses increase with altitude such that in the UT most of the particles below ca. 20 nm are lost in the inlet system before reaching the CPC. Because of a longer inlet tubing con-

nection and lower sample flow, the losses were even more significant for the DMPS, and as a result of this and other operational limitations, valid particle size distributions are only available from the LT.

The DMPS measurements in the LT showed that the aerosol size distribution was dominated by an accumulation mode centered at about 190 nm, flanked by an Aitken mode with a maximum at about 80 nm (Fig. 9), in good agreement with the size distributions measured previously at ground level in the Amazon (Zhou et al., 2002; Rissler et al., 2006; Andreae et al., 2015; Pöhlker et al., 2016) and those obtained over the Amazon on the G1 aircraft during the GoAmazon 2014 campaign (Martin et al., 2016; Wang et al., 2016a). For comparison, we show size spectra from GoAmazon 2014 from Wang et al. (2016a), the only published size spectra from the FT over central Amazonia. Unfortunately, these data reach only up to 5.8 km, the ceiling altitude of the G1 aircraft. In the PBL, the spectra were similar to our measurements from the LT. With increasing altitude, total particle concentrations increased and the size spectrum became dominated by an Aitken mode at ca. 50 nm (Wang et al., 2016a). A previous study over the northern Amazon in Suriname had also found a decrease in the modal diameter of the Aitken mode from ~70 nm in the LT to ~30 nm in the UT above 10 km (Krejci et al., 2003). Assuming that similar size distributions prevailed in the UT during ACRIDICON-CHUVA, and given the fact that inlet losses limited our measurements to particle diameters >20–30 nm, it seems justified to conclude that our N_{CN} concentrations in the UT are actually lower limits and that the true concentrations might have been significantly higher.

In the absence of full size spectra, we use the ultrafine fraction [UFF, defined as the fraction of particles with diameters between 90 nm (the lower cutoff of the UHSAS) and ~20 nm (the lower cutoff of the CPC), i.e., $UFF = (N_{CN} - N_{acc})/N_{CN}$] as a metric for the contribution of the Aitken and nucleation modes to the total observed particle concentration. The summary profile plot (Fig. 10a) shows the dramatic difference between the UFF in the LT and UT: In the LT, the mean UFF is about 0.2 ± 0.1 , showing the dominance of the accumulation mode. The share of ultrafine particles increases throughout the middle troposphere, and in the UT they account for the vast majority of particles, with UFF values around 0.7 in regions where both N_{acc} and N_{CN} are moderately enriched, and values approaching 1.0 in the layers with very high N_{CN} . This shows up even more clearly in individual profiles, e.g., the soundings from flight AC18 shown in Fig 10b. The highly enriched layers are represented by UFF peaks in the range of 0.7 to 1.0, whereas

the background UT enrichment exhibits UFF values of 0.5 to 0.8. The highest UFF values were measured in the very young aerosol layer in segment E2 at 13.5 km (Fig. 10b), which had an estimated particle age of about 1–5 hours (more on this layer in section 3.5.2).

3.4.2. Cloud nucleating properties

The cloud nucleating ability of aerosol particles depends both on their size and their chemical composition. Here we focus on CCN concentrations at 0.52% supersaturation ($N_{CCN0.5}$), which are dominated by the particles in the accumulation mode size range, but also include a fraction of the Aitken mode. A full discussion of the CCN measurements during ACRIDICON–CHUVA will be presented elsewhere.

Figure 11a shows the vertical distribution of CCN for the entire campaign, indicating strong variability in the LT, a minimum at ca. 5 km, and elevated concentrations in the UT. The $N_{CCN0.5}$ variability in the LT is related to the variable levels of regional pollution, mostly from biomass burning, which were much higher in the southern part of the basin than in the north. In contrast, there was no systematic difference between the CCN concentrations in the UT above polluted and relatively clean regions. Therefore, depending on the level of pollution in the lower troposphere, the $N_{CCN0.5}$ in the UT during our campaign were higher or lower than those in the LT. This is illustrated at the example of the $N_{CCN0.5}$ profiles from a clean region (AC09) and from one polluted by biomass burning emissions (AC12+13), respectively (Fig. 11b). While there was a large difference in the CCN concentrations in the LT, the values in the UT were very similar between these flights, indicating that the CCN enrichments in the UT are independent of the pollution levels in the LT.

The $N_{CCN0.5}$ in the UT were consistently greater than the corresponding accumulation particle number concentrations, N_{acc} , resulting in a median $N_{CCN0.5}/N_{acc}$ ratio of 1.66 (quartile range 1.32 – 2.32, $N=53,382$) above 8 km. This implies that some of the particles smaller than 90 nm are also able to nucleate cloud drops at $S=0.52\%$. Because size-selective CCN measurements were not performed during ACRIDICON–CHUVA, it was not possible to derive the actual critical diameters and hygroscopicity factors (κ , Petters and Kreidenweis, 2007) for the CCN on this campaign. However, a consistency check can be made using the measured chemical composition. As will be discussed in detail in section 3.4.4, the UT particles consist predominantly of or-

organic material, with minor amounts of nitrate and very small fractions of sulfate. The hygroscopicity of particles consisting completely of organic matter can vary greatly, with κ between near 0 and about 0.3 (Engelhart et al., 2008; Jimenez et al., 2009; Engelhart et al., 2011). Our AMS measurements (see section 3.4.4) showed that the UT secondary organic aerosol (SOA) contains a substantial fraction of organics derived from the oxidation of isoprene (IEPOX-SOA) (Schulz et al., 2017), which has relatively high hygroscopicity ($\kappa \geq 0.12$) (Engelhart et al., 2011; Thalman et al., 2017). Assuming a conservative value of $\kappa_{\text{org}} \cong 0.1$, which had been found previously for the Amazon PBL (Gunthe et al., 2009; Pöhlker et al., 2016), pure SOA particles would have to have diameters of ≥ 80 nm to act as CCN at 0.52% supersaturation, whereas for pure ammonium sulfate particles ($\kappa \cong 0.6$), the critical diameter would be ca. 45 nm (Petters and Kreidenweis, 2007). At a typical organic mass fraction of 0.8 for the UT aerosol (see section 3.4.4), an effective κ of ca. 0.2, corresponding to a critical diameter of ~ 65 nm, is likely. Given the expected steep increase in particle concentration between the N_{acc} cutoff of 90 nm and the estimated critical diameter of 65 nm, a $N_{\text{CCN0.5}}/N_{\text{acc}}$ ratio of the observed magnitude appears thus quite reasonable.

The vertical distribution of the CCN fraction, i.e., the ratio $N_{\text{CCN0.5}}/N_{\text{CN}}$, shows a pronounced decrease with altitude (Fig. 12a), reflecting the smaller particle size in the UT. It also exhibits a strong inverse relation to the total particle concentration, N_{CN} . This is illustrated at the example of flight AC18 (Fig. 12b), where data from the different flight segments are plotted. Segments A and F (yellow and orange) are from soundings in the somewhat more polluted central part of the Amazon Basin, whereas B and C (green) are from the cleaner westernmost part and show the lowest CCN concentrations and the highest CCN fractions. Both soundings have high-CN layers at altitudes between 7 and 13 km, with N_{CN} up to almost $23,000 \text{ cm}^{-3}$, and correspondingly low $N_{\text{CCN0.5}}/N_{\text{CN}}$. Segment E2 (red) is from a layer that was intercepted downwind of a massive convective complex, with a transport time of only 1–5 hours between the anvil and the aircraft (see section 3.5.2). This layer had N_{CN} values up to $45,000 \text{ cm}^{-3}$, CCN fractions down to 0.01, and $\text{UFF} \cong 0.98$, suggesting that these recently formed particles were too small to act as CCN. This layer was embedded in a region of moderately elevated CN (segment E1 at 13–14 km; lilac), which had much higher $N_{\text{CCN0.5}}/N_{\text{CN}}$ (0.2–0.5) and lower UFF (0.6–0.8), indicating larger particle sizes and likely a more aged aerosol. Segment D (blue), at 11–12 km altitude, had

similar properties to E1. These observations confirm the presence of the two distinct types of elevated aerosol populations in the UT, introduced in section 3.3. At one extreme, there are aerosols with very high N_{CN} and ultrafine fractions and low CCN fractions (e.g., E2), presumably representing newly formed particles with sizes too small to act as CCN. At the other extreme, there are populations with modest N_{CN} , but low UFF and high CCN fractions, indicating a more aged aerosol with larger particles (e.g., E1 and D).

The existence of these two populations is confirmed in plots of $N_{CCN0.5}$ and $N_{CCN0.5}/N_{CN}$ against supersaturation. Examples are shown in Figs. 13a and 13b, with AC18-DD representing a segment dominated by larger and aged particles, AC07-F a region with high concentrations of small and younger particles, and AC09-AA a mixed case with short periods of very high N_{CN} over a background of moderately elevated particle concentrations. Even though the mean CN concentration exceeds 8900 cm^{-3} in AC07-F, the mean $N_{CCN0.5}$ in the same region is only 13 cm^{-3} and therefore the $N_{CCN0.5}/N_{CN}$ vs. S plot falls essentially on the baseline. In contrast, AC18-DD presents a fairly “classical” supersaturation spectrum, and AC09-AA is a mixed case with the measurements made during the N_{CN} peaks showing very low $N_{CCN0.5}/N_{CN}$.

In Figs. 13c and 13d, we compare the mean supersaturation spectra from the lower, middle, and upper troposphere obtained on flights AC12 and AC13, which were taken on successive days over the same region and where the LT was influenced by biomass burning pollution. In the LT, the CCN fraction is in the range observed at ground level at the Amazon Tall Tower Observatory (ATTO) site (Pöhlker et al., 2016) and in close agreement with measurements in the southern Amazon during the biomass burning season (Vestin et al., 2007). In the UT, we observed low CCN fractions representing the regions with high N_{CN} and UFF, mostly at altitudes of 10–11 km, and higher CCN fractions at 12 km and above corresponding to a region with somewhat elevated CCN ($1000\text{--}1500\text{ cm}^{-3}$; cf. Fig. 11b, which shows the CCN concentrations from these flights). In the middle troposphere (5–8 km) we found intermediate CCN fractions, consistent with a mixture of LT and UT aerosols.

3.4.3. Volatility

On several flights (AC16, 18, 19, and 20), a second CPC was operated behind a thermomoder at a temperature of $250\text{ }^{\circ}\text{C}$, in parallel to the regular CPC, providing the concentration of non-volatile particles, N_{nonvol} . The results of these measurements are shown in Fig. 14a in

the form of the volatile fraction ($VF=[N_{CN} - N_{nonvol}]/N_{CN}$) plotted against altitude. In the LT, most particles are nonvolatile and the VF is typically between 10 and 20%. This is consistent with the behavior described by Clarke and Kapustin (2010) and Thornberry et al. (2010), who found that aged combustion aerosols (from biomass or fossil-fuel burning) are non-volatile and mostly in the accumulation mode size fraction. With increasing altitude, the VF increases, closely resembling the profile of the UFF. In the UT, the mean VF reaches about 80%, and approaches 100% in the most highly enriched layers (e.g., segment E2). In previous campaigns, high volatile fractions had also been observed in the tropical UT and TTL, with the highest VF in the region between 340 and 360 K potential temperature, corresponding to about 9–15 km (Borrmann et al., 2010; Weigel et al., 2011).

More detail can be seen when looking at data from an individual flight. In Fig. 14b we show the profiles from AC18, which we had already discussed in the context of CCN concentrations in the previous section. The profiles (segments A, B, C, and F) show the overall increase in VF with height, with peak values at embedded high-CN layers. The freshest layer (E2), which had the highest UFF, also has the highest VF. In contrast, segments D and E1, representing larger UT regions with moderate CN enrichments, larger particles, and higher CCN fraction also have lower VFs, between 0.4 and 0.7. A contribution from aged combustion aerosols can be ruled out as source for the non-volatile particles in these layers, because the rBC concentrations are close to zero (see below). As we will show in the next section, it appears that these low-volatility particles represent a more aged organic aerosol.

3.4.4. Chemical composition

As discussed above, the LT aerosol over the Amazon during the dry season is dominated by the products of biomass burning, with increasing concentrations from north to south. This is clearly reflected in its chemical composition, which is dominated by carbonaceous matter (organic and elemental carbon) and only contains minor fractions of inorganic species, such as potassium, sulfate, and nitrate. Elemental or black carbon is a unique tracer of combustion emissions and was measured on HALO in the form of refractory black carbon (rBC).

The vertical profile of rBC shows a sharp separation between LT and FT (Fig. 15). The average rBC concentration in the region below 5 km was $0.25 \pm 0.21 \mu\text{g m}^{-3}$, whereas in the FT above 6 km it was $0.002 \pm 0.006 \mu\text{g m}^{-3}$ in terms of mass concentrations, and $99 \pm 92 \text{ cm}^{-3}$ vs.

1.5±2.5 cm⁻³ in number concentrations of rBC particles. Interestingly, these concentrations over the Amazon Basin are only slightly higher than the values measured over the tropical Western Atlantic during the Saharan Aerosol Long-range Transport and Aerosol-Cloud-Interaction Experiment (SALTRACE; Weinzierl et al., 2017), June–July 2013: ca. 0.2 µg m⁻³ in the LT and ca. 0.001 µg m⁻³ in the FT (Schwarz et al., 2017), which suggests that a significant fraction of the rBC is entering the basin by long-range transport from Africa. Transport of biomass smoke containing BC and other constituents from Africa to South America has been documented previously, e.g., from Northern Africa during the wet season (Talbot et al., 1990; Wang et al., 2016b) and from Southern Africa during the dry season (Andreae et al., 1994). A detailed study on the transport of Southern African aerosols to the Amazon during ACRIDICON-CHUVA is in preparation and will be published elsewhere.

In 14 instances, elevated rBC concentrations were seen for short durations (usually less than 30 sec) in the UT. Most of the time, they occurred during cloud penetrations in the course of vertical cloud microphysics profiling. In the case of the flights over the northern half of the Amazon Basin, they could likely be attributed to sampling of HALO’s own exhaust, based on the flight track and the presence of associated NO enhancements in the absence of strong enhancements of CO and other aerosol species (CCN, N_{acc}, N_{CN}). On flights over the southern Amazon (AC07, AC12, AC13, and AC20), where the PBL was more polluted and active fires were present, there were a few instances when elevated rBC coincided with peaks in CO and accumulation mode particles, which suggests upward transport of biomass smoke aerosols. In view of the scarcity of such events during our campaign and their modest rBC concentrations, it is clear that they do not represent a major source of combustion aerosol for the UT during our campaign. No elevated rBC concentrations were observed during the extensive outflow sampling legs on any of the flights. A detailed discussion of the rBC measurements during the campaign will be presented in a companion paper (Holanda et al., 2017).

The drop in rBC concentration by two orders of magnitude between LT and FT implies that rBC, and by extension other aerosols (which are likely even more prone to being removed by nucleation scavenging), are efficiently removed during deep convection and consequently that there is little transport of LT aerosols into the FT. This provides further evidence that enrichments in N_{CN} and N_{acc} in the FT cannot be explained by vertical transport of particles from the FT.

The AMS measurements also show pronounced differences in the composition of the LT and UT aerosols (Fig. 16). In Table 2 we present a detailed analysis of the results from three flights, AC07 from a polluted region in the southern Amazon, and AC09 and AC18 from relatively clean regions in the northern and northwestern parts of the Basin, respectively. Organic aerosol (OA) is the dominant aerosol species in all three regions at all altitudes, as expected in an area where biomass burning and secondary organic aerosol (SOA) production are the dominant sources.

In the LT, (ammonium) sulfates (SO₄) are together with rBC the next most important species. Here, we see a clear difference between the BB-dominated region in the south (with high OA, ammonium [NH₄], and rBC, and relatively low SO₄) versus the northern basin, where SO₄, likely from long-range transport, plays a more important role. The ratio OA/rBC in the LT is in the range 3–11, consistent with values from BB aerosols. The biomass burning marker, f_{60} (Schneider et al., 2006; Alfarra et al., 2007), is present in all the measurements from the LT, but always mixed with oxidized secondary organics. It should also be noted that the f_{60} marker is not an inert tracer but decays with time, and a typical observed background level of the f_{60} tracer is 0.3% of OA (Cubison et al., 2011).

In the UT, SO₄ shows lower concentrations than in the LT, with the most pronounced difference on flights AC07 and AC18. The latter flights also show a large difference in the OA/SO₄ ratio, which is around 10 in the UT and around 2 in the LT. Because of the high BB component in flight AC07, this ratio is also relatively high in the LT on this flight. The most pronounced differences between UT and LT are seen in the nitrogen species. Ammonium is usually present in the BL, sometimes at considerable levels (e.g., on AC07), but always below the detection limit in the UT. In contrast, nitrate (NO₃) is a minor species in the LT, whereas in the UT it is comparable or greater than SO₄, so that the ratio NO₃/SO₄ is about an order of magnitude higher in the UT than in the LT. High concentrations of organics, especially oxidized organics, and nitrate had been seen previously in the UT by Froyd et al. (2009).

The nature of the nitrate signal in the UT cannot be definitely identified from our data. The absence of NH₄ and the ratio of the peaks associated with ammonium nitrate make it unlikely that the NO₃ signal represents ammonium nitrate (Fry et al., 2009; Bruns et al., 2010). It may be, at least to a large part, indicative of organonitrates, which have been shown to account

for 15–40% of SOA mass in laboratory experiments (Berkemeier et al., 2016) and whose formation is enhanced at low temperatures (Lee et al., 2014).

A closer look at the aerosol-enriched layers in the UT from these flights reinforces these conclusions (Table 2). In these layers, the ratios OA/SO₄ and NO₃/SO₄ can reach very high values, especially in the SO₄-poor UT of flight AC07. On flights AC09 and AC18, we encountered extended periods when N_{acc} and $N_{CCN0.5}$ were elevated, while N_{CN} did not show extremely high values (AC09-AA, AC18-AA, and AC18-DD). The AMS data from these segments were generally similar to the UT averages, suggesting that they are representative of the ambient UT aerosols. The layers with very high N_{CN} on these flights (AC09-BB, AC09-EE, AC09-A1+A2, and AC18-A1, AC18-A2, AC18-E2, AC18-F) also did not show significant differences from the UT means on these flights, likely because the numerous, but very small CN in these layers did not contain enough mass to influence the AMS measurements in a detectable way.

We attempted to examine this hypothesis further by investigating the size dependence of the AMS signals, but because of the small aerosol mass concentrations in the UT, size information from the AMS data required extended integration periods, which precluded obtaining size data from the relatively short segments with very high N_{CN} . The most robust size data were from the segments where relative high N_{acc} concentrations prevailed over extended periods of time, e.g., segment DD (Table 2) on flight AC18. Here, the organic aerosol (OA) showed a broad mode between 80 and 250 nm, with a modal diameter at 150 nm. This confirms that the AMS compositional data are dominated by the accumulation mode, while the particles that make up most of the UF fraction in the UT do not have enough mass to provide a clear AMS signal. An exception may be some segments on AC09 (BB and EE), where OA and NO₃ data suggest a mass mode between 60 and 120 nm. Here, the UFF is quite high (0.85 and 0.92, compared to segment DD on flight AC18, where it was 0.61) suggesting a smaller and therefore younger aerosol population.

More detailed information on the origin of the organics in the UT aerosol can be obtained from specific markers. In the UT, the BB marker f_{60} is typically not detectable, which in combination with the fact that the ratio OA/rBC is of the order of 1000, precludes a significant contribution of aerosols from biomass burning or other primary combustion aerosols to the OA in the UT. In contrast, the marker f_{82} , which is indicative of IEPOX-SOA formed by the photooxidation

of isoprene (Robinson et al., 2011; Hu et al., 2015), is found in the aerosol-enriched layers in the UT, suggesting oxidation of isoprene and other biogenic volatile organic compounds (BVOC) as source of the OA. The f_{82} marker is not correlated with sulfate, which suggests that sulfate may not have been participating in the formation of the IEPOX-SOA. Furthermore, in all cases with high f_{82} , the aerosol is not neutralized by NH_4^+ . These issues will be discussed in detail in a forthcoming paper by Schulz et al. (2017)

The plot f_{43} vs. f_{44} is frequently used to represent the aging of organic aerosols (Ng et al., 2011). In Fig. 17, we show the median locations of the LT and UT aerosol in this plot, which indicates that both are fairly well aged and oxidized, with the UT data plotting slightly towards less oxidized and younger values. This may reflect an overall younger aerosol, or the admixture of recent material either by condensation on the accumulation mode particles or in the form of an external mixture of larger aged particles with small younger ones. The individual segments from flight AC18, which had the lowest OA/SO₄ and NO₃/SO₄ ratios, also plot in this region, showing that they are dominated by a relatively well-aged aerosol. In contrast, segments AC09-AA, and AC07-AA1, AC07-AA2, and AC07-GG, which have the highest OA/SO₄ and NO₃/SO₄ ratios and much higher N_{CN} , plot much further to the lower right indicating a less oxidized, fresher aerosol. On this flight, the concentrations of accumulation mode aerosols in the UT were relatively low, so that freshly formed aerosol could be more evident because of a lower background of aged aerosol.

In summary, the chemical composition data show that, while both LT and UT aerosols are dominated by aged organics, their sources must be different because the UT aerosol is essentially devoid of the combustion tracers, rBC and f_{60} , whereas the OA/rBC ratios in the LT are consistent with combustion aerosols. Nitrate is strongly elevated in the UT, and may consist to a large extent of organonitrates. NH_4 is a significant component in the LT, whereas it is below the detection limit in the UT. Size-selective chemical analysis is difficult because of the low aerosol mass concentrations, but the available data suggest that the AMS measurements are dominated by the accumulation mode, and the strong N_{CN} enhancements are not distinctly seen in the AMS data. Chemical marker analysis shows the general absence of BB tracers in the UT, while the marker f_{82} indicates production of IEPOX-SOA from isoprene. Most of the UT organics are aged

and oxidized, but in some of the CN-enriched layers, younger and less oxidized OA was evidenced by much lower f_{44}/f_{43} ratios. A detailed discussion of the AMS measurements during ACRIDICON-CHUVA will be presented in Schulz et al. (2017).

3.5. The roles of long-range transport and deep convection

In the preceding sections, we have documented the differences between the aerosols in the LT and the UT, which rule out the possibility that convective transport of PBL aerosols can be an important source for the UT aerosols. This opens the question about the other potential sources of these particles: are they the result of long-range transport from remote sources or do they originate over the Amazon Basin? In the latter case, are they directly released in the outflow from the convective clouds or are they produced by subsequent nucleation and growth in the UT?

For the larger particles in the accumulation mode, represented by elevated N_{acc} and $N_{CCN0.5}$ in the UT, long-range transport cannot be excluded, because such particles can have long lifetimes in the upper troposphere (Williams et al., 2002). While the absence of detectable rBC still rules out an origin from pollution aerosols lofted from the LT, they may have formed days or weeks ago by gas-to-particle formation mechanisms anywhere in the free troposphere. In contrast, the high concentrations of small UF particles that we observed with high frequency in the UT cannot come from distant sources, as they persist only for hours to a few days before growing to larger sizes and decreasing in concentration due to coagulation and dilution processes (Williams et al., 2002; Krejci et al., 2003; Ekman et al., 2006).

3.5.1. Aerosols in cloud tops, anvils and outflows

First, we consider the possibility of these particles having been produced already inside the clouds and released by outflow into the UT. In earlier studies, NPF had been shown to occur in ice clouds in the tropical/subtropical UT, especially in conditions where the available surface area of ice particles was relatively low (e.g., Lee et al., 2004; Frey et al., 2011). To look for this phenomenon, we examined the particle concentrations during passages through the upper levels of deep convective clouds and in the anvils directly attached to active cumulonimbus clouds (Cb). Our measurements during these passages consistently show lower CN and CCN concentra-

tions than in the surrounding UT air, as exemplified in Fig. 18a by data from flight AC18. During this flight segment, we performed multiple penetrations of the tops of growing Cb at altitudes between 10.7 and 12.0 km and temperatures in the range of 225 to 236 K. During each cloud passage (indicated in Fig. 18a by the ice particle concentrations) the aerosol concentrations decreased sharply, to values of N_{CN} around 800 cm^{-3} and $N_{CCN0.5}$ around 250 cm^{-3} during the longer cloud passages. (Here, we use $N_{CCN0.5}$ as proxy for the accumulation mode particles, since the N_{acc} measurements in clouds were perturbed by shattering at the probe tip, whereas the N_{CN} and $N_{CCN0.5}$ measurements showed no artifacts in ice clouds.) In the case of N_{CN} , the values in the cloud tops are about the same as the PBL concentrations measured in the same region, while for $N_{CCN0.5}$ they are significantly lower than the PBL values of around 400 cm^{-3} .

The same behavior was found for all cloud penetrations in the UT during the campaign. In particular, extensive cloud top and outflow sampling on AC09, AC15, and AC16 showed $N_{CCN0.5}$ values down to $160\text{--}250 \text{ cm}^{-3}$ and N_{CN} values down to $600\text{--}1000 \text{ cm}^{-3}$. The lowest particle concentrations were seen in a large outflow sampled on AC13 (20:08–20:30 UTC), when both N_{CN} and $N_{CCN0.5}$ reached values below 50 cm^{-3} (Fig. 18b). In this airmass, NO and NO_y were strongly elevated indicating recent NO production by lightning in the large Cb from which this outflow originated.

Given that the air sampled during the cloud passages had already mixed in by lateral entrainment some of the surrounding air with much higher particle concentrations (Bertram et al., 2007; Yang et al., 2015), these low particle concentrations in the cloud tops and outflows are clear evidence that in-cloud processes were a sink and not a source of particles in the size class measureable with our instrumentation. A rough estimate of the scavenging efficiency of the convective process can be gained by using CO as a conservative tracer. For example, on flight AC18 the PBL concentrations of CO and N_{CN} averaged $\sim 120 \text{ ppb}$ and 780 cm^{-3} , and the UT during the cloud penetrations around 1900 UTC had CO $\sim 95 \text{ ppb}$ and $N_{CN} \sim 1500 \text{ cm}^{-3}$. In the cloud, CO rose to 108 ppb and N_{CN} dropped to 750 cm^{-3} . Following the approach of Bertram et al. (2007), we can estimate that the fraction of PBL air in the center of the cloud was ca. 0.52, and that without scavenging, $N_{CCN0.5}$ would be ca. 1130 cm^{-3} . From these values, a scavenging loss of 90% or more of CCN can be estimated, in good agreement with previous studies (e.g., Andreae et al., 2001; Yang et al., 2015), and consistent with the absence of detectable rBC.

Flight AC20 was the only exception to this behavior. Here, CN were strongly enhanced during cloud passages and even CCN were slightly elevated in some passages. The cloud that was sampled on this flight appears to have been a pyrocumulus that had been ingesting fresh biomass smoke, as suggested by the strongly elevated CO during the cloud passages. This flight will be discussed as a separate case study below (section 3.6.).

While these results show that the high particle concentrations we observed in the UT were not directly released from the cloud tops, they do not rule out the possibility that new particle formation had already started in the clouds or anvils. This is because the newly formed particles observed in the earlier studies were almost exclusively in the size range below 20 nm (Lee et al., 2004; Frey et al., 2011). Since our measurements are limited to particle sizes >20 nm, we would not have been able to detect such freshly nucleated particles, and therefore the earliest phases of particle nucleation and NPF over Amazonia will have to be addressed in future studies. Our data do show, however, that release of particles by hydrometeor evaporation following deep convection is not a net source of particles to the UT over Amazonia, in contrast to what was observed over the Indian Ocean region by Engström et al. (2008). Because the N_{CN} and $N_{CCN0.5}$ concentrations in the ambient air in the UT are actually higher than in the air detrained by the Cb clouds, the detrainment leads at least initially to a reduction in UT particle concentrations in the size class >20 nm. Only through subsequent NPF can this be reversed and deep convection then become a net source of UT aerosols.

3.5.2. Relationship between aerosol enhancements and airmass history

Connections between the presence of aerosol enhancements and the outflow from convective systems had been observed in some previous studies (de Reus et al., 2001; Twohy et al., 2002; Benson et al., 2008; Weigelt et al., 2009). We examined the connection between deep convection (DC) and the presence of high CN concentrations by a combination of backtrajectory calculations and the analysis of cloud-top temperatures from GOES-13 weather satellite images, similar to the approach used in some previous studies (de Reus et al., 2001; Froyd et al., 2009; Weigelt et al., 2009). We analyzed backtrajectories initialized at the aircraft locations where we had observed elevated aerosol concentrations, as listed in Table 1. Then we checked for each hour along the backtrajectories whether the airmass had crossed a region with DC (cloud top

temperatures below -30°C). The results show that in all cases, the aerosol enriched airmasses had encountered deep convection within the last 120 hours.

In Fig. 19 we present the results from two flights (AC09 and AC18) as examples. We find that for all flight segments that showed high aerosol concentrations in the UT (dark shading), the airmasses had made contact with DC with cloud tops typically reaching about -80°C . Of course, given the abundance of convection over Amazonia, it is to be expected that most airmasses would have interacted with convection within 120 hours (such as the example shown in the Supplement Fig. S2). For comparison, over the northeastern United States during summertime, Bertram et al. (2007) had found that more than 50% of UT air had encountered DC within the previous 2 days.

The cumulative plot of the time since the most recent DC contact (Fig. 20a) shows that on all flights (except AC19, the flight over the Atlantic) almost all aerosol-enhanced air masses had seen DC within the last 30–40 hours. The cloud tops during these encounters typically reached -70 to -80°C (Fig. 20b). In many cases, the air mass history analysis shows multiple contacts with deep convection within the preceding 72 hours. It must be noted, however, that the physical interaction between an UT air mass and a specific deep convective event is not represented in the trajectory model. Because the model does not “see” the individual convective event that brings up an outflow, it cannot trace a parcel back into this outflow and back down to the boundary layer. On the other hand, an air parcel trajectory that passed through the vicinity of the outflow, but is not part of the actual outflow, will keep moving backward along the mean flow in the UT and may then encounter another outflow. Obviously, however, the uncertainty in the trajectory position increases with time going backwards, and is probably enhanced by passage near a region of active convection.

In some cases, the airmasses could be tracked back to regions where the cold cloud encountered by the tracked air mass looked more like cirrus than identifiable deep convective outflow. The same favorable conditions for nucleation (low temperature, low pre-existing aerosol surface) as in the outflow regions prevail also in native cirrus, and Lee et al. (2004) had reported NPF in cirrus without immediate connection to DC. This might also have occurred in our campaign, but it is usually difficult to distinguish cirrus and very aged outflow.

To test whether there was a difference in the airmass histories between segments with high and low N_{CN} , we searched our data for suitable segments with low N_{CN} . However, because of the high variability of the CN concentrations in the UT, the times when N_{CN} was below 3000 cm^{-3} were in almost all cases very short, and would not lend themselves to a meaningful analysis of airmass history. To illustrate this, we show a full time series plot of the measurements from Flight AC09 in the supplement (Fig. S7).

We were only able to find a total of six segments, where N_{CN} was consistently below 3000 cm^{-3} , and which were not identifiably part of an outflow. These are listed in Table S1 in the supplement. The segments from flights AC16 and AC18 were well away from clouds, whereas those from AC19 and 20 were in the vicinity of Cbs, but not clearly in an outflow. The segment L from AC19 is low in CN, but actually has a relatively high $N_{CCN0.5}$, and may not really be significantly different from the aged enriched segment E2, which was sampled immediately after it. Consequently, we don't have a data set that would allow a representative analysis of the history of airmasses with low particle concentrations. Notably, however, the airmass trajectory types in these segments do not contain type D, i.e., recirculation within the Amazon basin. The air in the segments from AC20, which had the lowest particle concentrations, had come in straight from the Pacific within the last 48 hours, but may also contain some outflow air.

Information about the time required for particle production and the evolution of the aerosol populations in the UT can be derived from a close examination of the trajectories for individual flight segments. Flight AC18 provides some illustrative examples. The trajectories of the first particle plumes encountered (A1 and A2, Table 1) had passed close to areas of intense deep convection (-30 to -60 °C) about 17–21 hours before sampling. Because it is likely that the aerosol precursor substances are formed by photochemical reactions, we also looked at the amount of time that the airmass was exposed to sunlight (Lee et al., 2003). Since the convective encounters occurred between 16LT and 00LT and the measurements were taken at about 11LT, the airmass had only about 5–7 h of sun exposure. Assuming that the formation of the particles required photochemical processes, this implies that about 5–7 h were sufficient to produce particle concentrations above 20,000 cm^{-3} with sizes >20 nm. The enrichment in this case occurred only in the particles size range <90 nm, with a UFF of about 0.98, while N_{acc} remained at the same levels as in the surrounding background FT. Segment F, near the end of the flight, was sampling a similar region as A1, with a similar airmass trajectory. Since this segment was taken near the end of the

day, the airmass had experienced about 11 hours of sunlight. There is somewhat of a shift towards larger particles, but this might also be coincidental.

The air in segments B and C had traveled along similar trajectories as A1 and A2, but unfortunately there are no GOES images available for the time when they crossed the convective region encountered by A1 and A2, and so no conclusions can be drawn for these segments. Segments D and E1 represent airmasses that had made multiple and extended convection encounters over the central and western Amazon during the past three days. Here, we find only weak enhancements in N_{CN} , but significantly elevated $N_{CCN0.5}$ and N_{acc} , with a UFF of 0.73 and 0.82, respectively, suggesting that coagulation and growth had taken place over this time period.

Some of the highest N_{CN} (up to ca. $45,000 \text{ cm}^{-3}$) and UFF (0.98) were found in Segment AC18-E2, which was sampling the air just a few hours downwind of a massive convective system that reached well above our flight altitude of almost 14 km. The air sampled here had traveled for about one hour after leaving the convective complex before being encountered by HALO and had been interacting with this complex for up to 5 h, all of them in daylight. As in A1, A2, and F, there was no detectable enhancement in aerosol mass, as represented by N_{acc} and $N_{CCN0.5}$. In contrast to this very fresh aerosol with high number concentrations, the strongest enhancement in aerosol mass was seen in the early part of segment E1, which didn't show a strong increase in number concentration. The air during this segment had made its last contact with a convective system about 65–72 hours before sampling.

Another illustrative case is flight AC09 over a clean region in the northern Amazon. Segments A1-A3 sampled clear air that had DC contact about 16 and 60 hours ago and the UFF around 0.94 indicated a moderately aged aerosol. Segments B1 and B2 were taken in air immediately surrounding a Cb anvil, with previous DC contacts at about 14, 80, and 120 hours before. Here, the relatively low UFF of ~ 0.92 signaled no influence from the freshly outflowing air. Segments C, D, and E were in air close to a Cb, within its anvil, and in a large anvil/outflow, respectively. Otherwise, they had a DC contact history similar to B. Here also, the UFF remains fairly low, and there is no evidence of particle production directly in the anvil/outflow.

To summarize, our observations indicate that, while there is no evidence of immediate production of detectable particles (i.e., $>20 \text{ nm}$) in the actual anvil or outflow, a small number of daylight hours are sufficient to produce very large concentrations of particles with sizes larger

than about 20 nm in the FT. This is consistent with the observations made in the outflow of a convective complex off Darwin, Australia, where maximum Aitken concentrations were reported after ca. 3 hours since the outflow (Waddicor et al., 2012). During NPF events in the FT on the Jungfrauoch, high concentrations of particles >20 nm were observed about 4–6 hours after sunrise (Bianchi et al., 2016). In the FT over other regions, growth may be considerably slower; for example the measurements over oceanic regions by Weigelt et al. (2009) showed that it took about 12 hours for particles >12 nm to reach their maximum concentrations.

Considerably longer times (a few days) are required, however, before increases are detectable in the size class >90 nm. The development of significant amounts of particles in the accumulation mode appears to take two days or more, in agreement with the observations of Froyd et al. (2009), who had found enhanced aerosol organic mass concentrations over the Caribbean in UT air originating from Amazonia after 2–4 days in the atmosphere. Since many, if not most of our trajectories remain over Amazonia for this amount of time, there is enough time available in the UT over the Amazon Basin to produce CCN-sized aerosols within the region, which can subsequently be transported downward or be exported to other regions.

3.5.3. Aerosol enhancements and chemical tracers

The relationship between new particle production and the input of boundary layer air is also reflected in a correlation between N_{CN} and CO. When taking all data above 8 km, this correlation is highly significant given the large number of data points ($N=68,360$) but not very close ($r^2=0.52$) because of the large variability of CO concentrations in the PBL and UT background between flights (Fig. 21). Closer relationships are obtained when looking at individual flights and especially at individual profiles within flights.

Weigel et al. (2011) had seen a strong correlation between CO and nucleation mode particles over West Africa and interpreted it as indication of anthropogenic inputs. In contrast, over Amazonia we have not seen any evidence that UT aerosol production shows any relationship to boundary layer pollution, and we interpret the correlation between N_{CN} and CO simply as reflecting the input of air from the PBL, which generally has higher CO concentrations than the UT, by the cloud outflow.

An opposite relationship is generally seen between N_{CN} and O_3 , which tends to be lower in the particle-enriched layer. We also see this as an indication of injection of air from the PBL,

which generally has lower O_3 concentrations than the UT. Because of the great variability in the O_3 concentrations in the UT, there is no general correlation between N_{CN} and O_3 for the entire mission ($r^2=0.02$). For individual flights, modest, but statistically significant, negative correlations can be found, e.g., an r^2 value of 0.13 ($N=8509$) in the UT on flight AC09. The scatter plot in Fig. S08 shows that high O_3 concentrations were always associated with low N_{CN} , but that there were low- O_3 regions in the UT both with and without enhanced particle concentrations.

To look for a possible relationship between water vapor concentration and NPF, we examined several flights (AC07, AC09, AC13, and AC18) for relationships between RH and N_{CN} . We found a tendency for the layers with high N_{CN} to be associated with moister layers ($RH>50\%$), but also many exceptions. This relationship may simply have to do with the fact that moisture was brought up with the convective clouds, or there may be a relationship with the actual particle formation process, but at this point we do not have the data needed to answer these questions.

The nitrogen oxides show a complex relationship with the particle enhancements in the UT, as illustrated at the example of a flight segment from AC07 (Fig. 22). The highest NO concentrations are found in the Cb anvils or freshest outflows, as identified by significant concentrations of ice particles (e.g., at 2056, 2119, and 2154 UTC). In these regions, we typically observed particle minima, as discussed above. In these airmasses, NO has been formed very recently by lightning, and the NO to NO_y ratios are usually still very high. Here, the particles are still depleted by convection scavenging and there has not been enough time for new particles to form, at least not in the size range detectable by our instrumentation. On the other hand, there is a strong positive relationship between NO_y and N_{CN} , as seen in Fig. 22 during the entire period from 2051 to 2210 UTC. Regions with high concentrations of new particles generally show elevated NO_y , typically in the range of 1 to 3 ppb, indicating that photochemical reactions had taken place that both produced new particles and converted NO to NO_y .

3.6. Flight AC20: A special case with NPF from biomass smoke

On flight AC20, HALO performed detailed sampling of the anvil and outflow of a large Cb over northern Rondonia, a state with a high incidence of deforestation burning. Numerous outflow penetrations around this Cb were made, and the ice particles sampled here could be clearly identified as freshly produced in the Cb top. The CN concentrations in the UT away from

the outflow were unimpressive, typically in the range 2000 to 10,000 cm^{-3} . However, in sharp contrast to the other flights, where the air in the outflow always had been depleted in aerosol particles, on this flight the outflow often showed much higher CN concentrations, between 10,000 and 20,000 cm^{-3} (Fig. 23a). The concentrations of CCN and nonvolatile CN in the outflow were either the same as in the surrounding air or slightly higher, also contrasting with the observations on the other flights, where they had been depleted. Since the N_{CN} in the outflow were also much higher than in the PBL ($\sim 2000 \text{ cm}^{-3}$), entrainment of PBL air cannot explain the CN enrichment.

The mixing ratios of CO, NO, and NO_y were also elevated in the outflow (Fig. 23b), which in the case of CO and NO_y might be explained by inputs from the PBL, where CO and NO_y levels were around 120–200 ppb and 2–3 ppb, respectively. The NO values in the PBL, on the other hand, were only about 0.13 ppb, similar to the UT values, requiring an additional NO source for the outflow.

The explanation for this unusual behavior may be found in the layer between 11.5 and 12.5 km that was penetrated during both ascent and descent (Fig. 23c). In this layer, N_{CN} reached 30,000 cm^{-3} , CO was elevated to ~ 140 ppb, N_{acc} to 850 cm^{-3} , and NO_y to ~ 1.6 ppb. The data also suggest a slight enrichment in rBC, but this is close to the limit of detection. These values suggest that this is a detrainment layer polluted with biomass smoke, as we have often seen on previous campaigns over the burning regions in southern Amazonia (Andreae et al., 2004). An urban origin of this pollution is unlikely, since the only town in the region, Porto Velho, lies about 50–100 km downwind of the sampling area.

For a comparison with biomass smoke, we computed the enhancement ratios, $\Delta N_{\text{acc}}/\Delta \text{CO}$ and $\Delta \text{CCN}_{0.5}/\Delta \text{CO}$, as the slopes of the bivariate regression between these variables for the time period between 16:53 and 16:58 UTC. The enhancement ratios in this layer differ clearly from fresh biomass smoke. The ratio $\Delta N_{\text{acc}}/\Delta \text{CO}$ is $\sim 6\text{--}12 \text{ cm}^{-3} \text{ ppb}^{-1}$ and the ratio $\Delta \text{CCN}/\Delta \text{CO}$ about $2.5 \text{ cm}^{-3} \text{ ppb}^{-1}$, much lower than the typical ratios in fresh smoke, which are about $20\text{--}40 \text{ cm}^{-3} \text{ ppb}^{-1}$ (Janhäll et al., 2010), indicating removal of CCN-sized particles during the upward transport. In contrast, the ratio $\Delta \text{CN}/\Delta \text{CO}$ was about $350 \text{ cm}^{-3} \text{ ppb}^{-1}$, almost an order of magnitude above the values typical of fresh smoke. These results suggest that biomass smoke was brought to the UT either from the strongly smoke-polluted PBL in this region or actually by a pyro-Cb over an active fire, and that the concentration of the larger primary smoke particles was

strongly reduced by scavenging, which allowed new particle formation in this smoke layer. The enrichments seen in the outflow penetrations at altitudes above the 12-km layer may be the result of entrainment of air from this layer or of rapid particle formation in situ. Further evidence for the upward transport of pyrogenic emissions was found in measurements on a horizontal leg at 11 km, which had only modest CN concentrations (around 1700 cm^{-3}), but elevated CCN, NO_y , CO, and aerosol nitrate and organics, with similar values to the biomass-burning polluted boundary layer below. While we have this kind of observations from only one flight, which took place over the most polluted region sampled during this campaign, they are suggestive of the potential of rapid particle formation and growth in smoke detrainment layers, an issue that merits further study in future campaigns.

3.7. Conceptual model and role in aerosol life cycle

The discussion in the preceding sections can be summarized in a conceptual model of the aerosol life cycle over the Amazon Basin (Fig. 24). Cloud updrafts in deep convection bring air from the PBL into the middle and upper troposphere, where it is released in the convective outflow (Krejci et al., 2003). During this process, most pre-existing aerosols are removed by precipitation scavenging, especially the larger particles that account for most of the condensation sink (Ekman et al., 2006). Most likely, organic compounds with low and very low volatilities are also removed by deposition on hydrometeors, which provide a considerable amount of surface area inside the clouds (Murphy et al., 2015).

On the other hand, the rapid transport of PBL air to the UT inside deep convective clouds facilitates lofting of the more volatile reactive BVOCs from the Amazon boundary layer (Colomb et al., 2006; Apel et al., 2012). Here, the initially O_3 - and NO_x -poor boundary layer air is supplied with O_3 by mixing with UT air and addition of NO from lightning, creating a highly reactive chemical environment. This mixture is exposed to an extremely high actinic flux due to the high altitude and multiple scattering by ice particles. Because of the low air mass at UT altitudes, the actinic flux is already very high shortly after sunrise. In this environment, rapid photooxidation of BVOCs and formation of ELVOCs/HOMs is to be expected. In laboratory studies, ELVOCs/HOMs have been shown to be rapidly produced at fairly high yields both by ozonolysis of terpenes and by reactions with OH radicals (Ehn et al., 2014; Jokinen et al., 2015; Berndt et al., 2016; Dunne et al., 2016).

The outflow regions in the UT present an ideal environment for particle nucleation, as had already been suggested in some earlier studies (Twohy et al., 2002; Lee et al., 2004; Kulmala et al., 2006; Weigelt et al., 2009). The temperatures are some 60–80 K lower than in the PBL, which decreases the equilibrium vapor pressure of gaseous species (Murphy et al., 2015) and increases the nucleation rate. Based on classical nucleation theory and molecular dynamics calculations, Yu et al. (2017) have estimated an increase in nucleation rate by one order of magnitude per 10 K. Nucleation rate measurements in the CERN CLOUD chamber indicate a similar temperature dependence (Dunne et al., 2016). Note, however, that these temperature dependencies are based on measurements for inorganic NPF, and that while the trends for organics are expected to be similar, the magnitude of the increase in nucleation rates for organics may be quite different. Because the preexisting aerosol has been depleted during the passage through convective clouds before being released into the UT from the cloud outflow, the low particle surface area in the UT presents only a small condensation sink and thus very little competition to nucleation (Twohy et al., 2002; Lee et al., 2003; Lee et al., 2004; Young et al., 2007; Benson et al., 2008).

In the absence of measurements of the relevant gaseous sulfur species and the composition of the nucleating clusters, we cannot make firm conclusions about the actual nucleation mechanism. Over marine regions and polluted continental regions, the particles observed in outflows and in the UT were mostly identified as sulfates (Clarke et al., 1999; Twohy et al., 2002; Kojima et al., 2004; Waddicor et al., 2012), and consequently H_2SO_4 has been proposed as the nucleating species. However, since in some cases this identification was based only on the volatility of the particles, they could have also consisted of organics or mixtures of organics and H_2SO_4 . Over the Amazon, nucleation by H_2SO_4 cannot be excluded based on our observations, especially if there was already some SO_2 or H_2SO_4 present in the UT before the injection of the organic-rich PBL air. However, since the Amazonian BL contains very little SO_2 , the sulfur species would have had to come from outside the region and thus they would have had the opportunity to be oxidized to H_2SO_4 and nucleate into particles during its travel in the UT well before entering Amazonia. It is therefore likely that the particles in the Amazon UT formed by homogeneous nucleation of organics, as has been suggested by several authors (Kulmala et al., 2006; Ekman et al., 2008; Murphy et al., 2015). Nucleation by formation of clusters containing both H_2SO_4 and oxidized organic molecules is of course also a possibility that we cannot exclude

(Metzger et al., 2010; Riccobono et al., 2014). However, recent studies have shown that HOM compounds can nucleate to form particles even in the absence of H_2SO_4 , especially in the UT (Bianchi et al., 2016; Kirkby et al., 2016), and nucleation of HOMs without involvement of H_2SO_4 has been suggested to be the dominant mode of new particle formation in large parts of the pre-industrial atmosphere by the modeling study of Gordon et al. (2016). The importance of ions produced from cosmic radiation in this nucleation process is still controversial (Lee et al., 2003; Yu et al., 2008; Bianchi et al., 2016; Kirkby et al., 2016).

Regardless of the actual nucleating species, H_2SO_4 or HOMs/ELVOCs, the growth of the particles observed in our campaign must have been dominated by organics, as shown by the composition of the aerosol measured by the AMS. The dominance of organics in the growth of aerosols in pristine environments has also been suggested on the basis of measurements and modeling studies, both for the lower troposphere (Laaksonen et al., 2008; Riipinen et al., 2011; Riipinen et al., 2012; Öström et al., 2017) and the UT (Ekman et al., 2008; Murphy et al., 2015). In particular, isoprene-derived SOA has been suggested to be important in the growth of sub-CCN-size particles to CCN (Ekman et al., 2008; Jokinen et al., 2015), which would be consistent with the prevalence of isoprene in the Amazonian PBL and our observations of IEPOX-SOA in the UT aerosol. As the particles grow, the decrease of the Kelvin (curvature) effect with increasing size of the growing particles implies that subsequently relatively more volatile organics can condense (Tröstl et al., 2016), in agreement with the observed high volatile fraction we observed in the upper tropospheric CN.

While in general the volatile fraction of the particles in the UT was very high, there were also regions with a significant fraction of particles that did not evaporate at 250 °C (see section 3.4.3). These were dominated by relatively aged organics, which, based on the absence on detectable rBC, must also be of secondary origin. Such thermally refractory organics may explain the presence of non-volatile particles in the tropical UTLS, which had been observed in previous campaigns especially in the region above 360 K (Borrmann et al., 2010).

Once particles have nucleated in the UT and grown into the Aitken mode and in some cases even into the accumulation mode size ranges, they can be transported downward towards the lower troposphere both by general subsidence under the prevailing high pressure system over Amazonia and by downdrafts associated with deep convective activity. Large-scale entrainment

of UT and MT air into the boundary layer has been suggested as the major source of new particles in marine regions (Raes, 1995; Katoshevski et al., 1999; Clarke et al., 2013). Over Amazonia with its high degree of convective activity, downdrafts are likely to play a more important role. Downward transport of UT air by downdrafts associated with deep convective activity has been shown to inject air with lower moisture content, lower equivalent potential temperature, and elevated O₃ into the PBL (Zipser, 1977; Betts et al., 2002; Sahu and Lal, 2006; Grant et al., 2008; Hu et al., 2010; Gerken et al., 2016). It would follow that the same mechanism also brings down aerosol-rich air from the UT into the PBL. Indeed, in a recent aircraft study over the central Amazon, this mechanism was shown to be an important source of atmospheric aerosols, predominantly in the Aitken mode, to the Amazonian PBL (Wang et al., 2016a). Here, they can continue to grow by condensation of BVOC-derived organics into the accumulation mode and become available as CCN, closing the aerosol cycle over Amazonia.

This mechanism provides an explanation for the origin of secondary aerosol particles in the clean Amazon PBL, where the occurrence of “classical” nucleation events, characterized by the rapid appearance of large numbers of particles <10 nm and subsequent growth into an Aitken mode (e.g., Kulmala and Kerminen, 2008), has never been reported, in spite of several years of observations by several teams (Martin et al., 2010; Rizzo et al., 2013; Andreae et al., 2015). This has been attributed to the low emissions of gaseous sulfur species in the basin (Andreae and Andreae, 1988; Andreae et al., 1990a), which result in H₂SO₄ vapor concentrations that are too low to induce nucleation (Martin et al., 2010). Nucleation of particles from organic vapors alone is not favored in the Amazonian PBL because of high temperatures and humidity as well as the competition by the condensation sink on pre-existing particles, which results in organic coatings on almost all primary and secondary particles in the Amazonian PBL (Pöschl et al., 2010; Pöhlker et al., 2012).

4. Summary and Conclusions

As part of the ACRIDICON-CHUVA 2014 aircraft campaign, we investigated the characteristics and sources of aerosols in the upper troposphere over the Amazon Basin. We observed regions with high number concentrations of aerosol particles (tens of thousands per cm³ STP) in the UT on all flights that reached above 8 km. The aerosol enhancements were commonly in the

form of distinct layers with thicknesses of a few hundreds to a few thousands of meters. Such layer structures are a common feature of the free troposphere and have been related to detrainment from deep convection and large-scale subsidence (Newell et al., 1999).

In other regions, upward transport of aerosols from the PBL had been suggested to be an important source of UT aerosols, based on the abundance of low-volatility particles (Clarke and Kapustin, 2010), TEM analysis of individual particles (Kojima et al., 2004), or modeling of cloud processes (Yin et al., 2005). Over Amazonia, however, our study showed that the UT aerosol was fundamentally different from the aerosol in the LT, indicating that upward transport of PBL aerosols, especially combustion aerosols from BB, is not an important source of aerosols to the Amazonian UT.

The number concentrations of particles in the UT were often several orders of magnitude higher than in the LT, and their size distribution was dominated by the Aitken rather than the accumulation mode. In contrast to the LT, the particles in the UT were predominantly volatile at 250 °C and had much higher organics and nitrate contents. The extremely low concentrations of rBC in the MT and UT show that the aerosols above the LT are not combustion-derived and indicate that the low-volatility fraction must be representing secondary organics of extremely low volatility (ELVOCs/HOMs). Regarding the size class large enough to act as CCN (i.e., larger than 60–80 nm), we can conclude based on the absence of rBC and the lack of BB indicators in the AMS measurements that the enhanced CCN in the UT are not related to upward transport of combustion products, in contrast to most previous studies (e.g., Krejci et al., 2003; Engström et al., 2008; Clarke et al., 2013).

By analyzing the history of the particle-enriched airmasses and comparing the transport paths to GOES infrared imagery, we could show in all cases that these airmasses had been in contact with deep convective outflow. Measurements inside the cloud tops and the outflow anvils close to the clouds showed that the pre-existing aerosols in the ascending air had been almost completely scavenged by in-cloud processes, making the clouds initially a net aerosol sink. The near-complete scavenging is consistent with the hypothesized large water vapor supersaturation in pristine tropical deep convective clouds, which can nucleate particles that are much smaller than the commonly defined CCN (Khain et al., 2012).

Based on our measurements, we propose that BVOCs in the cloud outflow are rapidly oxidized to HOMs/ELVOCs, which because of the low temperatures and low condensation sink can form new particles, possibly together with H₂SO₄, and grow to sizes ≥ 20 nm within a few hours, making deep convective clouds an indirect aerosol source. This had also been concluded based on a large statistical sampling of UT air in the Northern Hemisphere by the CARIBIC aircraft measurement program (Weigelt et al., 2009). The importance of NPF in the UT for the budget of CN and CCN had been proposed previously on the basis of modeling studies (Yu et al., 2008; Merikanto et al., 2009; Carslaw et al., 2017), and is evident in the global enhancement of CN in the UT, especially in tropical regions, seen in compilations of data from numerous aircraft campaigns (Yu et al., 2008; Reddington et al., 2016). In this way, aerosol production by BVOC oxidation in the UT can provide the “missing source” of FT organic aerosol, which had been deduced from a mismatch between models and observations (Heald et al., 2005).

The high aerosol concentrations in the UT provide a reservoir of particles that are available for downward transport into the PBL both by large-scale downward motion and by convective downdrafts. In a recent study, we have shown that transport of aerosols by downdrafts from the free troposphere is an important, if not the dominant, source of particles to the lower troposphere (LT) over the Amazon (Wang et al., 2016a). The particles that are produced by this mechanism in the UT over the Amazon (and probably other tropical continents as well) can be transported globally due to their long lifetime in the UT (Williams et al., 2002; Clarke et al., 2013) and affect the microstructure of low-level clouds after they eventually descend into the PBL, possibly at very large distances from the source areas of their precursors.

Our study and the results of some previous studies (Lee et al., 2003; Froyd et al., 2009) suggest that UT aerosol production is especially important in the tropics because of the high rate of BVOC production and the abundance of deep convection, but its relevance may also extend to temperate and boreal regions. Our measurements both in the Amazon and at a remote site in central Siberia, distant from SO₂ emission sources and thus experiencing very low H₂SO₄ concentrations, show that “classical” nucleation events are very rare to absent at such sites and may not provide a strong source of new particles (Heintzenberg et al., 2011; Andreae et al., 2015; Wiedensohler et al., 2017). Consequently, the UT may be an important, possibly even the dominant source of tropospheric aerosol particles in regions that are not strongly affected by anthropogenic or natural primary aerosols. This would assign clouds a central role in the aerosol life

cycle, controlling both source and sink of aerosol particles, at least in regions of low anthropogenic pollution. Furthermore, the relevance of UT aerosol production may not be limited to the troposphere, because the UT and the TTL are also important reservoirs for the transport of particles into the lower stratosphere (Fueglistaler et al., 2009; Borrmann et al., 2010; Randel and Jensen, 2013). Organic aerosols in the lower stratosphere have been shown to have significant radiative effects (Yu et al., 2016).

The conceptual model proposed here implies a profound difference between the present-day polluted atmosphere and the pristine pre-industrial situation, especially over the continents. In the pristine atmosphere, the gradient of particle number concentrations may have been from high values in the UT to low values in the PBL, as we have found in Amazonia. In polluted continental regions, on the other hand, nucleation and NPF occur predominantly in the lower troposphere, where they add to primary emitted particles (Spracklen et al., 2006), and which thus has become the dominant source region of atmospheric aerosols in today's atmosphere over much of the world. Average N_{CN} measured at ground level at polluted continental sites worldwide range between 3400 and 19,000 cm^{-3} in the compilation by Andreae (2009). In the UT, on the other hand, the median particle concentrations ($> 12 \text{ nm}$) measured in the CARIBIC program over polluted continents are $\sim 3500 \text{ cm}^{-3}$ over North America, $\sim 2500 \text{ cm}^{-3}$ over Europe, and $\sim 3000 \text{ cm}^{-3}$ over India (Ekman et al., 2012). Of course, there are elevated values in the UT at particular places and times over polluted continents, such as those reported by Twohy et al. (2002), but they appear to be more the exception than the rule. This vertical structure is quite close to being the exact opposite of the distribution measured over Amazonia during ACRIDICON-CHUVA, where the averages ($\pm \text{std.dev.}$) were $7700 \pm 7970 \text{ cm}^{-3}$ in the UT and $1650 \pm 980 \text{ cm}^{-3}$ in the LT. Consequently, in the anthropocene the aerosol concentration profile has been turned upside down, at least in many polluted regions, since now the highest concentrations are found in the PBL.

This has important consequences for the Earth's climate system. The aerosol concentrations in the PBL influence cloud microphysical properties and radiative energy fluxes, which affect the characteristics of convection and thereby influence cloud radiative forcing, atmospheric stability, precipitation, and atmospheric dynamics at all scales (Jiang et al., 2008; Koren et al., 2008; Rosenfeld et al., 2008; Koren et al., 2010; Fan et al., 2012; Rosenfeld et al., 2014;

Gonçalves et al., 2015; Stolz et al., 2015; Dagan et al., 2016; Braga et al., 2017). By their radiative and microphysical effects on convection dynamics, aerosols are also able to increase upper tropospheric humidity, which plays an important role in the Earth’s radiation budget (Sherwood, 2002; Kottayil and Satheesan, 2015; Riuttanen et al., 2016) and may also affect the potential for aerosol nucleation in the UT, thus providing an additional feedback.

5. Acknowledgments

We thank the entire ACRIDICON–CHUVA team for the great cooperation that made this study possible. Our thanks go especially to the HALO pilots, Steffen Gamsa, Michael Grossrubatscher, and Stefan Grillenbeck, who always worked hard to put the aircraft at the right place for our measurements, even under sometimes difficult conditions. We appreciate the support of the colleagues from enviscope GmbH for their valuable help in certifying and installing the numerous instruments for HALO and thank the HALO team of the DLR for their cooperation. We acknowledge the generous support of the ACRIDICON–CHUVA campaign by the Max Planck Society, the German Aerospace Center (DLR), FAPESP (São Paulo Research Foundation), and the German Science Foundation (Deutsche Forschungsgemeinschaft, DFG) within the DFG Priority Program (SPP 1294) “Atmospheric and Earth System Research with the Research Aircraft HALO (High Altitude and Long Range Research Aircraft)” by contract no VO1504/4-1, SCHN1138/1-2, MI 583/4-1 and JU 3059/1-1, WE 1900/22-1, WE 1900/24-1, WE 1900/36-1. This study was also supported by EU Project HAIC under FP7-AAT-2012-3.5.1-1 and by the German Federal Ministry of Education and Research (BMBF, grant No. 01LG1205E). C. Voigt acknowledges financing by the Helmholtz Association under contract no. W2/W3-60. M. A. Cecchini was funded by FAPESP grants number 2014/08615-7 and 2014/21189-7. The participation of D. Rosenfeld was supported by project BACCHUS, European Commission FP7-603445. B. Weinzierl, M. Dollner, D. Sauer, and A. Walser received funding from the Helmholtz Association under Grant VH-NG-606 (Helmholtz-Hochschul-Nachwuchsforschergruppe AerCARE) and from the European Research Council under the European Community’s Horizon 2020 research and innovation framework program/ERC Grant Agreement 640458 (A-LIFE). A. Spanu was funded through the Marie Curie Initial Training Network VERTIGO (grant agreement number 607905).

6. Figure Captions

- Figure 1: Tracks of the flights on which measurements at high altitude were made during ACRIDICON-CHUVA. The flight segments at altitudes >8 km are shown as heavier lines.
- Figure 2: Columnar precipitable water anomaly for September 2014 (based on the 1981-2010 average NCEP/NCAR Reanalysis).
- Figure 3: Total rainfall (mm per month, 1° resolution) for September 2014. Data from the Global Precipitation Climatology Centre (GPCC).
- Figure 4: Mean wind speeds during September 2014 at a) 850 hPa and b) 200 hPa (Data from NCEP/NCAR).
- Figure 5: Vertical profiles of potential temperature, static air temperature, and relative humidity measured on HALO during the ACRIDICON-CHUVA flights over the Amazon Basin.
- Figure 6: Trajectory statistics based on (a) 72-hour and (b) 120-hour backtrajectory calculations for September 2014, initialized at Manaus at an elevation of 12 km.
- Figure 7: Vertical profiles of CN concentrations, N_{CN} ; a) overall statistics from all flights, b) examples from individual profiles on flight AC07 (segment G) and AC09 (segments A1 and A2).
- Figure 8: Vertical profiles of accumulation mode particle concentrations, N_{acc} ; a) 1-min averaged data from all flights, b) N_{acc} profile from flight AC19 together with the profile of N_{CN} from the same flight (1-sec data).
- Figure 9: Size spectra: The black line shows the mean boundary layer DMPS size spectrum from a segment in the PBL on flight AC13 (16:55 to 17:18 UTC). The square black symbols represent the mean, the grey shaded area the standard deviation of the measurements. The line is a logarithmic fit with modal diameters of 74 and 175 nm. The colored lines represent size distributions from 0.65 to 5.8 km from a G1 flight during GoAmazon (Wang et al., 2016a).
- Figure 10: Vertical profiles of the ultrafine fraction (UFF); a) overall statistics from all flights, b) examples from individual profiles on flight AC18.
- Figure 11: Vertical profiles of CCN concentrations at 0.52% supersaturation; a) overall statistics from all flights (1-min averages), b) examples from individual profiles on flights AC09 (green)

1413 and AC12+13 (red). Flights AC12 and AC13 were conducted over the same region on successive
 1414 days.

1415 Figure 12: a) CCN fraction ($N_{CCN0.5}/N_{CN}$) vs altitude, all data. The peak at 11 km is caused by the
 1416 inclusion of a large number of measurements from flight AC20 on a horizontal leg at 11 km,
 1417 which was influenced by biomass burning (see section 3.6). b) CCN fraction vs. CN concentra-
 1418 tion for specific segments from flight AC18 (see text for discussion).

1419 Figure 13: a) CCN fractions ($N_{CCN0.5}/N_{CN}$) and b) CCN concentrations ($N_{CCN0.5}$) vs. supersatura-
 1420 tion from selected legs from flights AC07, AC09, and AC18; c,d) data from flights AC12 and
 1421 AC13 for the LT, MT, and UT.

1422 Figure 14: Volatile fraction. a) statistics from all flights; b) individual segments from flight
 1423 AC18 (see text for discussion).

1424 Figure 15: Refractory black carbon vs altitude, all flights, 30-second averages.

1425 Figure 16: Aerosol chemical composition as determined by AMS and SP2 measurements in the
 1426 lower, middle, and upper troposphere.

1427 Figure 17: Plot of the AMS factors f_{44} vs. f_{43} , indicating the median values for the LT and UT
 1428 and values for some UT flight segments with elevated aerosol concentrations. With increasing
 1429 degree of oxidation, the measurements move to the upper left of the triangle

1430 Figure 18: Measurements during passages through cumulonimbus cloud tops and outflow anvils:
 1431 a) Several cloud top penetrations at 10.7 to 12 km altitude on flight AC18 showing reduced N_{CN}
 1432 and $N_{CCN0.5}$ inside the cloud top; b) Outflow from a large active cumulonimbus, showing strong
 1433 aerosol depletion and NO production by lightning.

1434 Fig. 19: Airmass contacts with deep convection. The colors indicate the cloud top temperature of
 1435 the convective system with which the trajectory had the most recent contact. The aircraft altitude
 1436 at which the airmass was sampled is indicated by the red line. The colored dots are plotted at the
 1437 altitude at which the airmass crossed the grid cell with the convective system. The dots are only
 1438 plotted if this altitude is greater than 6 km and if it encountered a DC region (i.e., $T_b < -30$ °C).
 1439 The shaded areas correspond to the flight segments with elevated CN concentrations. a) flight
 1440 AC09, b) flight AC18.

1441 Figure 20: a) Number of hours since last contact with deep convection for flight segments with
 1442 elevated aerosol concentrations (cumulative frequency, all flights); b) frequency distribution of
 1443 minimum GOES brightness temperature (T_b) for selected flights legs (within 5-day backward tra-
 1444 jectories).
 1445 Figure 21: CN vs CO concentrations in the upper troposphere above 8 km (15-second averages).
 1446 Figure 22: CN, NO, and NO_y concentrations in a flight segment in the upper troposphere on
 1447 flight AC07.
 1448 Figure 23: a) Measurements of $N_{\text{CCN}0.5}$, N_{CN} , N_{nonvol} , and ice particles during cloud top penetra-
 1449 tions on flight AC20 at altitudes between 12.3 and 13.5 km. b) Concentrations of CO, NO, and
 1450 NO_y on the same flight segments. c) Measurements of N_{acc} , N_{CN} , rBC, CO, and O_3 during the
 1451 climb from 11.0 to 13.5 km.
 1452 Figure 24: Conceptual model of the aerosol life cycle over the Amazon Basin.

7. References

- Abdelmonem, A., Järvinen, E., Duft, D., Hirst, E., Vogt, S., Leisner, T., and Schnaiter, M., PHIPS–HALO: the airborne Particle Habit Imaging and Polar Scattering probe – Part 1: Design and operation: *Atmos. Meas. Tech.*, 9, 3131-3144, doi:10.5194/amt-9-3131-2016, 2016.
- Alfarra, M. R., Prevot, A. S. H., Szidat, S., Sandradewi, J., Weimer, S., Lanz, V. A., Schreiber, D., Mohr, M., and Baltensperger, U., Identification of the mass spectral signature of organic aerosols from wood burning emissions: *Environ. Sci. Technol.*, 41, 5770-5777, doi:10.1021/es062289b, 2007.
- Andreae, M. O., and Andreae, T. W., The cycle of biogenic sulfur compounds over the Amazon Basin. I. Dry season: *J. Geophys. Res.*, 93, 1487-1497, 1988.
- Andreae, M. O., Browell, E. V., Garstang, M., Gregory, G. L., Harriss, R. C., Hill, G. F., Jacob, D. J., Pereira, M. C., Sachse, G. W., Setzer, A. W., Dias, P. L. S., Talbot, R. W., Torres, A. L., and Wofsy, S. C., Biomass-burning emissions and associated haze layers over Amazonia: *J. Geophys. Res.*, 93, 1509-1527, 1988.
- Andreae, M. O., Berresheim, H., Bingemer, H., Jacob, D. J., Lewis, B. L., Li, S.-M., and Talbot, R. W., The atmospheric sulfur cycle over the Amazon Basin, 2. Wet Season: *J. Geophys. Res.*, 95, 16,813-16,824, 1990a.
- Andreae, M. O., Talbot, R. W., Berresheim, H., and Beecher, K. M., Precipitation chemistry in central Amazonia: *J. Geophys. Res.*, 95, 16,987-16,999, 1990b.
- Andreae, M. O., Anderson, B. E., Blake, D. R., Bradshaw, J. D., Collins, J. E., Gregory, G. L., Sachse, G. W., and Shipham, M. C., Influence of plumes from biomass burning on atmospheric chemistry over the equatorial Atlantic during CITE-3: *J. Geophys. Res.*, 99, 12,793-12,808, 1994.
- Andreae, M. O., Artaxo, P., Fischer, H., Freitas, S. R., Gregoire, J. M., Hansel, A., Hoor, P., Kormann, R., Krejci, R., Lange, L., Lelieveld, J., Lindinger, W., Longo, K., Peters, W., Reus, M. d., Scheeren, B., Silva Dias, M. A. F., Ström, J., van Velthoven, P. F. J., and Williams, J., Transport of biomass burning smoke to the upper troposphere by deep convection in the equatorial region: *Geophys. Res. Lett.*, 28, 951-954, 2001.
- Andreae, M. O., Artaxo, P., Brandão, C., Carswell, F. E., Ciccioli, P., da Costa, A. L., Culf, A. D., Esteves, J. L., Gash, J. H. C., Grace, J., Kabat, P., Lelieveld, J., Malhi, Y., Manzi, A. O., Meixner, F. X., Nobre, A. D., Nobre, C., Ruivo, M. d. L. P., Silva-Dias, M. A., Stefani, P., Valentini, R., von Jouanne, J., and Waterloo, M. J., Biogeochemical cycling of carbon, water, energy, trace gases and aerosols in Amazonia: The LBA-EUSTACH experiments: *J. Geophys. Res.*, 107, 8066, doi:10.1029/2001JD000524, 2002.
- Andreae, M. O., Rosenfeld, D., Artaxo, P., Costa, A. A., Frank, G. P., Longo, K. M., and Silva-Dias, M. A. F., Smoking rain clouds over the Amazon: *Science*, 303, 1337-1342, 2004.
- Andreae, M. O., Correlation between cloud condensation nuclei concentration and aerosol optical thickness in remote and polluted regions: *Atmos. Chem. Phys.*, 9, 543–556, 2009.

1493 Andreae, M. O., Artaxo, P., Beck, V., M. Bela, Gerbig, C., Longo, K., Munger, J. W.,
 1494 Wiedemann, K. T., and Wofsy, S. C., Carbon monoxide and related trace gases and
 1495 aerosols over the Amazon Basin during the wet and dry seasons: *Atmos. Chem. Phys.*,
 1496 12, 6041–6065, 2012.

1497 Andreae, M. O., Acevedo, O. C., Araùjo, A., Artaxo, P., Barbosa, C. G. G., Barbosa, H. M. J.,
 1498 Brito, J., Carbone, S., Chi, X., Cintra, B. B. L., da Silva, N. F., Dias, N. L., Dias-Júnior,
 1499 C. Q., Ditas, F., Ditz, R., Godoi, A. F. L., Godoi, R. H. M., Heimann, M., Hoffmann, T.,
 1500 Kesselmeier, J., Könemann, T., Krüger, M. L., Lavric, J. V., Manzi, A. O., Lopes, A. P.,
 1501 Martins, D. L., Mikhailov, E. F., Moran-Zuloaga, D., Nelson, B. W., Nölscher, A. C.,
 1502 Santos Nogueira, D., Piedade, M. T. F., Pöhlker, C., Pöschl, U., Quesada, C. A., Rizzo,
 1503 L. V., Ro, C. U., Ruckteschler, N., Sá, L. D. A., de Oliveira Sá, M., Sales, C. B., dos
 1504 Santos, R. M. N., Saturno, J., Schöngart, J., Sörgel, M., de Souza, C. M., de Souza, R. A.
 1505 F., Su, H., Targhetta, N., Tóta, J., Trebs, I., Trumbore, S., van Eijck, A., Walter, D.,
 1506 Wang, Z., Weber, B., Williams, J., Winderlich, J., Wittmann, F., Wolff, S., and Yáñez-
 1507 Serrano, A. M., The Amazon Tall Tower Observatory (ATTO): overview of pilot
 1508 measurements on ecosystem ecology, meteorology, trace gases, and aerosols: *Atmos.*
 1509 *Chem. Phys.*, 15, 10,723-10,776, doi:10.5194/acp-15-10723-2015, 2015.

1510 Apel, E. C., Olson, J. R., Crawford, J. H., Hornbrook, R. S., Hills, A. J., Cantrell, C. A.,
 1511 Emmons, L. K., Knapp, D. J., Hall, S., Mauldin, R. L., Weinheimer, A. J., Fried, A.,
 1512 Blake, D. R., Crounse, J. D., St Clair, J. M., Wennberg, P. O., Diskin, G. S., Fuelberg, H.
 1513 E., Wisthaler, A., Mikoviny, T., Brune, W., and Riemer, D. D., Impact of the deep
 1514 convection of isoprene and other reactive trace species on radicals and ozone in the upper
 1515 troposphere: *Atmos. Chem. Phys.*, 12, 1135-1150, doi:10.5194/acp-12-1135-2012, 2012.

1516 Artaxo, P., Martins, J. V., Yamasoe, M. A., Procópio, A. S., Pauliquevis, T. M., Andreae, M. O.,
 1517 Guyon, P., Gatti, L. V., and Leal, A. M. C., Physical and chemical properties of aerosols
 1518 in the wet and dry season in Rondonia, Amazonia: *J. Geophys. Res.*, 107, 8081,
 1519 doi:10.1029/2001JD000666, 2002.

1520 Artaxo, P., Rizzo, L. V., Brito, J. F., Barbosa, H. M. J., Arana, A., Sena, E. T., Cirino, G. G.,
 1521 Bastos, W., Martin, S. T., and Andreae, M. O., Atmospheric aerosols in Amazonia and
 1522 land use change: from natural biogenic to biomass burning conditions: *Faraday*
 1523 *Discussions*, 165, 203-235, doi:10.1039/C3FD00052D, 2013.

1524 Benson, D. R., Young, L. H., Lee, S. H., Campos, T. L., Rogers, D. C., and Jensen, J., The
 1525 effects of air mass history on new particle formation in the free troposphere: case studies:
 1526 *Atmos. Chem. Phys.*, 8, 3015-3024, 2008.

1527 Berkemeier, T., Ammann, M., Mentel, T. F., Pöschl, U., and Shiraiwa, M., Organic nitrate
 1528 contribution to new particle formation and growth in secondary organic aerosols from
 1529 alpha-pinene ozonolysis: *Environ. Sci. Technol.*, 50, 6334-6342,
 1530 doi:10.1021/acs.est.6b00961, 2016.

1531 Berndt, T., Richters, S., Jokinen, T., Hyttinen, N., Kurten, T., Otkjaer, R. V., Kjaergaard, H. G.,
 1532 Stratmann, F., Herrmann, H., Sipila, M., Kulmala, M., and Ehn, M., Hydroxyl radical-
 1533 induced formation of highly oxidized organic compounds: *Nature Communications*, 7,
 1534 13677, doi:10.1038/ncomms13677, 2016.

1535 Bertram, T. H., Perring, A. E., Wooldridge, P. J., Crounse, J. D., Kwan, A. J., Wennberg, P. O.,
1536 Scheuer, E., Dibb, J., Avery, M., Sachse, G., Vay, S. A., Crawford, J. H., McNaughton,
1537 C. S., Clarke, A., Pickering, K. E., Fuelberg, H., Huey, G., Blake, D. R., Singh, H. B.,
1538 Hall, S. R., Shetter, R. E., Fried, A., Heikes, B. G., and Cohen, R. C., Direct
1539 measurements of the convective recycling of the upper troposphere: *Science* 315, 816-
1540 820, 2007.

1541 Betts, A. K., Gatti, L. V., Cordova, A. M., Dias, M. A. F. S., and Fuentes, J. D., Transport of
1542 ozone to the surface by convective downdrafts at night: *J. Geophys. Res.*, 107, 8046,
1543 doi:10.1029/2000JD000158, 2002.

1544 Bianchi, F., Tröstl, J., Junninen, H., Frege, C., Henne, S., Hoyle, C. R., Molteni, U., Herrmann,
1545 E., Adamov, A., Bukowiecki, N., Chen, X., Duplissy, J., Gysel, M., Hutterli, M.,
1546 Kangasluoma, J., Kontkanen, J., Kürten, A., Manninen, H. E., Münch, S., Peräkylä, O.,
1547 Petäjä, T., Rondo, L., Williamson, C., Weingartner, E., Curtius, J., Worsnop, D. R.,
1548 Kulmala, M., Dommen, J., and Baltensperger, U., New particle formation in the free
1549 troposphere: A question of chemistry and timing: *Science*, 352, 1109-1112,
1550 doi:10.1126/science.aad5456, 2016.

1551 Borrmann, S., Kunkel, D., Weigel, R., Minikin, A., Deshler, T., Wilson, J. C., Curtius, J., Volk,
1552 C. M., Homan, C. D., Ulanovsky, A., Ravegnani, F., Viciani, S., Shur, G. N., Belyaev, G.
1553 V., Law, K. S., and Cairo, F., Aerosols in the tropical and subtropical UT/LS: in-situ
1554 measurements of submicron particle abundance and volatility: *Atmos. Chem. Phys.*, 10,
1555 5573-5592, doi:10.5194/acp-10-5573-2010, 2010.

1556 Braga, R. C., Rosenfeld, D., Weigel, R., Jurkat, T., Andreae, M. O., Wendisch, M., Pöschl, U.,
1557 Voigt, C., Mahnke, C., Borrmann, S., Albrecht, R. I., Molleker, S., Vila, D. A., Machado,
1558 L. A. T., and Grulich, L., Aerosol concentrations determine the height of warm rain and
1559 ice initiation in convective clouds over the Amazon basin: *Atmos. Chem. Phys. Discuss.*,
1560 2017, 1-44, doi:10.5194/acp-2016-1155, 2017.

1561 Brock, C. A., Hamill, P., Wilson, J. C., Jonsson, H. H., and Chan, K. R., Particle formation in the
1562 upper tropical troposphere - a source of nuclei for the stratospheric aerosol: *Science*, 270,
1563 1650-1653, doi:10.1126/science.270.5242.1650, 1995.

1564 Brock, C. A., Cozic, J., Bahreini, R., Froyd, K. D., Middlebrook, A. M., McComiskey, A.,
1565 Brioude, J., Cooper, O. R., Stohl, A., Aikin, K. C., de Gouw, J. A., Fahey, D. W., Ferrare,
1566 R. A., Gao, R. S., Gore, W., Holloway, J. S., Hubler, G., Jefferson, A., Lack, D. A.,
1567 Lance, S., Moore, R. H., Murphy, D. M., Nenes, A., Novelli, P. C., Nowak, J. B., Ogren,
1568 J. A., Peischl, J., Pierce, R. B., Pilewskie, P., Quinn, P. K., Ryerson, T. B., Schmidt, K.
1569 S., Schwarz, J. P., Sodemann, H., Spackman, J. R., Stark, H., Thomson, D. S.,
1570 Thornberry, T., Veres, P., Watts, L. A., Warneke, C., and Wollny, A. G., Characteristics,
1571 sources, and transport of aerosols measured in spring 2008 during the aerosol, radiation,
1572 and cloud processes affecting Arctic Climate (ARCPAC) Project: *Atmos. Chem. Phys.*,
1573 11, 2423-2453, doi:10.5194/acp-11-2423-2011, 2011.

1574 Browell, E. V., Fenn, M. A., Butler, C. F., Grant, W. B., Clayton, M. E., Fishman, J., Bachmeier,
1575 A. S., Anderson, B. E., Gregory, G. L., Fuelberg, H. E., Bradshaw, J. D., Sandholm, S.
1576 T., Blake, D. R., Heikes, B. G., Sachse, G. W., Singh, H. B., and Talbot, R. W., Ozone

1577 and aerosol distributions and air mass characteristics over the South Atlantic basin during
1578 the burning season: *J. Geophys. Res.*, 101, 24,043-24,068, 1996.

1579 Bruns, E. A., Perraud, V., Zelenyuk, A., Ezell, M. J., Johnson, S. N., Yu, Y., Imre, D.,
1580 Finlayson-Pitts, B. J., and Alexander, M. L., Comparison of FTIR and particle mass
1581 spectrometry for the measurement of particulate organic nitrates: *Environ. Sci. Technol.*,
1582 44, 1056-1061, doi:10.1021/es9029864, 2010.

1583 Cai, Y., Montague, D. C., Mooiweer-Bryan, W., and Deshler, T., Performance characteristics of
1584 the ultra high sensitivity aerosol spectrometer for particles between 55 and 800 nm:
1585 Laboratory and field studies: *J. Aerosol Sci.*, 39, 759-769,
1586 doi:10.1016/j.jaerosci.2008.04.007, 2008.

1587 Carslaw, K. S., Lee, L. A., Reddington, C. L., Pringle, K. J., Rap, A., Forster, P. M., Mann, G.
1588 W., Spracklen, D. V., Woodhouse, M. T., Regayre, L. A., and Pierce, J. R., Large
1589 contribution of natural aerosols to uncertainty in indirect forcing: *Nature*, 503, 67-71,
1590 doi:10.1038/nature12674, 2013.

1591 Carslaw, K. S., Gordon, H., Hamilton, D. S., Johnson, J. S., Regayre, L. A., Yoshioka, M., and
1592 Pringle, K. J., Aerosols in the pre-industrial atmosphere: *Current Climate Change*
1593 *Reports*, 3, 1-15, doi:10.1007/s40641-017-0061-2, 2017.

1594 Cecchini, M. A., Machado, L. A. T., Andreae, M. O., Martin, S. T., Albrecht, R. I., Artaxo, P.,
1595 Barbosa, H. M. J., Borrmann, S., Fütterer, D., Jurkat, T., Mahnke, C., Minikin, A.,
1596 Molleker, S., Pöhlker, M. L., Pöschl, U., Rosenfeld, D., Voigt, C., Weinzierl, B., and
1597 Wendisch, M., Sensitivities of Amazonian clouds to aerosols and updraft speed: *Atmos.*
1598 *Chem. Phys.*, 17, 10,037-10,050, doi:10.5194/acp-17-10037-2017, 2017.

1599 Chubb, T., Huang, Y., Jensen, J., Campos, T., Siems, S., and Manton, M., Observations of high
1600 droplet number concentrations in Southern Ocean boundary layer clouds: *Atmos. Chem.*
1601 *Phys.*, 16, 971-987, doi:10.5194/acp-16-971-2016, 2016.

1602 Clarke, A., and Kapustin, V., Hemispheric aerosol vertical profiles: Anthropogenic impacts on
1603 optical depth and cloud nuclei: *Science*, 329, 1488-1492, 2010.

1604 Clarke, A. D., Atmospheric nuclei in the remote free troposphere: *J. Atmos. Chem.*, 14, 479-488,
1605 doi:10.1007/bf00115252, 1992.

1606 Clarke, A. D., Atmospheric nuclei in the Pacific midtroposphere - their nature, concentration,
1607 and evolution: *J. Geophys. Res.*, 98, 20,633-20,647, doi:10.1029/93jd00797, 1993.

1608 Clarke, A. D., Varner, J. L., Eisele, F., Mauldin, R. L., Tanner, D., and Litchy, M., Particle
1609 production in the remote marine atmosphere: Cloud outflow and subsidence during ACE
1610 1: *J. Geophys. Res.*, 103, 16,397-16,409, doi:10.1029/97jd02987, 1998.

1611 Clarke, A. D., Eisele, F., Kapustin, V. N., Moore, K., Tanner, D., Mauldin, L., Litchy, M.,
1612 Lienert, B., Carroll, M. A., and Albercook, G., Nucleation in the equatorial free
1613 troposphere: Favorable environments during PEM-Tropics: *J. Geophys. Res.*, 104, 5735-
1614 5744, doi:10.1029/98JD02303, 1999.

1615 Clarke, A. D., and Kapustin, V. N., A Pacific aerosol survey. Part I: A decade of data on particle
1616 production, transport, evolution, and mixing in the troposphere: *J. Atmos. Sci.*, 59, 363-
1617 382, 2002.

1618 Clarke, A. D., Freitag, S., Simpson, R. M. C., Hudson, J. G., Howell, S. G., Brekhovskikh, V. L.,
 1619 Campos, T., Kapustin, V. N., and Zhou, J., Free troposphere as a major source of CCN
 1620 for the Equatorial Pacific boundary layer: long-range transport and teleconnections:
 1621 Atmos. Chem. Phys., 13, 7511-7529, doi:10.5194/acp-13-7511-2013, 2013.

1622 Collow, A. B. M., Miller, M. A., and Trabachino, L. C., Cloudiness over the Amazon rainforest:
 1623 Meteorology and thermodynamics: J. Geophys. Res., 121, 7990-8005,
 1624 doi:10.1002/2016JD024848, 2016.

1625 Colomb, A., Williams, J., Crowley, J., Gros, V., Hofmann, R., Salisbury, G., Klupfel, T.,
 1626 Kormann, R., Stickler, A., Forster, C., and Lelieveld, J., Airborne measurements of trace
 1627 organic species in the upper troposphere over Europe: the impact of deep convection:
 1628 Environmental Chemistry, 3, 244-259, doi:10.1071/en06020, 2006.

1629 Cubison, M. J., Ortega, A. M., Hayes, P. L., Farmer, D. K., Day, D., Lechner, M. J., Brune, W.
 1630 H., Apel, E., Diskin, G. S., Fisher, J. A., Fuelberg, H. E., Hecobian, A., Knapp, D. J.,
 1631 Mikoviny, T., Riemer, D., Sachse, G. W., Sessions, W., Weber, R. J., Weinheimer, A. J.,
 1632 Wisthaler, A., and Jimenez, J. L., Effects of aging on organic aerosol from open biomass
 1633 burning smoke in aircraft and laboratory studies: Atmos. Chem. Phys., 11, 12,049-
 1634 12,064, doi:10.5194/acp-11-12049-2011, 2011.

1635 Dagan, G., Koren, I., Altaratz, O., and Heiblum, R. H., Aerosol effect on the evolution of the
 1636 thermodynamic properties of warm convective cloud fields: Scientific Reports, 6, 38769,
 1637 doi:10.1038/srep38769, 2016.

1638 de Reus, M., Krejci, R., Williams, J., Fischer, H., Scheele, R., and Strom, J., Vertical and
 1639 horizontal distributions of the aerosol number concentration and size distribution over the
 1640 northern Indian Ocean: J. Geophys. Res., 106, 28,629-28,641, 2001.

1641 Drewnick, F., Hings, S. S., DeCarlo, P., Jayne, J. T., Gonin, M., Fuhrer, K., Weimer, S.,
 1642 Jimenez, J. L., Demerjian, K. L., Borrmann, S., and Worsnop, D. R., A new time-of-
 1643 flight aerosol mass spectrometer (TOF-AMS) - Instrument description and first field
 1644 deployment: Aerosol Sci. Tech., 39, 637-658, 2005.

1645 Dunne, E. M., Gordon, H., Kürten, A., Almeida, J., Duplissy, J., Williamson, C., Ortega, I. K.,
 1646 Pringle, K. J., Adamov, A., Baltensperger, U., Barmet, P., Benduhn, F., Bianchi, F.,
 1647 Breitenlechner, M., Clarke, A., Curtius, J., Dommen, J., Donahue, N. M., Ehrhart, S.,
 1648 Flagan, R. C., Franchin, A., Guida, R., Hakala, J., Hansel, A., Heinritzi, M., Jokinen, T.,
 1649 Kangasluoma, J., Kirkby, J., Kulmala, M., Kupc, A., Lawler, M. J., Lehtipalo, K.,
 1650 Makhmutov, V., Mann, G., Mathot, S., Merikanto, J., Miettinen, P., Nenes, A., Onnela,
 1651 A., Rap, A., Reddington, C. L. S., Riccobono, F., Richards, N. A. D., Rissanen, M. P.,
 1652 Rondo, L., Sarnela, N., Schobesberger, S., Sengupta, K., Simon, M., Sipilä, M., Smith, J.
 1653 N., Stozkhov, Y., Tomé, A., Tröstl, J., Wagner, P. E., Wimmer, D., Winkler, P. M.,
 1654 Worsnop, D. R., and Carslaw, K. S., Global atmospheric particle formation from CERN
 1655 CLOUD measurements: Science, 354, 1119-1124, doi:10.1126/science.aaf2649, 2016.

1656 Ehn, M., Thornton, J. A., Kleist, E., Sipilä, M., Junninen, H., Pullinen, I., Springer, M., Rubach,
 1657 F., Tillmann, R., Lee, B., Lopez-Hilfiker, F., Andres, S., Acir, I. H., Rissanen, M.,
 1658 Jokinen, T., Schobesberger, S., Kangasluoma, J., Kontkanen, J., Nieminen, T., Kurten,
 1659 T., Nielsen, L. B., Jorgensen, S., Kjaergaard, H. G., Canagaratna, M., Dal Maso, M.,
 1660 Berndt, T., Petaja, T., Wahner, A., Kerminen, V. M., Kulmala, M., Worsnop, D. R.,

1661 Wildt, J., and Mentel, T. F., A large source of low-volatility secondary organic aerosol:
 1662 Nature, 506, 476-479, doi:10.1038/nature13032, 2014.

1663 Ekman, A. M. L., Wang, C., Strom, J., and Krejci, R., Explicit simulation of aerosol physics in a
 1664 cloud-resolving model: Aerosol transport and processing in the free troposphere: J.
 1665 Atmos. Sci., 63, 682-696, 2006.

1666 Ekman, A. M. L., Krejci, R., Engström, A., Ström, J., de Reus, M., Williams, J., and Andreae,
 1667 M. O., Do organics contribute to small particle formation in the Amazonian upper
 1668 troposphere?: Geophys. Res. Lett., 35, L17810, doi:10.1029/2008GL034970, 2008.

1669 Ekman, A. M. L., Hermann, M., Gross, P., Heintzenberg, J., Kim, D., and Wang, C., Sub-
 1670 micrometer aerosol particles in the upper troposphere/lowermost stratosphere as
 1671 measured by CARIBIC and modeled using the MIT-CAM3 global climate model: J.
 1672 Geophys. Res., 117, D11202, doi:10.1029/2011jd016777, 2012.

1673 Engelhart, G. J., Asa-Awuku, A., Nenes, A., and Pandis, S. N., CCN activity and droplet growth
 1674 kinetics of fresh and aged monoterpene secondary organic aerosol: Atmos. Chem. Phys.,
 1675 8, 3937-3949, 2008.

1676 Engelhart, G. J., Moore, R. H., Nenes, A., and Pandis, S. N., Cloud condensation nuclei activity
 1677 of isoprene secondary organic aerosol: J. Geophys. Res., 116, D02207,
 1678 doi:10.1029/2010jd014706, 2011.

1679 Engström, A., Ekman, A. M. L., Krejci, R., Strom, J., de Reus, M., and Wang, C., Observational
 1680 and modelling evidence of tropical deep convective clouds as a source of mid-
 1681 tropospheric accumulation mode aerosols: Geophys. Res. Lett., 35, L23813,
 1682 doi:10.1029/2008gl035817, 2008.

1683 Fan, J. W., Rosenfeld, D., Ding, Y. N., Leung, L. R., and Li, Z. Q., Potential aerosol indirect
 1684 effects on atmospheric circulation and radiative forcing through deep convection:
 1685 Geophys. Res. Lett., 39, L09806, doi:10.1029/2012gl051851, 2012.

1686 Fishman, J., Fakhruzzaman, K., Cros, B., and Nganga, D., Identification of widespread pollution
 1687 in the southern hemisphere deduced from satellite analyses: Science, 252, 1693-1696,
 1688 1991.

1689 Fishman, J., Brackett, V. G., Browell, E. V., and Grant, W. B., Tropospheric ozone derived from
 1690 TOMS/SBUV measurements during TRACE-A: J. Geophys. Res., 101, 24,069-24,082,
 1691 1996.

1692 Frey, W., Borrmann, S., Kunkel, D., Weigel, R., de Reus, M., Schlager, H., Roiger, A., Voigt,
 1693 C., Hoor, P., Curtius, J., Kraemer, M., Schiller, C., Volk, C. M., Homan, C. D., Fierli, F.,
 1694 Di Donfrancesco, G., Ulanovsky, A., Ravegnani, F., Sitnikov, N. M., Viciani, S.,
 1695 D'Amato, F., Shur, G. N., Belyaev, G. V., Law, K. S., and Cairo, F., In situ
 1696 measurements of tropical cloud properties in the West African Monsoon: upper
 1697 tropospheric ice clouds, Mesoscale Convective System outflow, and subvisual cirrus:
 1698 Atmos. Chem. Phys., 11, 5569-5590, doi:10.5194/acp-11-5569-2011, 2011.

1699 Froyd, K. D., Murphy, D. M., Sanford, T. J., Thomson, D. S., Wilson, J. C., Pfister, L., and Lait,
 1700 L., Aerosol composition of the tropical upper troposphere: Atmos. Chem. Phys., 9, 4363-
 1701 4385, 2009.

1702 Fry, J. L., Kiendler-Scharr, A., Rollins, A. W., Wooldridge, P. J., Brown, S. S., Fuchs, H., Dube,
 1703 W., Mensah, A., dal Maso, M., Tillmann, R., Dorn, H. P., Brauers, T., and Cohen, R. C.,
 1704 Organic nitrate and secondary organic aerosol yield from NO₃ oxidation of beta-pinene
 1705 evaluated using a gas-phase kinetics/aerosol partitioning model: *Atmos. Chem. Phys.*, 9,
 1706 1431-1449, 2009.

1707 Fu, R., Zhu, B., and Dickinson, R. E., How do atmosphere and land surface influence seasonal
 1708 changes of convection in the tropical Amazon?: *J. Clim.*, 12, 1306-1321, 1999.

1709 Fueglistaler, S., Dessler, A. E., Dunkerton, T. J., Folkins, I., Fu, Q., and Mote, P. W., Tropical
 1710 tropopause layer: *Rev. Geophys.*, 47, RG1004, doi:10.1029/2008rg000267, 2009.

1711 Gerbig, C., Schmitgen, S., Kley, D., Volz-Thomas, A., Dewey, K., and Haaks, D., An improved
 1712 fast-response vacuum-UV resonance fluorescence CO instrument: *J. Geophys. Res.*, 104,
 1713 1699-1704, doi:10.1029/1998jd100031, 1999.

1714 Gerken, T., Wei, D., Chase, R. J., Fuentes, J. D., Schumacher, C., Machado, L. A. T., Andreoli,
 1715 R. V., Chamecki, M., Ferreira de Souza, R. A., Freire, L. S., Jardine, A. B., Manzi, A. O.,
 1716 Nascimento dos Santos, R. M., von Randow, C., dos Santos Costa, P., Stoy, P. C., Tóta,
 1717 J., and Trowbridge, A. M., Downward transport of ozone rich air and implications for
 1718 atmospheric chemistry in the Amazon rainforest: *Atmospheric Environment*, 124, 64-76,
 1719 doi:10.1016/j.atmosenv.2015.11.014, 2016.

1720 Giangrande, S. E., Feng, Z., Jensen, M. P., Comstock, J., Johnson, K. L., Toto, T., Wang, M.,
 1721 Burleyson, C., Mei, F., Machado, L. A. T., Manzi, A., Xie, S., Tang, S., Silva Dias, M. A.
 1722 F., de Souza, R. A. F., Schumacher, C., and Martin, S. T., Cloud Characteristics,
 1723 Thermodynamic Controls and Radiative Impacts During the Observations and Modeling
 1724 of the Green Ocean Amazon (GoAmazon2014/5) Experiment: *Atmos. Chem. Phys.*
 1725 Discuss., 2017, 1-41, doi:10.5194/acp-2017-452, 2017.

1726 Gonçalves, W. A., Machado, L. A. T., and Kirstetter, P. E., Influence of biomass aerosol on
 1727 precipitation over the Central Amazon: an observational study: *Atmos. Chem. Phys.*, 15,
 1728 6789-6800, doi:10.5194/acp-15-6789-2015, 2015.

1729 Gordon, H., Sengupta, K., Rap, A., Duplissy, J., Frege, C., Williamson, C., Heinritzi, M., Simon,
 1730 M., Yan, C., Almeida, J., Tröstl, J., Nieminen, T., Ortega, I. K., Wagner, R., Dunne, E.
 1731 M., Adamov, A., Amorim, A., Bernhammer, A.-K., Bianchi, F., Breitenlechner, M.,
 1732 Brilke, S., Chen, X., Craven, J. S., Dias, A., Ehrhart, S., Fischer, L., Flagan, R. C.,
 1733 Franchin, A., Fuchs, C., Guida, R., Hakala, J., Hoyle, C. R., Jokinen, T., Junninen, H.,
 1734 Kangasluoma, J., Kim, J., Kirkby, J., Krapf, M., Kürten, A., Laaksonen, A., Lehtipalo,
 1735 K., Makhmutov, V., Mathot, S., Molteni, U., Monks, S. A., Onnela, A., Peräkylä, O.,
 1736 Piel, F., Petäjä, T., Praplan, A. P., Pringle, K. J., Richards, N. A. D., Rissanen, M. P.,
 1737 Rondo, L., Sarnela, N., Schobesberger, S., Scott, C. E., Seinfeld, J. H., Sharma, S., Sipilä,
 1738 M., Steiner, G., Stozhkov, Y., Stratmann, F., Tomé, A., Virtanen, A., Vogel, A. L.,
 1739 Wagner, A. C., Wagner, P. E., Weingartner, E., Wimmer, D., Winkler, P. M., Ye, P.,
 1740 Zhang, X., Hansel, A., Dommen, J., Donahue, N. M., Worsnop, D. R., Baltensperger, U.,
 1741 Kulmala, M., Curtius, J., and Carslaw, K. S., Reduced anthropogenic aerosol radiative
 1742 forcing caused by biogenic new particle formation: *Proc. Natl. Acad. Sci.*, 113, 12,053-
 1743 12,058, doi:10.1073/pnas.1602360113, 2016.

- 1744 Grant, D. D., Fuentes, J. D., DeLonge, M. S., Chan, S., Joseph, E., Kucera, P., Ndiaye, S. A., and
1745 Gaye, A. T., Ozone transport by mesoscale convective storms in western Senegal:
1746 *Atmospheric Environment*, 42, 7104-7114, doi:10.1016/j.atmosenv.2008.05.044, 2008.
- 1747 Gunthe, S. S., King, S. M., Rose, D., Chen, Q., Roldin, P., Farmer, D. K., Jimenez, J. L., Artaxo,
1748 P., Andreae, M. O., Martin, S. T., and Pöschl, U., Cloud condensation nuclei in pristine
1749 tropical rainforest air of Amazonia: size-resolved measurements and modeling of
1750 atmospheric aerosol composition and CCN activity: *Atmos. Chem. Phys.*, 9, 7551–7575,
1751 2009.
- 1752 Heald, C. L., Jacob, D. J., Park, R. J., Russell, L. M., Huebert, B. J., Seinfeld, J. H., Liao, H., and
1753 Weber, R. J., A large organic aerosol source in the free troposphere missing from current
1754 models: *Geophys. Res. Lett.*, 32, L18809, doi:10.1029/2005GL023831, 2005.
- 1755 Heintzenberg, J., Birmili, W., Otto, R., Andreae, M. O., Mayer, J.-C., Chi, X., and Panov, A.,
1756 Aerosol particle number size distributions and particulate light absorption at the ZOTTO
1757 tall tower (Siberia), 2006-2009: *Atmos. Chem. Phys.*, 11, 8703-8719, 2011.
- 1758 Holanda, B. A., Wang, Q., Saturno, J., Ditas, F., Ditas, J., Pöhlker, M., Klimach, T., Moran, D.,
1759 Schulz, C., Ming, J., Cheng, Y., Su, H., Wendisch, M., Machado, L. A. T., Schneider, J.,
1760 Pöhlker, C., Artaxo, P., Pöschl, U., and Andreae, M., Transatlantic transport of pollution
1761 aerosol from Africa to the Amazon rain forest - Aircraft observations in the context of the
1762 ACRIDICON-CHUVA campaign: *Atmos. Chem. Phys. Discuss.*, 2017, in preparation.
- 1763 Hu, W. W., Campuzano-Jost, P., Palm, B. B., Day, D. A., Ortega, A. M., Hayes, P. L.,
1764 Krechmer, J. E., Chen, Q., Kuwata, M., Liu, Y. J., de Sa, S. S., McKinney, K., Martin, S.
1765 T., Hu, M., Budisulistiorini, S. H., Riva, M., Surratt, J. D., St Clair, J. M., Isaacman-Van
1766 Wertz, G., Yee, L. D., Goldstein, A. H., Carbone, S., Brito, J., Artaxo, P., de Gouw, J. A.,
1767 Koss, A., Wisthaler, A., Mikoviny, T., Karl, T., Kaser, L., Jud, W., Hansel, A., Docherty,
1768 K. S., Alexander, M. L., Robinson, N. H., Coe, H., Allan, J. D., Canagaratna, M. R.,
1769 Paulot, F., and Jimenez, J. L., Characterization of a real-time tracer for isoprene
1770 epoxydiols-derived secondary organic aerosol (IEPOX-SOA) from aerosol mass
1771 spectrometer measurements: *Atmos. Chem. Phys.*, 15, 11,807-11,833, doi:10.5194/acp-
1772 15-11807-2015, 2015.
- 1773 Hu, X. M., Fuentes, J. D., and Zhang, F. Q., Downward transport and modification of
1774 tropospheric ozone through moist convection: *J. Atmos. Chem.*, 65, 13-35,
1775 doi:10.1007/s10874-010-9179-5, 2010.
- 1776 Huntrieser, H., Lichtenstern, M., Scheibe, M., Aufmhoff, H., Schlager, H., Pucik, T., Minikin,
1777 A., Weinzierl, B., Heimerl, K., Futterer, D., Rappengluck, B., Ackermann, L., Pickering,
1778 K. E., Cummings, K. A., Biggstaff, M. I., Betten, D. P., Honomichl, S., and Barth, M.
1779 C., On the origin of pronounced O₃ gradients in the thunderstorm outflow region during
1780 DC3: *J. Geophys. Res.*, 121, 6600-6637, doi:10.1002/2015jd024279, 2016.
- 1781 Janhäll, S., Andreae, M. O., and Pöschl, U., Biomass burning aerosol emissions from vegetation
1782 fires: particle number and mass emission factors and size distributions: *Atmos. Chem.*
1783 *Phys.*, 10, 1427-1439, 2010.
- 1784 Jiang, J. H., Su, H., Schoeberl, M. R., Massie, S. T., Colarco, P., Platnick, S., and Livesey, N. J.,
1785 Clean and polluted clouds: Relationships among pollution, ice clouds, and precipitation
1786 in South America: *Geophys. Res. Lett.*, 35, L14804, doi:10.1029/2008GL034631, 2008.

- 1787 Jimenez, J. L., Canagaratna, M. R., Donahue, N. M., Prevot, A. S. H., Zhang, Q., Kroll, J. H.,
 1788 DeCarlo, P. F., Allan, J. D., Coe, H., Ng, N. L., Aiken, A. C., Docherty, K. D., Ulbrich, I.
 1789 M., Grieshop, A. P., Robinson, A. L., Duplissy, J., Smith, J. D., Wilson, K. R., Lanz, V.
 1790 A., Hueglin, C., Sun, Y. L., Tian, J., Laaksonen, A., Raatikainen, T., Rautiainen, J.,
 1791 Vaattovaara, P., Ehn, M., Kulmala, M., Tomlinson, J. M., Collins, D. R., Cubison, M. J.,
 1792 Dunlea, E. J., Huffman, J. A., Onasch, T. B., Alfarra, M. R., Williams, P. I., Bower, K.,
 1793 Kondo, Y., Schneider, J., Drewnick, F., Borrmann, S., Weimer, S., Demerjian, K.,
 1794 Salcedo, D., Cottrell, L., Griffin, R., Takami, A., Miyoshi, T., Hatakeyama, S., Shimono,
 1795 A., Sun, J. Y., Zhang, Y. M., Dzepina, K., Kimmel, J. R., Sueper, D., Jayne, J. T.,
 1796 Herndon, S. C., Trimborn, A. M., Williams, L. R., Wood, E. C., Kolb, C. E.,
 1797 Baltensperger, U., and Worsnop, D. R., Evolution of organic aerosols in the atmosphere:
 1798 Science, 326, 1525-529, doi:10.1126/science.1180353, 2009.
- 1799 Jokinen, T., Berndt, T., Makkonen, R., Kerminen, V.-M., Junninen, H., Paasonen, P., Stratmann,
 1800 F., Herrmann, H., Guenther, A. B., Worsnop, D. R., Kulmala, M., Ehn, M., and Sipilä,
 1801 M., Production of extremely low volatile organic compounds from biogenic emissions:
 1802 Measured yields and atmospheric implications: Proc. Natl. Acad. Sci., 112, 7123-7128,
 1803 doi:10.1073/pnas.1423977112, 2015.
- 1804 Katoshevski, D., Nenes, A., and Seinfeld, J. H., A study of processes that govern the
 1805 maintenance of aerosols in the marine boundary layer: J. Aerosol Sci., 30, 503-532, 1999.
- 1806 Khain, A. P., Phillips, V., Benmoshe, N., and Pokrovsky, A., The role of small soluble aerosols
 1807 in the microphysics of deep maritime clouds: J. Atmos. Sci., 69, 2787-2807,
 1808 doi:10.1175/2011jas3649.1, 2012.
- 1809 Kirkby, J., Duplissy, J., Sengupta, K., Frege, C., Gordon, H., Williamson, C., Heinritzi, M.,
 1810 Simon, M., Yan, C., Almeida, J., Tröstl, J., Nieminen, T., Ortega, I. K., Wagner, R.,
 1811 Adamov, A., Amorim, A., Bernhammer, A.-K., Bianchi, F., Breitenlechner, M., Brilke,
 1812 S., Chen, X., Craven, J., Dias, A., Ehrhart, S., Flagan, R. C., Franchin, A., Fuchs, C.,
 1813 Guida, R., Hakala, J., Hoyle, C. R., Jokinen, T., Junninen, H., Kangasluoma, J., Kim, J.,
 1814 Krapf, M., Kürten, A., Laaksonen, A., Lehtipalo, K., Makhmutov, V., Mathot, S.,
 1815 Molteni, U., Onnela, A., Peräkylä, O., Piel, F., Petäjä, T., Praplan, A. P., Pringle, K., Rap,
 1816 A., Richards, N. A. D., Riipinen, I., Rissanen, M. P., Rondo, L., Sarnela, N.,
 1817 Schobesberger, S., Scott, C. E., Seinfeld, J. H., Sipilä, M., Steiner, G., Stozhkov, Y.,
 1818 Stratmann, F., Tomé, A., Virtanen, A., Vogel, A. L., Wagner, A. C., Wagner, P. E.,
 1819 Weingartner, E., Wimmer, D., Winkler, P. M., Ye, P., Zhang, X., Hansel, A., Dommen,
 1820 J., Donahue, N. M., Worsnop, D. R., Baltensperger, U., Kulmala, M., Carslaw, K. S., and
 1821 Curtius, J., Ion-induced nucleation of pure biogenic particles: Nature, 533, 521-526,
 1822 doi:10.1038/nature17953, 2016.
- 1823 Kojima, T., Buseck, P. R., Wilson, J. C., Reeves, J. M., and Mahoney, M. J., Aerosol particles
 1824 from tropical convective systems: Cloud tops and cirrus anvils: J. Geophys. Res., 109,
 1825 D12201, 2004.
- 1826 Koren, I., Martins, J. V., Remer, L. A., and Afargan, H., Smoke invigoration versus inhibition of
 1827 clouds over the Amazon: Science 321, 946-949, 2008.

- 1828 Koren, I., Remer, L. A., Altaratz, O., Martins, J. V., and Davidi, A., Aerosol-induced changes of
1829 convective cloud anvils produce strong climate warming: *Atmos. Chem. Phys.*, 10, 5001-
1830 5010, doi:10.5194/acp-10-5001-2010, 2010.
- 1831 Kottayil, A., and Satheesan, K., Enhancement in the upper tropospheric humidity associated with
1832 aerosol loading over tropical Pacific: *Atmospheric Environment*, 122, 148-153,
1833 doi:10.1016/j.atmosenv.2015.09.043, 2015.
- 1834 Krejci, R., Strom, J., de Reus, M., Hoor, P., Williams, J., Fischer, H., and Hansson, H. C.,
1835 Evolution of aerosol properties over the rain forest in Surinam, South America, observed
1836 from aircraft during the LBA-CLAIRE 98 experiment: *J. Geophys. Res.*, 108, 4561,
1837 doi:10.1029/2001JD001375, 2003.
- 1838 Krüger, M. L., Mertes, S., Klimach, T., Cheng, Y., Su, H., Schneider, J., Andreae, M. O., Pöschl,
1839 U., and Rose, D., Assessment of cloud supersaturation by size-resolved aerosol particle
1840 and cloud condensation nuclei (CCN) measurements: *Atmos. Meas. Tech.*, 7, 2615–2629,
1841 doi:10.5194/amt-7-2615-2014, 2014.
- 1842 Kulmala, M., Reissell, A., Sipila, M., Bonn, B., Ruuskanen, T. M., Lehtinen, K. E. J., Kerminen,
1843 V.-M., and Strom, J., Deep convective clouds as aerosol production engines: Role of
1844 insoluble organics: *J. Geophys. Res.*, 111, D17202, doi:10.1029/2005jd006963, 2006.
- 1845 Kulmala, M., and Kerminen, V. M., On the formation and growth of atmospheric nanoparticles:
1846 *Atmos. Res.*, 90, 132-150, doi:10.1016/j.atmosres.2008.01.005, 2008.
- 1847 Laaksonen, A., Kulmala, M., O'Dowd, C. D., Joutsensaari, J., Vaattovaara, P., Mikkonen, S.,
1848 Lehtinen, K. E. J., Sogacheva, L., Dal Maso, M., Aalto, P., Petaja, T., Sogachev, A.,
1849 Yoon, Y. J., Lihavainen, H., Nilsson, D., Facchini, M. C., Cavalli, F., Fuzzi, S.,
1850 Hoffmann, T., Arnold, F., Hanke, M., Sellegri, K., Umann, B., Junkermann, W., Coe, H.,
1851 Allan, J. D., Alfarra, M. R., Worsnop, D. R., Riekkola, M. L., Hyotylainen, T., and
1852 Viisanen, Y., The role of VOC oxidation products in continental new particle formation:
1853 *Atmos. Chem. Phys.*, 8, 2657-2665, 2008.
- 1854 Laborde, M., Crippa, M., Tritscher, T., Juranyi, Z., Decarlo, P. F., Temime-Roussel, B.,
1855 Marchand, N., Eckhardt, S., Stohl, A., Baltensperger, U., Prevot, A. S. H., Weingartner,
1856 E., and Gysel, M., Black carbon physical properties and mixing state in the European
1857 megacity Paris: *Atmos. Chem. Phys.*, 13, 5831-5856, doi:10.5194/acp-13-5831-2013,
1858 2013.
- 1859 Lee, L., Wooldridge, P. J., Gilman, J. B., Warneke, C., de Gouw, J., and Cohen, R. C., Low
1860 temperatures enhance organic nitrate formation: evidence from observations in the 2012
1861 Uintah Basin Winter Ozone Study: *Atmos. Chem. Phys.*, 14, 12,441-12,454,
1862 doi:10.5194/acp-14-12441-2014, 2014.
- 1863 Lee, S. H., Reeves, J. M., Wilson, J. C., Hunton, D. E., Viggiano, A. A., Miller, T. M.,
1864 Ballenthin, J. O., and Lait, L. R., Particle formation by ion nucleation in the upper
1865 troposphere and lower stratosphere: *Science*, 301, 1886-1889,
1866 doi:10.1126/science.1087236, 2003.
- 1867 Lee, S. H., Wilson, J. C., Baumgardner, D., Herman, R. L., Weinstock, E. M., LaFleur, B. G.,
1868 Kok, G., Anderson, B., Lawson, P., Baker, B., Strawa, A., Pittman, J. V., Reeves, J. M.,

1869 and Bui, T. P., New particle formation observed in the tropical/subtropical cirrus clouds:
1870 J. Geophys. Res., 109, D20209, doi:10.1029/2004jd005033, 2004.

1871 Machado, L. A. T., Laurent, H., Dessay, N., and Miranda, I., Seasonal and diurnal variability of
1872 convection over the Amazonia: A comparison of different vegetation types and large
1873 scale forcing: Theoretical and Applied Climatology, 78, 61-77, doi:10.1007/s00704-004-
1874 0044-9, 2004.

1875 Martin, S. T., Andreae, M. O., Artaxo, P., Baumgardner, D., Chen, Q., Goldstein, A. H.,
1876 Guenther, A., Heald, C. L., Mayol-Bracero, O. L., McMurry, P. H., Pauliquevis, T.,
1877 Pöschl, U., Prather, K. A., Roberts, G. C., Saleska, S. R., Dias, M. A. S., Spracklen, D.,
1878 Swietlicki, E., and Trebs, I., Sources and properties of Amazonian aerosol particles: Rev.
1879 Geophys., 48, RG2002, doi:10.1029/2008RG000280, 2010.

1880 Martin, S. T., Artaxo, P., Machado, L. A. T., Manzi, A. O., Souza, R. A. F., Schumacher, C.,
1881 Wang, J., Andreae, M. O., Barbosa, H. M. J., Fan, J., Fisch, G., Goldstein, A. H.,
1882 Guenther, A., Jimenez, J. L., Pöschl, U., Silva Dias, M. A., Smith, J. N., and Wendisch,
1883 M., Introduction: Observations and modeling of the Green Ocean Amazon
1884 (GoAmazon2014/5): Atmos. Chem. Phys., 16, 4785-4797, doi:10.5194/acp-16-4785-
1885 2016, 2016.

1886 Merikanto, J., Spracklen, D. V., Mann, G. W., Pickering, S. J., and Carslaw, K. S., Impact of
1887 nucleation on global CCN: Atmos. Chem. Phys., 9, 8601-8616, 2009.

1888 Metzger, A., Verheggen, B., Dommen, J., Duplissy, J., Prevot, A. S. H., Weingartner, E.,
1889 Riipinen, I., Kulmala, M., Spracklen, D. V., Carslaw, K. S., and Baltensperger, U.,
1890 Evidence for the role of organics in aerosol particle formation under atmospheric
1891 conditions: Proc. Natl. Acad. Sci., doi:10.1073/pnas.0911330107, 2010.

1892 Mirme, S., Mirme, A., Minikin, A., Petzold, A., Horrak, U., Kerminen, V. M., and Kulmala, M.,
1893 Atmospheric sub-3 nm particles at high altitudes: Atmos. Chem. Phys., 10, 437-451,
1894 2010.

1895 Murphy, B. N., Julin, J., Riipinen, I., and Ekman, A. M. L., Organic aerosol processing in
1896 tropical deep convective clouds: Development of a new model (CRM-ORG) and
1897 implications for sources of particle number: J. Geophys. Res., 120, 10,441-10,464,
1898 doi:10.1002/2015JD023551, 2015.

1899 Newell, R. E., Thouret, V., Cho, J. Y. N., Stoller, P., Marengo, A., and Smit, H. G., Ubiquity of
1900 quasi-horizontal layers in the troposphere: Nature, 398, 316-319, 1999.

1901 Ng, N. L., Canagaratna, M. R., Jimenez, J. L., Chhabra, P. S., Seinfeld, J. H., and Worsnop, D.
1902 R., Changes in organic aerosol composition with aging inferred from aerosol mass
1903 spectra: Atmos. Chem. Phys., 11, 6465-6474, doi:10.5194/acp-11-6465-2011, 2011.

1904 Öström, E., Putian, Z., Schurgers, G., Mishurov, M., Kivekäs, N., Lihavainen, H., Ehn, M.,
1905 Rissanen, M. P., Kurtén, T., Boy, M., Swietlicki, E., and Roldin, P., Modeling the role of
1906 highly oxidized multifunctional organic molecules for the growth of new particles
1907 over the boreal forest region: Atmos. Chem. Phys., 17, 8887-8901, doi:10.5194/acp-17-
1908 8887-2017, 2017.

1909 Petters, M. D., and Kreidenweis, S. M., A single parameter representation of hygroscopic growth
1910 and cloud condensation nucleus activity: Atmos. Chem. Phys., 7, 1961-1971, 2007.

- 1911 Petzold, A., Marsh, R., Johnson, M., Miller, M., Sevcenco, Y., Delhay, D., Ibrahim, A.,
1912 Williams, P., Bauer, H., Crayford, A., Bachalo, W. D., and Raper, D., Evaluation of
1913 methods for measuring particulate matter emissions from gas turbines: *Environ. Sci.*
1914 *Technol.*, 45, 3562-3568, doi:10.1021/es103969v, 2011.
- 1915 Pöhlker, C., Wiedemann, K., Sinha, B., Shiraiwa, M., Gunthe, S., Smith, M., Su, H., Artaxo, P.,
1916 Chen, Q., Cheng, Y., Elbert, W., Gilles, M. K., Kilcoyne, A. L. D., Moffet, R. C.,
1917 Weigand, M., Martin, S. T., Pöschl, U., and Andreae, M. O., Biogenic potassium salt
1918 particles as seeds for secondary organic aerosol in the Amazon: *Science*, 337, 1075-1078,
1919 2012.
- 1920 Pöhlker, M. L., Pöhlker, C., Ditas, F., Klimach, T., Hrabě de Angelis, I., Araújo, A., Brito, J.,
1921 Carbone, S., Cheng, Y., Chi, X., Ditz, R., Gunthe, S. S., Kesselmeier, J., Könemann, T.,
1922 Lavrič, J. V., Martin, S. T., Mikhailov, E., Moran-Zuloaga, D., Rose, D., Saturno, J., Su,
1923 H., Thalman, R., Walter, D., Wang, J., Wolff, S., Barbosa, H. M. J., Artaxo, P., Andreae,
1924 M. O., and Pöschl, U., Long-term observations of cloud condensation nuclei in the
1925 Amazon rain forest – Part 1: Aerosol size distribution, hygroscopicity, and new model
1926 parametrizations for CCN prediction: *Atmos. Chem. Phys.*, 16, 15,709-15,740,
1927 doi:10.5194/acp-16-15709-2016, 2016.
- 1928 Pöschl, U., Martin, S. T., Sinha, B., Chen, Q., Gunthe, S. S., Huffman, J. A., Borrmann, S.,
1929 Farmer, D. K., Garland, R. M., Helas, G., Jimenez, J. L., King, S. M., Manzi, A.,
1930 Mikhailov, E., Pauliquevis, T., Petters, M. D., Prenni, A. J., Roldin, P., Rose, D.,
1931 Schneider, J., Su, H., Zorn, S. R., Artaxo, P., and Andreae, M. O., Rainforest aerosols as
1932 biogenic nuclei of clouds and precipitation in the Amazon: *Science*, 329, 1513-1516,
1933 2010.
- 1934 Raes, F., Entrainment of free tropospheric aerosols as a regulating mechanism for cloud
1935 condensation nuclei in the remote marine boundary layer: *J. Geophys. Res.*, 100, 2893-
1936 2903, 1995.
- 1937 Randel, W. J., and Jensen, E. J., Physical processes in the tropical tropopause layer and their
1938 roles in a changing climate: *Nature Geoscience*, 6, 169-176, doi:10.1038/ngeo1733, 2013.
- 1939 Reddington, C. L., Carslaw, K. S., Stier, P., Schutgens, N., Coe, H., Liu, D., Allan, J., Browse,
1940 J., Pringle, K. J., Lee, L. A., Yoshioka, M., Johnson, J. S., Regayre, L. A., Spracklen, D.
1941 V., Mann, G. W., Clarke, A., Hermann, M., Henning, S., Wex, H., Kristensen, T. B.,
1942 Leaitch, W. R., Pöschl, U., Rose, D., Andreae, M. O., Schmale, J., Kondo, Y., Oshima,
1943 N., Schwarz, J. P., Nenes, A., Anderson, B., Roberts, G. C., Snider, J. R., Leck, C.,
1944 Quinn, P. K., Chi, X., Ding, A., Jimenez, J. L., and Zhang, Q., The Global Aerosol
1945 Synthesis and Science Project (GASSP) - Measurements and modelling to reduce
1946 uncertainty: *Bull. Am. Meteorol. Soc.*, 2016, under review.
- 1947 Riccobono, F., Schobesberger, S., Scott, C. E., Dommen, J., Ortega, I. K., Rondo, L., Almeida,
1948 J., Amorim, A., Bianchi, F., Breitenlechner, M., David, A., Downard, A., Dunne, E. M.,
1949 Duplissy, J., Ehrhart, S., Flagan, R. C., Franchin, A., Hansel, A., Junninen, H., Kajos, M.,
1950 Keskinen, H., Kupc, A., Kürten, A., Kvashin, A. N., Laaksonen, A., Lehtipalo, K.,
1951 Makhmutov, V., Mathot, S., Nieminen, T., Onnela, A., Petäjä, T., Praplan, A. P., Santos,
1952 F. D., Schallhart, S., Seinfeld, J. H., Sipilä, M., Spracklen, D. V., Stozhkov, Y.,
1953 Stratmann, F., Tomé, A., Tsagkogeorgas, G., Vaattovaara, P., Viisanen, Y., Vrtala, A.,

- 1954 Wagner, P. E., Weingartner, E., Wex, H., Wimmer, D., Carslaw, K. S., Curtius, J.,
 1955 Donahue, N. M., Kirkby, J., Kulmala, M., Worsnop, D. R., and Baltensperger, U.,
 1956 Oxidation products of biogenic emissions contribute to nucleation of atmospheric
 1957 particles: *Science*, 344, 717-721, doi:10.1126/science.1243527, 2014.
- 1958 Riipinen, I., Pierce, J. R., Yli-Juuti, T., Nieminen, T., Hakkinen, S., Ehn, M., Junninen, H.,
 1959 Lehtipalo, K., Petaja, T., Slowik, J., Chang, R., Shantz, N. C., Abbatt, J., Leaitch, W. R.,
 1960 Kerminen, V. M., Worsnop, D. R., Pandis, S. N., Donahue, N. M., and Kulmala, M.,
 1961 Organic condensation: a vital link connecting aerosol formation to cloud condensation
 1962 nuclei (CCN) concentrations: *Atmos. Chem. Phys.*, 11, 3865-3878, doi:10.5194/acp-11-
 1963 3865-2011, 2011.
- 1964 Riipinen, I., Yli-Juuti, T., Pierce, J. R., Petaja, T., Worsnop, D. R., Kulmala, M., and Donahue,
 1965 N. M., The contribution of organics to atmospheric nanoparticle growth: *Nature*
 1966 *Geoscience*, 5, 453-458, doi:10.1038/ngeo1499, 2012.
- 1967 Rissler, J., Vestin, A., Swietlicki, E., Fisch, G., Zhou, J., Artaxo, P., and Andreae, M. O., Size
 1968 distribution and hygroscopic properties of aerosol particles from dry-season biomass
 1969 burning in Amazonia: *Atmos. Chem. Phys.*, 6, 471-491, 2006.
- 1970 Riuttanen, L., Bister, M., Kerminen, V. M., John, V. O., Sundstrom, A. M., Dal Maso, M.,
 1971 Raisanen, J., Sinclair, V. A., Makkonen, R., Xausa, F., de Leeuw, G., and Kulmala, M.,
 1972 Observational evidence for aerosols increasing upper tropospheric humidity: *Atmos.*
 1973 *Chem. Phys.*, 16, 14,331-14,342, doi:10.5194/acp-16-14331-2016, 2016.
- 1974 Rizzo, L. V., Artaxo, P., Müller, T., Wiedensohler, A., Paixão, M., Cirino, G. G., Arana, A.,
 1975 Swietlicki, E., Roldin, P., Fors, E. O., Wiedemann, K. T., Leal, L. S. M., and Kulmala,
 1976 M., Long term measurements of aerosol optical properties at a primary forest site in
 1977 Amazonia: *Atmos. Chem. Phys.*, 13, 2391-2413, doi:10.5194/acp-13-2391-2013, 2013.
- 1978 Roberts, G. C., and Andreae, M. O., Reply to "Comment on Cloud condensation nuclei in the
 1979 Amazon Basin: "Marine" conditions over a continent?" by P. J. Crutzen et al.: *Geophys.*
 1980 *Res. Lett.*, 30, doi:10.1029/2002GL015564, 2003.
- 1981 Roberts, G. C., and Nenes, A., A continuous-flow streamwise thermal-gradient CCN chamber
 1982 for atmospheric measurements: *Aerosol Sci. Tech.*, 39, 206-221, 2005.
- 1983 Robinson, N. H., Hamilton, J. F., Allan, J. D., Langford, B., Oram, D. E., Chen, Q., Docherty,
 1984 K., Farmer, D. K., Jimenez, J. L., Ward, M. W., Hewitt, C. N., Barley, M. H., Jenkin, M.
 1985 E., Rickard, A. R., Martin, S. T., McFiggans, G., and Coe, H., Evidence for a significant
 1986 proportion of Secondary Organic Aerosol from isoprene above a maritime tropical forest:
 1987 *Atmos. Chem. Phys.*, 11, 1039-1050, 2011.
- 1988 Rose, C., Sellegri, K., Moreno, I., Velarde, F., Ramonet, M., Weinhold, K., Krejci, R., Andrade,
 1989 M., Wiedensohler, A., Ginot, P., and Laj, P., CCN production by new particle formation
 1990 in the free troposphere: *Atmos. Chem. Phys.*, 17, 1529-1541, doi:10.5194/acp-17-1529-
 1991 2017, 2017.
- 1992 Rose, D., Gunthe, S. S., Mikhailov, E., Frank, G. P., Dusek, U., Andreae, M. O., and Pöschl, U.,
 1993 Calibration and measurement uncertainties of a continuous-flow cloud condensation
 1994 nuclei counter (DMT-CCNC): CCN activation of ammonium sulfate and sodium chloride
 1995 aerosol particles in theory and experiment: *Atmos. Chem. Phys.*, 8, 1153-1179, 2008.

1996 Rosenfeld, D., Lohmann, U., Raga, G. B., O'Dowd, C. D., Kulmala, M., Fuzzi, S., Reissell, A.,
1997 and Andreae, M. O., Flood or drought: How do aerosols affect precipitation?: Science,
1998 321, 1309-1313, 2008.

1999 Rosenfeld, D., Andreae, M. O., Asmi, A., Chin, M., de Leeuw, G., Donovan, D. P., Kahn, R.,
2000 Kinne, S., Kivekäs, N., Kulmala, M., Lau, W., Schmidt, K. S., Suni, T., Wagner, T.,
2001 Wild, M., and Quaas, J., Global observations of aerosol-cloud-precipitation-climate
2002 interactions: Rev. Geophys., 52, 750-808, doi:10.1002/2013RG000441, 2014.

2003 Saha, S., Moorthi, S., Wu, X., Wang, J., Nadiga, S., Tripp, P., Behringer, D., Hou, Y.-T.,
2004 Chuang, H.-y., Iredell, M., Ek, M., Meng, J., Yang, R., Mendez, M. P., Dool, H. v. d.,
2005 Zhang, Q., Wang, W., Chen, M., and Becker, E., NCEP Climate Forecast System Version
2006 2 (CFSv2) 6-hourly Products. Research Data Archive at the National Center for
2007 Atmospheric Research, Computational and Information Systems Laboratory. Accessed
2008 20 March 2017, <https://rda.ucar.edu/datasets/ds094.0/> (2017).

2009 Sahu, L. K., and Lal, S., Changes in surface ozone levels due to convective downdrafts over the
2010 Bay of Bengal: Geophys. Res. Lett., 33, L10807, doi:10.1029/2006gl025994, 2006.

2011 Schmale, J., Schneider, J., Jurkat, T., Voigt, C., Kalesse, H., Rautenhaus, M., Lichtenstern, M.,
2012 Schlager, H., Ancellet, G., Arnold, F., Gerding, M., Mattis, I., Wendisch, M., and
2013 Borrmann, S., Aerosol layers from the 2008 eruptions of Mount Okmok and Mount
2014 Kasatochi: In situ upper troposphere and lower stratosphere measurements of sulfate and
2015 organics over Europe: J. Geophys. Res., 115, D00107, doi:10.1029/2009jd013628, 2010.

2016 Schneider, J., Weimer, S., Drewnick, F., Borrmann, S., Helas, G., Gwaze, P., Schmid, O.,
2017 Andreae, M. O., and Kirchner, U., Mass spectrometric analysis and aerodynamic
2018 properties of various types of combustion-derived aerosol particles: Int. J. Mass Spec.,
2019 258, 37-49, 2006.

2020 Schulz, C., Schneider, J., Weinzierl, B., Sauer, D., Fütterer, D., Ziereis, H., and Borrmann, S.,
2021 Aircraft-based observations of IEPOX-derived isoprene SOA formation in the tropical
2022 upper troposphere in the Amazon region: Atmos. Chem. Phys. Discuss., 2017, in
2023 preparation.

2024 Schwarz, J. P., Gao, R. S., Fahey, D. W., Thomson, D. S., Watts, L. A., Wilson, J. C., Reeves, J.
2025 M., Darbeheshti, M., Baumgardner, D. G., Kok, G. L., Chung, S. H., Schulz, M.,
2026 Hendricks, J., Lauer, A., Karcher, B., Slowik, J. G., Rosenlof, K. H., Thompson, T. L.,
2027 Langford, A. O., Loewenstein, M., and Aikin, K. C., Single-particle measurements of
2028 midlatitude black carbon and light-scattering aerosols from the boundary layer to the
2029 lower stratosphere: J. Geophys. Res., 111, D16207, doi:10.1029/2006JD007076, 2006.

2030 Schwarz, J. P., Weinzierl, B., Samset, B. H., Dollner, M., Heimerl, K., Markovic, M. Z., Perring,
2031 A. E., and Ziemba, L., Aircraft measurements of black carbon vertical profiles show
2032 upper tropospheric variability and stability: Geophys. Res. Lett., 44, 1132-1140,
2033 doi:10.1002/2016GL071241, 2017.

2034 Seibert, P., and Frank, A., Source-receptor matrix calculation with a Lagrangian particle
2035 dispersion model in backward mode: Atmos. Chem. Phys., 4, 51-63, 2004.

2036 Sherwood, S., A microphysical connection among biomass burning, cumulus clouds, and
2037 stratospheric moisture: Science, 295, 1272-1275, 2002.

2038 Spracklen, D. V., Carslaw, K. S., Kulmala, M., Kerminen, V.-M., Mann, G. W., and Sihto, S.-L.,
2039 The contribution of boundary layer nucleation events to total particle concentrations on
2040 regional and global scales: *Atmos. Chem. Phys.*, 6, 5631-5648, 2006.

2041 Stein, A. F., Draxler, R. R., Rolph, G. D., Stunder, B. J. B., Cohen, M. D., and Ngan, F.,
2042 NOAA's HYSPLIT atmospheric transport and dispersion modeling system: *Bull. Am.*
2043 *Meteorol. Soc.*, 96, 2059-2077, doi:10.1175/BAMS-D-14-00110.1, 2015.

2044 Stephens, M., Turner, N., and Sandberg, J., Particle identification by laser-induced
2045 incandescence in a solid-state laser cavity: *Applied Optics*, 42, 3726-3736,
2046 doi:10.1364/ao.42.003726, 2003.

2047 Stohl, A., Hittenberger, M., and Wotawa, G., Validation of the Lagrangian particle dispersion
2048 model FLEXPART against large-scale tracer experiment data: *Atmospheric*
2049 *Environment*, 32, 4245-4264, doi:10.1016/s1352-2310(98)00184-8, 1998.

2050 Stohl, A., and Thomson, D. J., A density correction for Lagrangian particle dispersion models:
2051 *Boundary-Layer Meteorology*, 90, 155-167, doi:10.1023/a:1001741110696, 1999.

2052 Stohl, A., Eckhardt, S., Forster, C., James, P., Spichtinger, N., and Seibert, P., A replacement for
2053 simple back trajectory calculations in the interpretation of atmospheric trace substance
2054 measurements: *Atmospheric Environment*, 36, 4635-4648, doi:10.1016/s1352-
2055 2310(02)00416-8, 2002.

2056 Stohl, A., Forster, C., Frank, A., Seibert, P., and Wotawa, G., Technical note: The Lagrangian
2057 particle dispersion model FLEXPART version 6.2: *Atmos. Chem. Phys.*, 5, 2461-2474,
2058 2005.

2059 Stolz, D. C., Rutledge, S. A., and Pierce, J. R., Simultaneous influences of thermodynamics and
2060 aerosols on deep convection and lightning in the tropics: *J. Geophys. Res.*, 120, 6207-
2061 6231, doi:10.1002/2014jd023033, 2015.

2062 Talbot, R. W., Andreae, M. O., Andreae, T. W., and Harriss, R. C., Regional aerosol chemistry
2063 of the Amazon Basin during the dry season: *J. Geophys. Res.*, 93, 1499-1508, 1988.

2064 Talbot, R. W., Andreae, M. O., Berresheim, H., Artaxo, P., Garstang, M., Harriss, R. C.,
2065 Beecher, K. M., and Li, S. M., Aerosol chemistry during the wet season in Central
2066 Amazonia: The influence of long-range transport: *J. Geophys. Res.*, 95, 16,955-16,969,
2067 1990.

2068 Thalman, R., Thalman, R., de Sá, S. S., Palm, B. B., Barbosa, H. M. J., Pöhlker, M. L.,
2069 Alexander, M. L., Brito, J., Carbone, S., Castillo, P., Day, D. A., Kuang, C., Manzi, A.,
2070 Ng, N. L., Sedlacek III, A. J., Souza, R., Springston, S., Watson, T., Pöhlker, C., Pöschl,
2071 U., Andreae, M. O., Artaxo, P., Jimenez, J. L., Martin, S. T., and Wang, J., CCN activity
2072 and organic hygroscopicity of aerosols downwind of an urban region in central
2073 Amazonia: Seasonal and diel variations and impact of anthropogenic emissions: *Atmos.*
2074 *Chem. Phys. Discuss.*, doi:10.5194/acp-2017-251, 2017.

2075 Thornberry, T., Froyd, K. D., Murphy, D. M., Thomson, D. S., Anderson, B. E., Thornhill, K. L.,
2076 and Winstead, E. L., Persistence of organic carbon in heated aerosol residuals measured
2077 during Tropical Composition Cloud and Climate Coupling (TC4): *J. Geophys. Res.*, 115,
2078 D00J02, doi:10.1029/2009jd012721, 2010.

- 2079 Tröstl, J., Chuang, W. K., Gordon, H., Heinritzi, M., Yan, C., Molteni, U., Ahlm, L., Frege, C.,
 2080 Bianchi, F., Wagner, R., Simon, M., Lehtipalo, K., Williamson, C., Craven, J. S.,
 2081 Duplissy, J., Adamov, A., Almeida, J., Bernhammer, A.-K., Breitenlechner, M., Brilke,
 2082 S., Dias, A., Ehrhart, S., Flagan, R. C., Franchin, A., Fuchs, C., Guida, R., Gysel, M.,
 2083 Hansel, A., Hoyle, C. R., Jokinen, T., Junninen, H., Kangasluoma, J., Keskinen, H., Kim,
 2084 J., Krapf, M., Kürten, A., Laaksonen, A., Lawler, M., Leiminger, M., Mathot, S., Möhler,
 2085 O., Nieminen, T., Onnela, A., Petäjä, T., Piel, F. M., Miettinen, P., Rissanen, M. P.,
 2086 Rondo, L., Sarnela, N., Schobesberger, S., Sengupta, K., Sipilä, M., Smith, J. N., Steiner,
 2087 G., Tomè, A., Virtanen, A., Wagner, A. C., Weingartner, E., Wimmer, D., Winkler, P.
 2088 M., Ye, P., Carslaw, K. S., Curtius, J., Dommen, J., Kirkby, J., Kulmala, M., Riipinen, I.,
 2089 Worsnop, D. R., Donahue, N. M., and Baltensperger, U., The role of low-volatility
 2090 organic compounds in initial particle growth in the atmosphere: *Nature*, 533, 527-531,
 2091 doi:10.1038/nature18271, 2016.
- 2092 Twohy, C. H., Clement, C. F., Gandrud, B. W., Weinheimer, A. J., Campos, T. L., Baumgardner,
 2093 D., Brune, W. H., Faloon, I., Sachse, G. W., Vay, S. A., and Tan, D., Deep convection
 2094 as a source of new particles in the midlatitude upper troposphere: *J. Geophys. Res.*, 107,
 2095 4560, doi:10.1029/2001JD000323, 2002.
- 2096 Vestin, A., Rissler, J., Swietlicki, E., Frank, G., and Andreae, M. O., Cloud nucleating properties
 2097 of the Amazonian biomass burning aerosol: Cloud condensation nuclei measurements
 2098 and modeling: *J. Geophys. Res.*, 112, D14201, doi:10.1029/2006JD008104, 2007.
- 2099 Virji, H., A preliminary study of summertime tropospheric circulation patterns over South
 2100 America estimated from cloud winds: *Mon. Weather Rev.*, 109, 599-610, 1981.
- 2101 Voigt, C., Schumann, U., Minikin, A., Abdelmonem, A., Afchine, A., Borrmann, S., Boettcher,
 2102 M., Bucuchholz, B., Bugliaro, L., Costa, A., Curtius, J., Dollner, M., Doernbrack, A.,
 2103 Dreiling, V., Ebert, V., Ehrlich, A., Fix, A., Forster, L., Frank, F., Fuetterer, D., Giez, A.,
 2104 Graf, K., Grooss, J.-U., Gross, S., Heimerl, K., Heinold, B., Hueneke, T., Jaervinen, E.,
 2105 Jurkat, T., Kaufmann, S., Kenntner, M., Klingebiel, M., Klimach, T., Kohl, R., Kraemer,
 2106 M., Krisna, T. C., Luebke, A., Mayer, B., Mertes, S., Molleker, S., Petzold, A.,
 2107 Pfeilsticker, K., Port, M., Rapp, M., Reutter, P., Rolf, C., Rose, D., Sauer, D., Schaefer,
 2108 A., Schlage, R., Schnaiter, M., Schneider, J., Spelten, N., Spichtinger, P., Stock, P.,
 2109 Walser, A., Weigel, R., Weinzierl, B., Wendisch, M., Werner, F., Wernli, H., Wirth, M.,
 2110 Zahn, A., Ziereis, H., and Zoger, M., ML-CIRRUS: The airborne experiment on natural
 2111 cirrus and contrail cirrus with the high-altitude long-range research aircraft HALO: *Bull.*
 2112 *Am. Meteorol. Soc.*, 98, 271-288, doi:10.1175/bams-d-15-00213.1, 2017.
- 2113 von der Weiden, S. L., Drewnick, F., and Borrmann, S., Particle Loss Calculator – a new
 2114 software tool for the assessment of the performance of aerosol inlet systems: *Atmos.*
 2115 *Meas. Tech.*, 2, 479-494, doi:10.5194/amt-2-479-2009, 2009.
- 2116 Waddicor, D. A., Vaughan, G., Choularton, T. W., Bower, K. N., Coe, H., Gallagher, M.,
 2117 Williams, P. I., Flynn, M., Volz-Thomas, A., Pätz, H. W., Isaac, P., Hacker, J., Arnold,
 2118 F., Schlager, H., and Whiteway, J. A., Aerosol observations and growth rates downwind
 2119 of the anvil of a deep tropical thunderstorm: *Atmos. Chem. Phys.*, 12, 6157-6172,
 2120 doi:10.5194/acp-12-6157-2012, 2012.

- 2121 Walser, A., Sauer, D., Spanu, A., Gasteiger, J., and Weinzierl, B., On the parametrization of
2122 optical particle counter response including instrument-induced broadening of size spectra
2123 and a self-consistent evaluation of calibration measurements: *Atmos. Meas. Tech.*
2124 *Discuss.*, 2017, 1-30, doi:10.5194/amt-2017-81, 2017.
- 2125 Wang, H., and Fu, R., The influence of Amazon rainfall on the Atlantic ITCZ through
2126 convectively coupled Kelvin waves: *J. Clim.*, 20, 1188-1201, doi:10.1175/jcli4061.1,
2127 2007.
- 2128 Wang, J., Krejci, R., Giangrande, S., Kuang, C., Barbosa, H. M. J., Brito, J., Carbone, S., Chi,
2129 X., Comstock, J., Ditas, F., Lavric, J., Manninen, H. E., Mei, F., Moran-Zuloaga, D.,
2130 Pöhlker, C., Pöhlker, M. L., Saturno, J., Schmid, B., Souza, R. A. F., Springston, S. R.,
2131 Tomlinson, J. M., Toto, T., Walter, D., Wimmer, D., Smith, J. N., Kulmala, M.,
2132 Machado, L. A. T., Artaxo, P., Andreae, M. O., Petäjä, T., and Martin, S. T., Amazon
2133 boundary layer aerosol concentration sustained by vertical transport during rainfall:
2134 *Nature*, 539, 416-419, doi:10.1038/nature19819, 2016a.
- 2135 Wang, Q., Saturno, J., Chi, X., Walter, D., Lavric, J. V., Moran-Zuloaga, D., Ditas, F., Pöhlker,
2136 C., Brito, J., Carbone, S., Artaxo, P., and Andreae, M. O., Modeling investigation of
2137 light-absorbing aerosols in the Amazon Basin during the wet season: *Atmos. Chem.*
2138 *Phys.*, 16, 14,775-14,794, doi:10.5194/acp-16-14775-2016, 2016b.
- 2139 Watson, C. E., Fishman, J., and Reichle, H. G., The significance of biomass burning as a source
2140 of carbon monoxide and ozone in the Southern Hemisphere tropics: A satellite analysis:
2141 *J. Geophys. Res.*, 95, 14,443-14,450, 1990.
- 2142 Weigel, R., Borrmann, S., Kazil, J., Minikin, A., Stohl, A., Wilson, J. C., Reeves, J. M., Kunkel,
2143 D., de Reus, M., Frey, W., Lovejoy, E. R., Volk, C. M., Viciani, S., D'Amato, F.,
2144 Schiller, C., Peter, T., Schlager, H., Cairo, F., Law, K. S., Shur, G. N., Belyaev, G. V.,
2145 and Curtius, J., In situ observations of new particle formation in the tropical upper
2146 troposphere: the role of clouds and the nucleation mechanism: *Atmos. Chem. Phys.*, 11,
2147 9983-10,010, doi:10.5194/acp-11-9983-2011, 2011.
- 2148 Weigel, R., Spichtinger, P., Mahnke, C., Klingebiel, M., Afchine, A., Petzold, A., Krämer, M.,
2149 Costa, A., Molleker, S., Reutter, P., Szakáll, M., Port, M., Grulich, L., Jurkat, T.,
2150 Minikin, A., and Borrmann, S., Thermodynamic correction of particle concentrations
2151 measured by underwing probes on fast-flying aircraft: *Atmos. Meas. Tech.*, 9, 5135-
2152 5162, doi:10.5194/amt-9-5135-2016, 2016.
- 2153 Weigelt, A., Hermann, M., van Velthoven, P. F. J., Brenninkmeijer, C. A. M., Schlaf, G., Zahn,
2154 A., and Wiedensohler, A., Influence of clouds on aerosol particle number concentrations
2155 in the upper troposphere: *J. Geophys. Res.*, 114, D01204, doi:10.1029/2008jd009805,
2156 2009.
- 2157 Weinzierl, B., Ansmann, A., Prospero, J. M., Althausen, D., Benker, N., Chouza, F., Dollner, M.,
2158 Farrell, D., Fomba, W. K., Freudenthaler, V., Gasteiger, J., Gross, S., Haarig, M.,
2159 Heinold, B., Kandler, K., Kristensen, T. B., Mayol-Bracero, O. L., Müller, T., Reitebuch,
2160 O., Sauer, D., Schafner, A., Schepanski, K., Spanu, A., Tegen, I., Toledano, C., and
2161 Walser, A., The Saharan Aerosol Long-Range Transport and Aerosol-Cloud-Interaction
2162 Experiment: Overview and Selected Highlights: *Bull. Am. Meteorol. Soc.*, 98, 1427-
2163 1451, doi:10.1175/bams-d-15-00142.1, 2017.

2164 Wendisch, M., Pöschl, U., Andreae, M. O., Machado, L. A. T., Albrecht, R., Schlager, H.,
 2165 Rosenfeld, D., Martin, S. T., Abdelmonem, A., Afchine, A., Araújo, A. C., Artaxo, P.,
 2166 Aufmhoff, H., Barbosa, H. M. J., Borrmann, S., Braga, R., Buchholz, B., Cecchini, M.
 2167 A., Costa, A., Curtius, J., Dollner, M., Dorf, M., Dreiling, V., Ebert, V., Ehrlich, A.,
 2168 Ewald, F., Fisch, G., Fix, A., Frank, F., Fütterer, D., Heckl, C., Heidelberg, F., Hüneke,
 2169 T., Jäkel, E., Järvinen, E., Jurkat, T., Kanter, S., Kästner, U., Kenntner, M., Kesselmeier,
 2170 J., Klimach, T., Knecht, M., Kohl, R., Kölling, T., Krämer, M., Krüger, M., Krisna, T. C.,
 2171 Lavric, J. V., Longo, K., Mahnke, C., Manzi, A. O., Mayer, B., Mertes, S., Minikin, A.,
 2172 Molleker, S., Münch, S., Nillius, B., Pfeilsticker, K., Pöhlker, C., Roiger, A., Rose, D.,
 2173 Rosenow, D., Sauer, D., Schnaiter, M., Schneider, J., Schulz, C., Souza, R. A. F. d.,
 2174 Spanu, A., Stock, P., Vila, D., Voigt, C., Walser, A., Walter, D., Weigel, R., Weinzierl,
 2175 B., Werner, F., Yamasoe, M. A., Ziereis, H., Zinner, T., and Zöger, M., ACRIDICON–
 2176 CHUVA campaign: Studying tropical deep convective clouds and precipitation over
 2177 Amazonia using the new German research aircraft HALO: *Bull. Am. Meteorol. Soc.*, 97,
 2178 1885-1908, doi:10.1175/bams-d-14-00255.1, 2016.

2179 Wiedensohler, A., An approximation of the bipolar charge distribution for particles in the sub-
 2180 micron size range: *J. Aerosol Sci.*, 19, 387-389, 1988.

2181 Wiedensohler, A., Ma, N., Birmili, W., Heintzenberg, J., Ditas, F., Andreae, M. O., and Panov,
 2182 A., Rare particle nucleation over remote forests: *Nature*, 2017, submitted.

2183 Williams, J., de Reus, M., Krejci, R., Fischer, H., and Strom, J., Application of the variability-
 2184 size relationship to atmospheric aerosol studies: estimating aerosol lifetimes and ages:
 2185 *Atmos. Chem. Phys.*, 2, 133-145, 2002.

2186 Witte, K., HALO Technical Note: Top Fuselage Aperture Plates - Particle Enrichment. DLR
 2187 Flight Facility Oberpfaffenhofen, Weßling, Germany, 17 p. (2008).

2188 Yang, Q., Easter, R. C., Campuzano-Jost, P., Jimenez, J. L., Fast, J. D., Ghan, S. J., Wang, H.,
 2189 Berg, L. K., Barth, M. C., Liu, Y., Shrivastava, M. B., Singh, B., Morrison, H., Fan, J.,
 2190 Ziegler, C. L., Bela, M., Apel, E., Diskin, G. S., Mikoviny, T., and Wisthaler, A., Aerosol
 2191 transport and wet scavenging in deep convective clouds: A case study and model
 2192 evaluation using a multiple passive tracer analysis approach: *J. Geophys. Res.*, 120,
 2193 8448-8468, doi:10.1002/2015JD023647, 2015.

2194 Yin, Y., Carslaw, K. S., and Feingold, G., Vertical transport and processing of aerosols in a
 2195 mixed-phase convective cloud and the feedback on cloud development: *Q. J. R.*
 2196 *Meteorol. Soc.*, 131, 221-245, 2005.

2197 Young, L. H., Benson, D. R., Montanaro, W. M., Lee, S. H., Pan, L. L., Rogers, D. C., Jensen, J.,
 2198 Stith, J. L., Davis, C. A., Campos, T. L., Bowman, K. P., Cooper, W. A., and Lait, L. R.,
 2199 Enhanced new particle formation observed in the northern midlatitude tropopause region:
 2200 *J. Geophys. Res.*, 112, D10218, doi:10.1029/2006jd008109, 2007.

2201 Yu, F., Wang, Z., Luo, G., and Turco, R., Ion-mediated nucleation as an important global source
 2202 of tropospheric aerosols: *Atmos. Chem. Phys.*, 8, 2537-2554, 2008.

2203 Yu, F., Luo, G., Nadykto, A. B., and Herb, J., Impact of temperature dependence on the possible
 2204 contribution of organics to new particle formation in the atmosphere: *Atmos. Chem.*
 2205 *Phys.*, 17, 4997-5005, doi:10.5194/acp-17-4997-2017, 2017.

2206 Yu, P. F., Murphy, D. M., Portmann, R. W., Toon, O. B., Froyd, K. D., Rollins, A. W., Gao, R.
 2207 S., and Rosenlof, K. H., Radiative forcing from anthropogenic sulfur and organic
 2208 emissions reaching the stratosphere: *Geophys. Res. Lett.*, 43, 9361-9367,
 2209 doi:10.1002/2016gl070153, 2016.

2210 Zhou, J., Swietlicki, E., Hansson, H.-C., and Artaxo, P., Submicrometer aerosol particle size
 2211 distribution and hygroscopic growth measured in the Amazon rain forest during the wet
 2212 season: *J. Geophys. Res.*, 107, 8055, doi:10.129/2000JD000203, 2002.

2213 Zhou, J. C., Swietlicki, E., Berg, O. H., Aalto, P. P., Hameri, K., Nilsson, E. D., and Leck, C.,
 2214 Hygroscopic properties of aerosol particles over the central Arctic Ocean during summer:
 2215 *J. Geophys. Res.*, 106, 32111-32123, 2001.

2216 Zhou, J. Y., and Lau, K. M., Does a monsoon climate exist over South America?: *J. Clim.*, 11,
 2217 1020-1040, 1998.

2218 Zhuang, Y., Fu, R., Marengo, J. A., and Wang, H., Seasonal variation of shallow-to-deep
 2219 convection transition and its link to the environmental conditions over the Central
 2220 Amazon: *J. Geophys. Res.*, 122, 2649-2666, doi:10.1002/2016JD025993, 2017.

2221 Ziereis, H., Schlager, H., Schulte, P., van Velthoven, P. F. J., and Slemr, F., Distributions of NO,
 2222 NO_x, and NO_y in the upper troposphere and lower stratosphere between 28° and 61°N
 2223 during POLINAT 2: *J. Geophys. Res.*, 105, 3653-3664, doi:10.1029/1999jd900870,
 2224 2000.

2225 Zipser, E. J., Mesoscale and convective-scale downdrafts as distinct components of squall-line
 2226 structure: *Mon. Weather Rev.*, 105, 1568-1589, doi:10.1175/1520-
 2227 0493(1977)105<1568:macdad>2.0.co;2, 1977.
 2228

Table 1: Properties of the flight legs on which elevated aerosol concentrations were measured during ACRIDICON-CHUVA.

Flight	Leg	Start UTC	End UTC	Altitude range m	N _{CN} max. cm ⁻³	N _{CN} mean cm ⁻³	N _{CCN0.5} mean cm ⁻³	N _{acc} mean cm ⁻³	Ultrafine fraction	Trajectory type	Min T _b [min,max] ^a °C	Time since last DC [min,max] ^b hours	Time in DC [min,max] ^c hours	Sampling environment
AC07	A1	1622	1626	8300-9200	17200	9360	657	696	0.93	A	[-76,-65]	[0, 0]	[21,27]	in and near outflows
AC07	AA1	1626	1627	9140	36100	19230	775	588	0.97	A	---	---		in and near outflows
AC07	A2	1627	1633	8100-9100	38400	24250	471	499	0.98	A	[-77,-76]	[0, 0]	[19,26]	clear air
AC07	AA2	1633	1637	6700-8200	26700	6450	708	565	0.91	A	---	---		clear air
AC07	B	1714	1717	7000-8400	15900	7140	214	270	0.96	A	[-75,-68]	[0, 0]	[13,28]	clear air
AC07	C	1923	1929	9000	22600	16480	272	389	0.98	A	[-78,-74]	[0, 0]	[27,40]	clear air
AC07	D1	2024	2027	8500-10500	23200	14270	---	146	0.99	A	[-74,-68]	[0, 0]	[29,40]	clear air near outflow
AC07	D2	2028	2112	11000	28200	15160	---	76	0.99	A	[-76,-68]	[0, 0]	[12,28]	outflow, mixed with cirrus
AC07	E	2126	2129	13100	33500	15140	---	---	---	A	[-72,-67]	[0, 0]	[21,28]	pristine ice cirrus
AC07	F	2130	2147	13200	25300	12030	13	---	---	A	[-72,-69]	[0, 5]	[24,32]	clear air
AC07	G	2205	2211	13000-10000	20500	15470	284	---	---	A	[-76,-51]	[0, 0]	[24,31]	cirrus
AC07	GG	2210	2212	10200-9500	19500	16840	-	869	0.95	A				cirrus
AC08	No useful high alt CN data. CCN moderately elevated at ca. 10 and 13 km, ca. 1200 /cc													
AC09	A1	1453	1455	11400	24100	10370	901	572	0.94	B	[-74,-71]	[16,16]	[22,41]	clear air
AC09	A2	1455	1458	11900	27600	12970	1103	808	0.94	B	[-76,-72]	[16,17]	[34,41]	clear air
AC09	A3	1501	1503	11000	35100	14470	629	697	0.95	B	[-72,-70]	[17,17]	[38,40]	clear air
AC09	B1	1815	1820	11000	19100	10540	1393	954	0.91	B	[-76,-74]	[14,14]	[49,54]	around Cb anvil
AC09	B2	1821	1827	11300-11600	28300	15370	1414	1012	0.93	B	[-78,-73]	[14,14]	[47,57]	around Cb anvil
AC09	C	1830	1838	11600	31700	9130	1490	1127	0.88	B	[-79,-76]	[1,19]	[45,56]	clear air
AC09	D	1838	1923	11300-11900	13000	5690	1012	869	0.85	B, C	[-80,-74]	[1, 1]	[34,57]	outflow region
AC09	E	1929	1957	11300	24200	12790	891	856	0.93	B, C	[-76,-70]	[2,21]	[24,48]	outflow region
AC10	A	1709	1714	6700-8600	27400	13040	355	389	0.94	C	[-66,-54]	[6, 7]	[9,32]	clear air
AC10	B	1721	1728	9200	32500	12480	850	861	0.91	D	[-78,-72]	[4,10]	[34,56]	clear air
AC10	C	1800	1808	9200	26000	13100	1020	937	0.91	B	[-79,-71]	[7,10]	[33,56]	clear air
AC10	D	1811	1815	9200-10100	33000	20180	1130	684	0.95	B	[-77,-71]	[5, 5]	[23,51]	clear air
AC10	E	1817	1833	10800-13600	33400	22210	712	289	0.98	E	[-84,-72]	[0,12]	[42,76]	thin cirrus
AC10	F	1835	1906	13800	34700	16540	464	---	---	E	[-80,-68]	[0, 0]	[33,54]	cirrus layer
AC10	G	1912	1919	10600-7500	24200	10220	1230	1160	0.83	B	[-80,-58]	[0,14]	[11,60]	clear air

AC11	A	1603	1605	8700-9700	47400	26280	572	323	0.98	E	[-54,-32]	[3,44]	[1,18]	clear air
AC11	B	1613	1630	11800	4700	3850	1390	763	0.80	E, D	[-76,-58]	[0, 6]	[14,41]	clear air
AC11	C	1633	1642	11800-10800	31700	6080	1436	937	0.78	D	[-80,-77]	[0, 0]	[30,46]	around anvil
AC11	D	1831	1850	5200-6700	25000	14380	---	187	0.98	C	[-79,-79]	[0, 0]	[18,19]	outflow region
AC11	E	1907	1930	9900-12200	36100	29280	---	330	0.99	D	[-85,-74]	[0, 0]	[26,82]	outflow region
AC11	F1	1940	1942	12200	54900	22060	---	674	0.95	E, D	[-84,-84]	[0, 0]	[55,55]	outflow region
AC11	F2	1942	1951	12200	32800	20720	---	549	0.97	E, D	[-84,-84]	[0, 0]	[55,55]	outflow region
AC11	G	2005	2030	13700-14200	2830	10090	---	---	---	D	[-84,-84]	[0, 0]	[55,55]	outflow region
AC11	H	2042	2057	12200-10400	47900	20240	---	663	0.96	A	[-84,-84]	[0, 0]	[55,55]	outflow region
AC12	A	1512	1518	9800-11300	19300	8040	1130	341	0.95	E	[-79,-74]	[0, 0]	[23,37]	clear
AC12	B	1524	1527	11300	24700	9290	1120	358	0.95	A	[-83,-71]	[0, 0]	[26,66]	thin outflow
AC12	C	1537	1541	7300-5600	26200	7760	356	186	0.95	B	[-78,-57]	[1, 1]	[7,16]	clear
AC12	D	1922	1925	8000-9700	17400	11980	650	132	0.99	B	[-71,-71]	[17,20]	[6,12]	clear
AC12	E	1928	1933	10800-12200	25300	15740	423	75	0.99	B	[-70,-57]	[20,24]	[8,18]	clear
AC12	F1	1936	1950	12200-13100	7020	5940	2010	698	0.88	D	[-80,-67]	[0,38]	[12,40]	clear
AC12	F2	1952	2015	13100	7300	5950	1190	594	0.90	B, D	[-82,-74]	[0,21]	[28,77]	aged outflow
AC12	G	2017	2020	13200-12800	19600	10930	661	422	0.96	E	[-79,-75]	[0, 0]	[26,49]	outflow
AC12	H	2023	2027	11300-9600	23900	16930	849	372	0.98	C	[-80,-77]	[0, 0]	[37,59]	mostly clear air
AC13	A	1520	1533	11000-11900	43500	13830	1054	---	---	C	[-78,-75]	[0,12]	[27,43]	mostly cirrus and old outflow
AC13	B	1550	1607	11900-6900	36300	11890	1012	476	0.95	A	[-83,-50]	[1, 8]	[11,47]	mostly cirrus and old outflow
AC13	C	1901	1908	9500	25700	17870	687	---	---	A	[-72,-66]	[0, 0]	[13,24]	clear air around anvils
AC13	D1	1909	1912	10700	26200	18600	910	---	---	A	[-70,-66]	[0, 0]	[15,19]	""
AC13	D2	1916	1919	10700	28200	19170	1017	---	---	A	[-73,-69]	[0, 0]	[24,25]	""
AC13	D3	1921	1926	10700	29500	19010	919	---	---	A	[-69,-68]	[0, 0]	[15,26]	""
AC13	D4	1930	1933	10700	21600	10890	727	---	---	A	[-68,-67]	[0, 0]	[14,17]	""
AC13	E	1939	1942	11900	22500	15100	770	---	---	A	[-57,-47]	[10,10]	[5, 8]	""
AC13	F	2036	2043	12200	18600	7840	912	---	---	A	[-78,-76]	[0, 0]	[34,43]	clear air, some cirrus
AC14	no useable high alt data													
AC15	A	1415	1419	10500-11700	58500	38170	687	453	0.98	D	[-81,-78]	[0, 9]	[63,68]	air around a huge Cb anvil
AC15	B	1419	1424	11800-12900	67900	46970	701	405	0.98	D	[-81,-81]	[0, 0]	[59,66]	mostly cirrus and old outflow
AC15	C	1431	1432	13200	49500	20900	1070	747	0.94	D	[-84,-84]	[0, 0]	[55,55]	""
AC15	D	1436	1437	13200	38300	15300	1009	633	0.92	D	[-84,-77]	[0, 0]	[50,56]	""

AC15	E	1448	1449	12500	44500	29220	603	718	0.97	D	[-81,-79]	[0, 0]	[54,59]	""
AC15	F	1452	1455	12500	60500	45100	672	514	0.97	D	[-79,-75]	[0, 0]	[52,56]	""
AC15	G	1456	1500	12500-11900	59200	38070	748	574	0.98	D	[-82,-72]	[0, 0]	[53,62]	""
AC15	H	1502	1505	11900-11600	49800	16440	1114	750	0.94	D	[-76,-73]	[0, 0]	[62,69]	""
AC15	I	1518	1519	11300	46800	22000	1848	931	0.93	D	[-79,-73]	[0, 0]	[65,71]	""
AC15	J	1526	1528	10700	21700	8980	1292	817	0.86	D	[-76,-75]	[0, 0]	[59,65]	""
AC16	A	1554	1600	10700-12200	40300	21210	606	223	0.98	B	[-75,-68]	[0, 0]	[9,18]	clear air
AC16	B	1749	1757	10000-10300	28200	11350	926	282	0.97	B	[-68,-57]	[0, 0]	[8,10]	air around a large Cb anvil
AC16	C	1803	1815	10300-10700	27200	15180	746	208	0.98	B	[-75,-60]	[0, 0]	[9,12]	air around a large Cb anvil
AC16	D	1818	1820	10700-11300	23100	11540	789	356	0.97	B	[-75,-67]	[0, 0]	[10,17]	air around a large Cb anvil
AC16	E	1824	1826	12000	26700	14070	488	354	0.97	B	[-75,-75]	[0, 0]	[17,19]	air around a large Cb anvil
AC16	F	1857	1911	12600-11900	19500	11210	598	521	0.94	B	[-73,-66]	[0, 0]	[22,28]	air around a large Cb anvil
AC16	G	1925	1935	11900	22700	12880	703	492	0.95	B	[-73,-70]	[0, 0]	[22,30]	air around a large Cb anvil
AC16	H	1950	2000	11900-9600	27100	12670	806	444	0.96	B	[-75,-65]	[0, 0]	[13,29]	air around a large Cb anvil
AC17	no high alt data													
AC18	A1	1454	1456	8300-8600	20700	10698	-	219	0.98	B	[-60,-10]	[14,17]	[2, 5]	clear air
AC18	A2	1520	1522	12900-8400	22500	14538	479	400	0.97	C	[-58,-38]	[14,18]	[1, 5]	clear air
AC18	B	1753	1801	7100	10040	6255	400	312	0.95	C	[-30,-0]	[0, 0]	[1, 2]	clear air around anvils
AC18	C	1833	1834	7100-7400	14200	10713	404	280	0.97	C	[-52,-28]	[22,22]	[1, 1]	clear air around anvils
AC18	D	1913	2005	11300-12000	4000	2367	916	640	0.73	A, D	[-75,-37]	[0,16]	[3,46]	clear air around anvils
AC18	E1	2017	2034	13000-13700	8170	4841	1481	892	0.82	A, D	[-84,-68]	[0,44]	[21,45]	clear air
AC18	E2	2040	2043	13700-13200	44700	13679	469	283	0.98	D	[-77,-71]	[0, 0]	[28,42]	clear air downwind of large Cb
AC18	F	2053	2057	9500-8100	15800	8778	444	318	0.96	C, D	[-68,-32]	[1,20]	[1,11]	clear air
AC19	A1	1518	1519	7300-7700	30600	28480	451	339	0.99	B	[-82,-65]	[14,43]	[7,14]	clear air
AC19	A2	1536	1601	12600	3600	2910	679	268	0.91	E	[-72,-58]	[43,94]	[6,19]	clear air, high alt leg
AC19	E1	2009	2010	8500-8900	14700	11470	642	271	0.98	B	[-75,-59]	[16,92]	[8,16]	clear air
AC19	E2	2023	2100	13800	3900	2690	1024	498	0.81	A	[-76,-29]	[0,105]	[1,22]	clear air
AC19	E3	2106	2119	13800	10200	2770	1073	950	0.65	B	[-73,-57]	[0, 1]	[6,25]	outflow
AC19	E4	2127	2128	7500-6600	66000	16210	440	414	0.96	D	[-60,-59]	[3,22]	[4, 7]	clear air
AC20	A	1654	1658	11700-12500	30300	21540	881	616	0.97	A, D	[-77,-53]	[1, 1]	[7,28]	NPF at top of smoke layer
AC20	B	1901	1905	12300	21300	9340	614	381	0.95	A, D	[-78,-70]	[0, 0]	[14,42]	NPF at top of smoke layer

-
- ^a) Minimum and maximum temperature at top of most recent deep convection in grid boxes through which the trajectories for the flight leg had passed.
 - ^b) Trajectories were calculated for each minute of the leg, and for each trajectory the time between sampling and the most recent encounter with DC was determined. Given are the shortest and the longest of these time intervals.
 - ^c) Minimum and maximum length of time that the trajectories from each leg had spent in grid boxes with DC.

Table 2: Composition of UT aerosols based on AMS and SP2 measurements (means and standard deviations).

Flight	Time	N _{CN}	N _{CCN0.5}	N _{acc}	OA	NO ₃	SO ₄	NH ₄	rBC	OA/SO ₄	NO ₃ /SO ₄	Ultrafine fraction	CO
	UT	cm ⁻³	cm ⁻³	cm ⁻³	µg m ⁻³	µg m ⁻³	µg m ⁻³	µg m ⁻³	µg m ⁻³				ppb
AC07													
<4 km	-	1620±680	1070±410	1363±651	1.81±0.96	0.088±0.039	0.30±0.10	0.20±0.17	0.40±0.21	6.1±4.4	0.30±0.22	0.19±0.16	-
>7 km	-	9300±7420	300±210	278±232	0.61±0.50	0.072±0.051	0.071±0.060	<0.05	0.003±0.007	8.5±10.2	1.0±1.1	0.92±0.008	-
AA1	16:24-16:29	19200	650	588	1.55±0.27	0.14±0.03	<0.005	-	0.002	>300	>28	0.97	-
AA2	16:33-16:37	6450	710	565	1.26±0.22	0.12±0.02	0.020±0.021	-	0.002	63	6.0	0.89	-
GG	22:09-22:11	16800	-	921	2.40±1.09	0.20±0.08	<0.005	-	0.002	>480	>40	-	-
AC09													
<5 km	-	920±490	290±95	395±189	0.28±0.22	0.013±0.020	0.15±0.07	0.03±0.07	0.085±0.095	1.8±1.7	0.08±0.14	0.51±0.26	-
>9 km	-	8020±5180	1090±430	861±338	1.80±0.52	0.22±0.08	0.14±0.06	<0.05	0.001±0.003	13.3±6.7	1.6±0.9	0.86±0.07	-
AA	14:48-15:08	2280	1050	754	1.55±0.53	0.21±0.09	0.083±0.044	<0.05	0.001	18.6	2.5	0.54	-
BB	18:18-19:23	8060	1200	922	1.88±0.47	0.23±0.07	0.15±0.04	<0.05	0.001	12.6	1.5	0.85	-
EE	19:28-19:58	12000	950	892	1.96±0.47	0.23±0.07	0.13±0.03	<0.05	0.001	15.4	1.8	0.92	-
A1+A2	14:53-14:58	12100	1040	724	1.69±0.38	0.23±0.06	0.08±0.04	<0.05	<0.001	21.8	3.1	0.91	-
AC18													
<5 km	-	740±220	350±100	473±212	1.11±1.17	0.060±0.056	0.55±0.27	0.19±0.10	0.15±0.15	2.8±1.4	0.11±0.08	0.51±0.26	-
>10 km	-	2950±2640	920±310	560±145	2.07±0.63	0.24±0.10	0.23±0.06	<0.05	0.002±0.005	9.1±3.9	1.1±0.5	0.86±0.07	-
AA	15:06-15:16	(1740)	870	545	1.64±0.20	0.20±0.02	0.19±0.05	<0.05	0.001	8.5	1.0	1.50	-
DD	19:21-20:05	2360	910	639	2.04±0.23	0.22±0.04	0.22±0.06	<0.05	0.002	9.3	1.0	0.61	-
A1	14:54-14:56	87000	-	203	0.43±0.17	0.06±0.03	0.18±0.08	<0.05	0.002	2.4	0.31	-	-
A2	15:20-15:22	17400	500	433	0.68±0.39	0.06±0.05	0.14±0.04	<0.05	0.002	5.0	0.43	0.97	-
E2	20:40-20:43	15900	360	-	1.21±0.56	0.13±0.09	0.22±0.08	<0.05	-	5.5	0.61	0.98	-
F	20:54-20:56	11600	460	361	1.02±0.26	0.09±0.04	0.24±0.07	<0.05	0.002	4.3	0.40	0.96	-
All flights													
PBL	0-4 km	1650±1030	880±630	1260±910	2.77±2.48	0.114±0.140	0.50±0.31	0.43±0.59	0.25±0.21	5.6±6.6	0.23±0.43	0.28±0.19	157±64
MT	5-8 km	2130±3070	410±150	280±170	0.51±0.40	0.035±0.039	0.17±0.30	0.06±0.10	0.005±0.011	3.0±3.6	0.21±0.38	0.79±0.15	96±22
UT	9-15 km	7700±7970	840±440	568±313	1.59±0.91	0.190±0.117	0.115±0.084	0.04±0.09	0.002±0.006	13.8±4.6	1.7±1.2	0.86±0.11	116±39

Figure 1: Tracks of the flights on which measurements at high altitude were made during ACRIDICON-CHUVA. The flight segments at altitudes >8 km are shown as heavier lines.

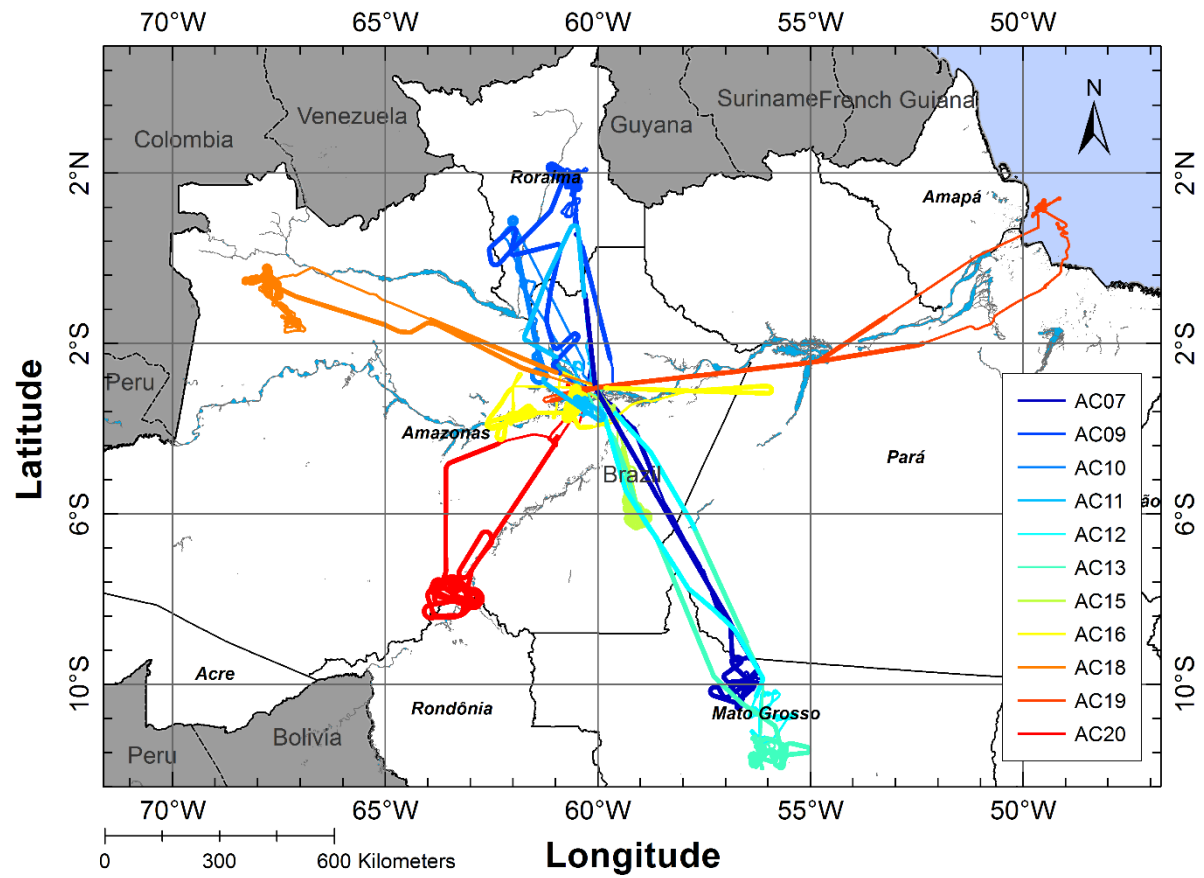


Figure 2: Columnar precipitable water anomaly for September 2014 (based on the 1981-2010 average NCEP/NCAR Reanalysis).

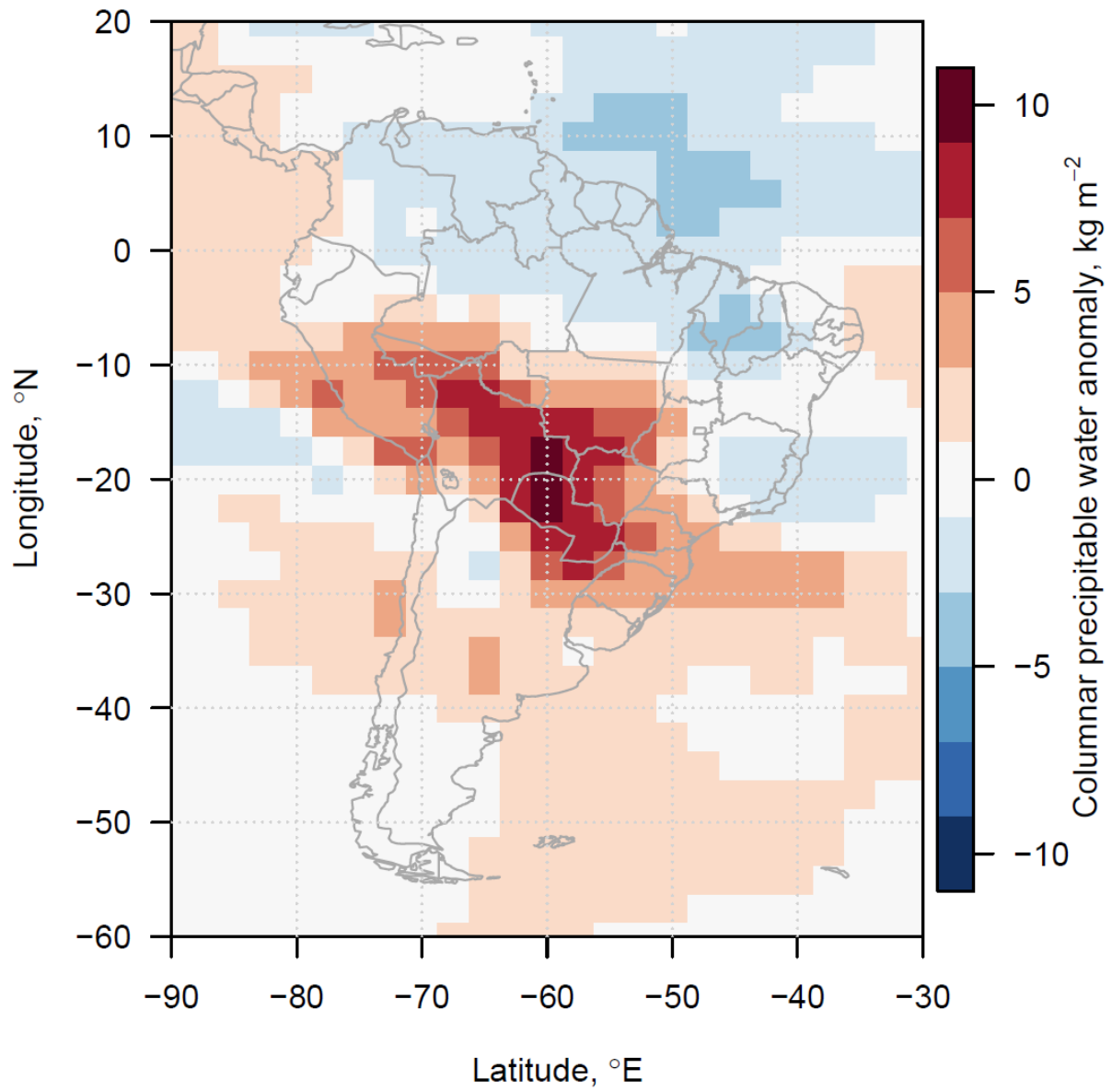


Figure 3: Total rainfall (mm per month, 1° resolution) for September 2014. Data from Global Precipitation Climatology Centre (GPCC).

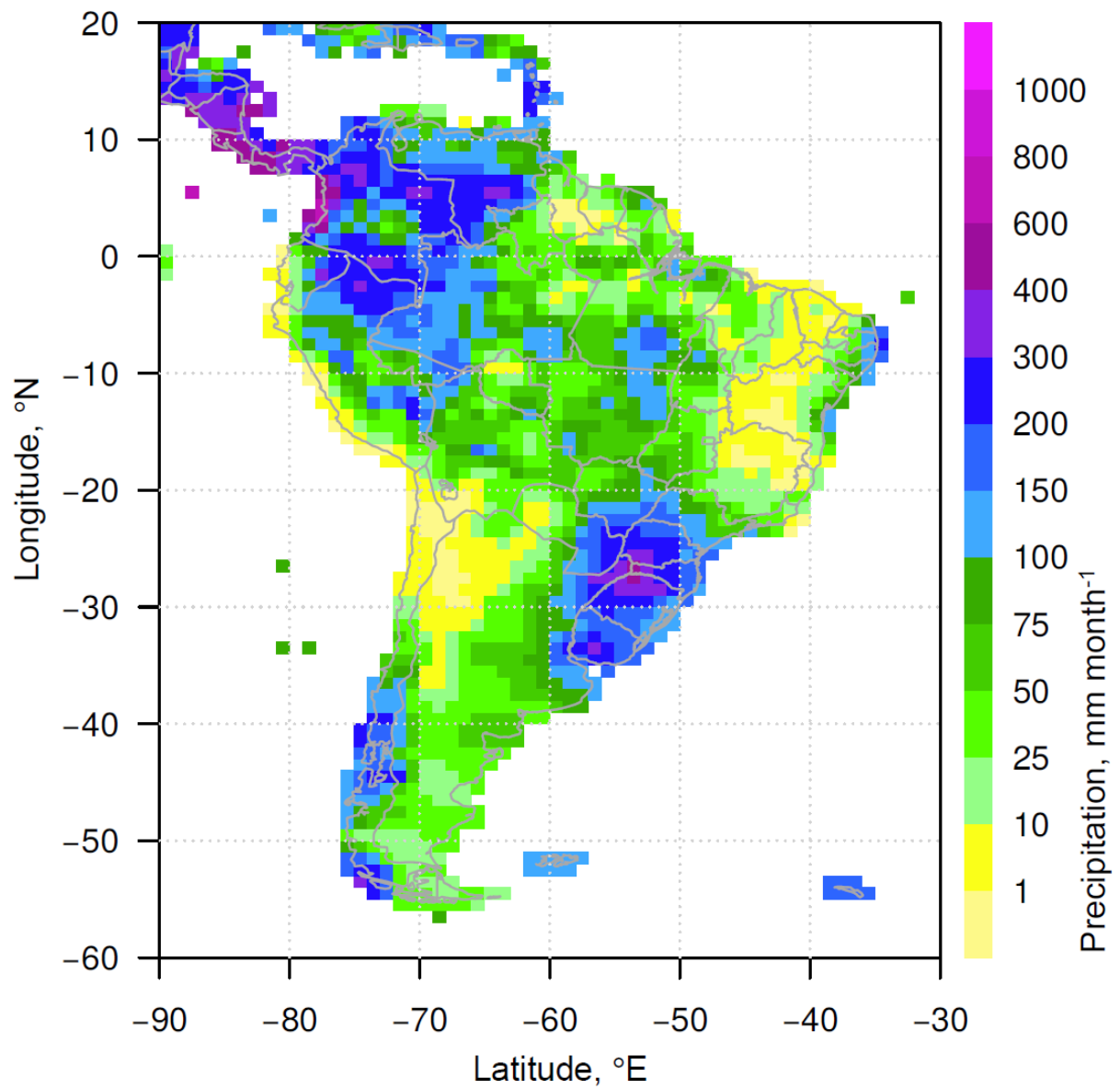


Figure 4: Mean wind speeds during September 2014 at a) 850 hPa and b) 200 hPa (Data from NCEP/NCAR).

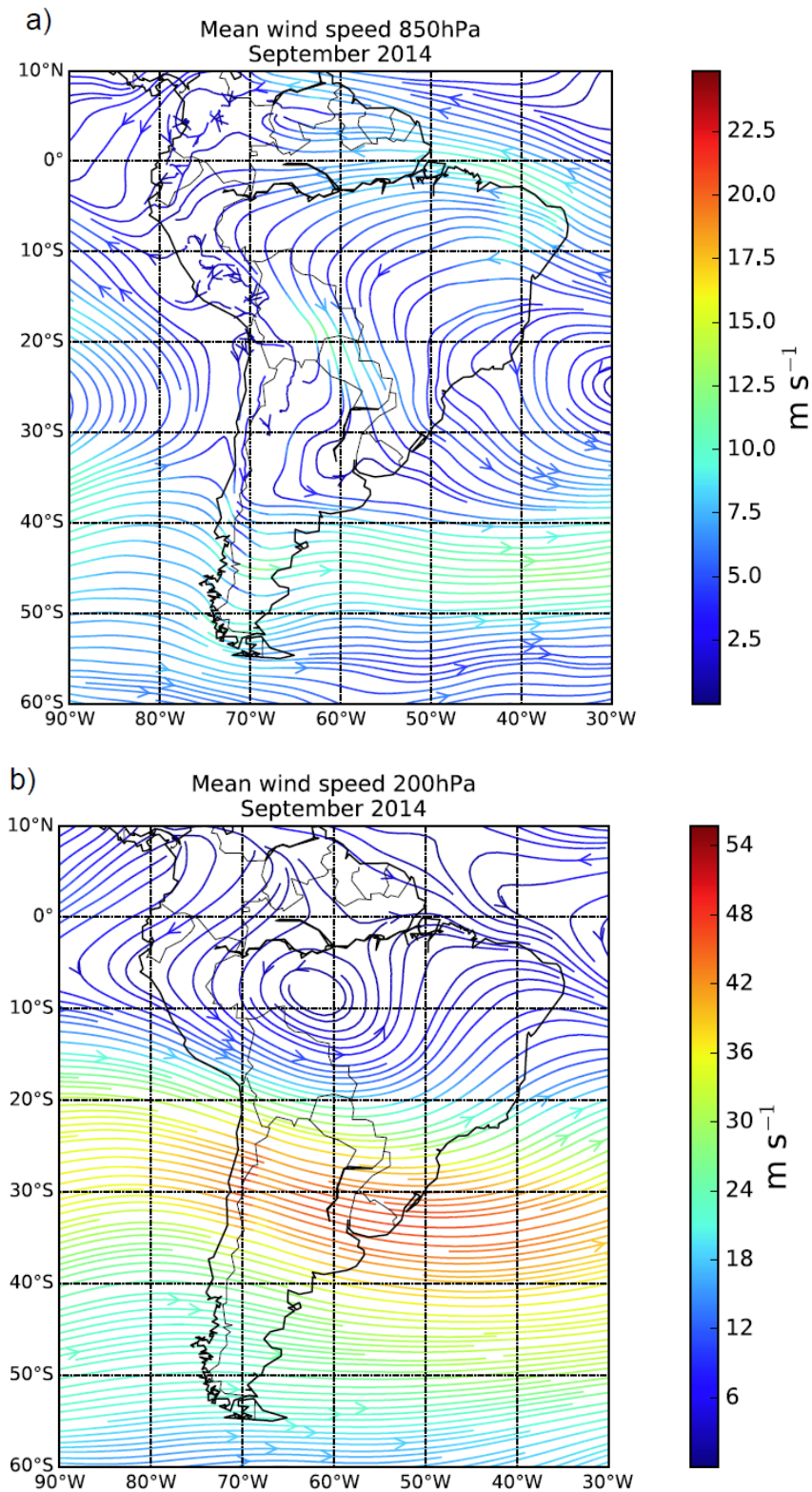


Figure 5: Vertical profiles of potential temperature, static air temperature and relative humidity measured on HALO during the ACRIDICON-CHUVA flights over the Amazon Basin.

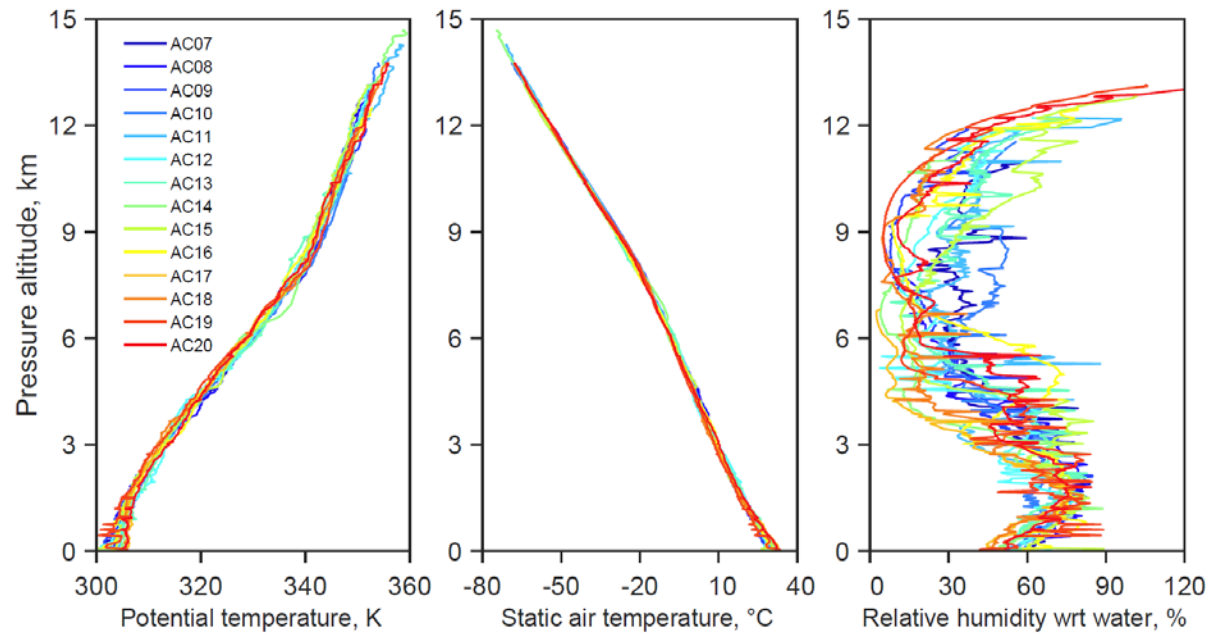


Figure 6: Trajectory statistics based on (a) 72-hour and (b) 120-hour backtrajectory calculations for September 2014, initialized at Manaus at an elevation of 12 km.

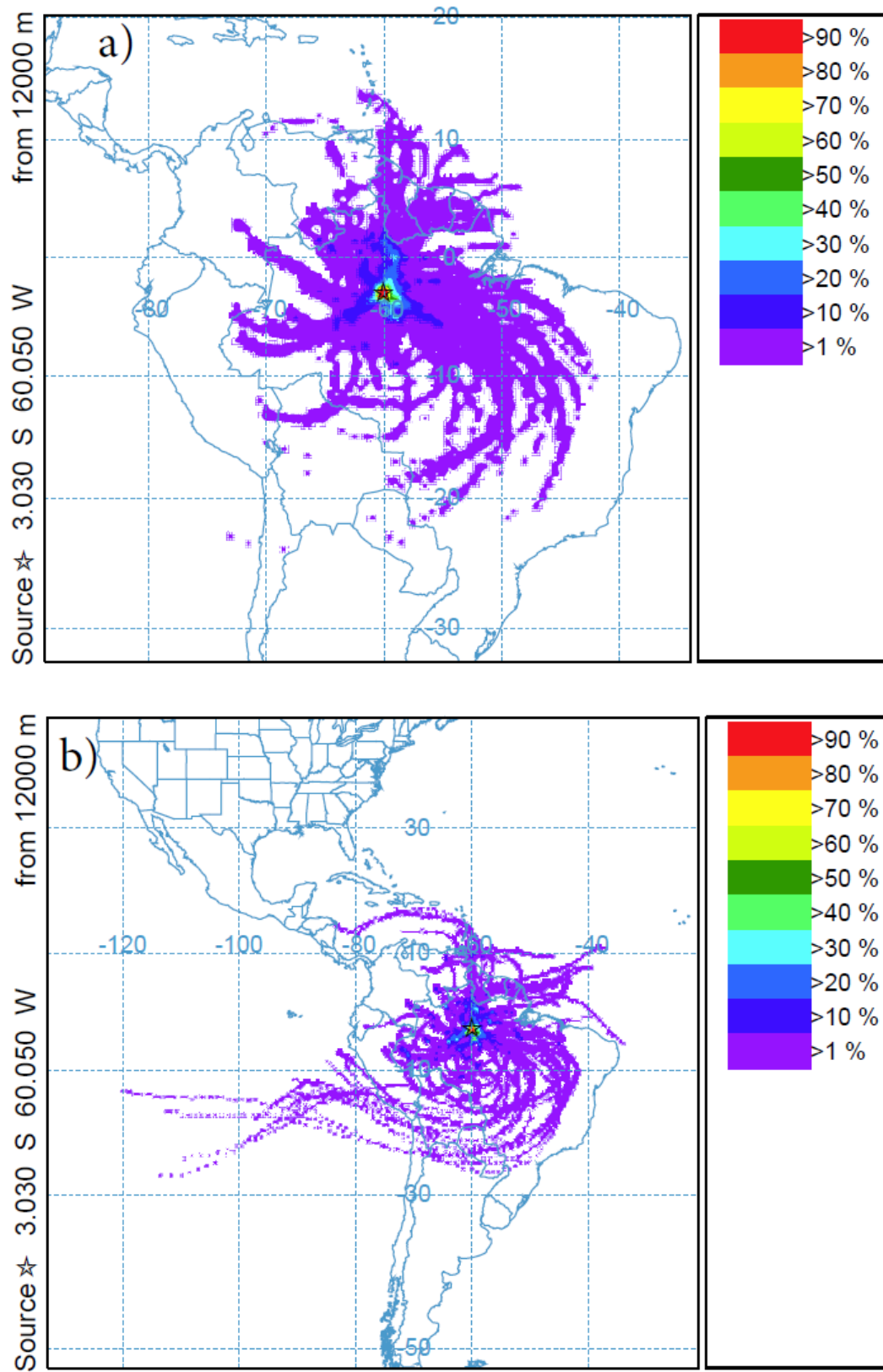


Figure 7: Vertical profiles of CN concentrations, N_{CN} ; a) overall statistics from all flights, b) examples from individual profiles on flight AC07 (segment G) and AC09 (segments A1 and A2).

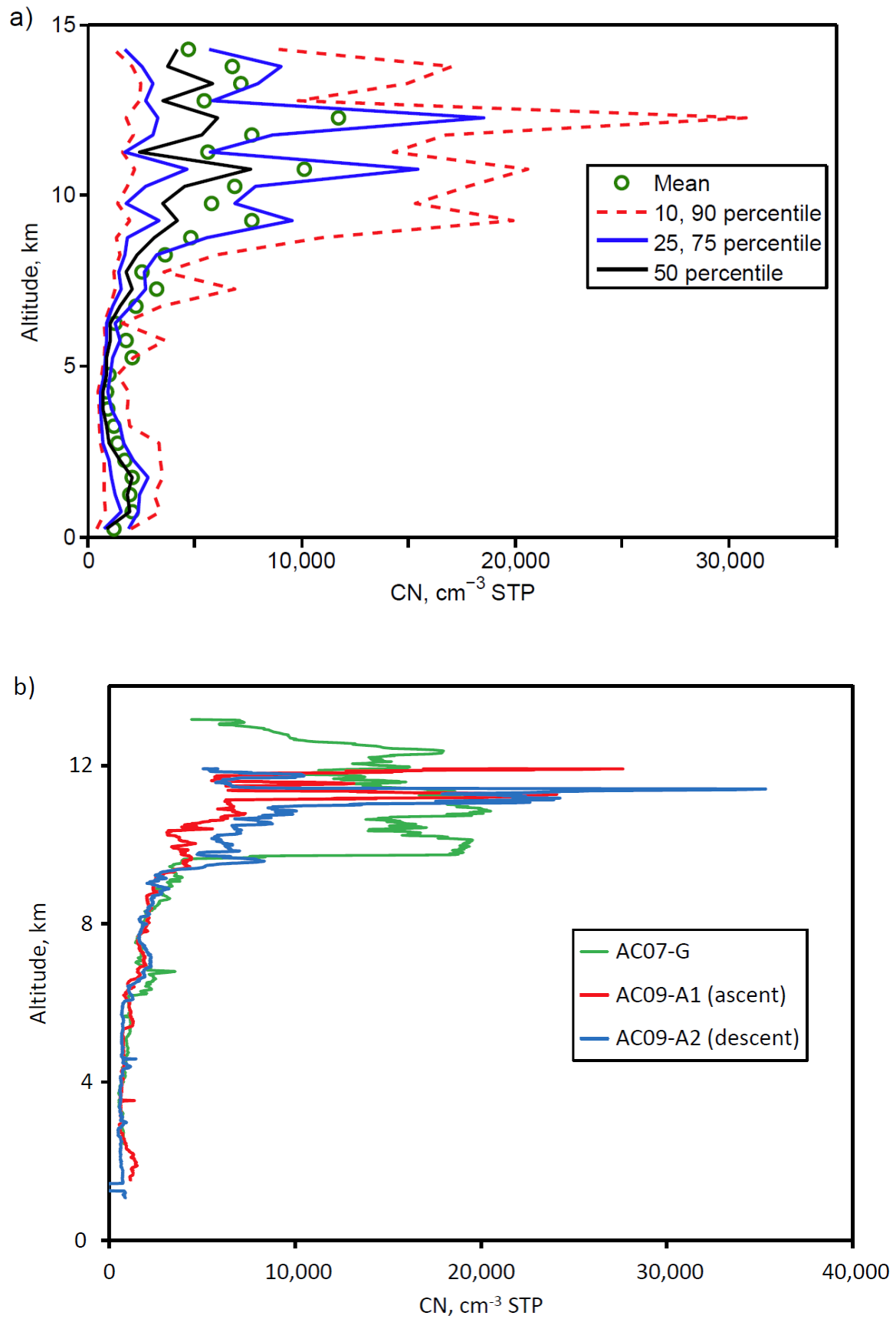


Figure 8: Vertical profiles of accumulation mode particle concentrations, N_{acc} ; a) 1-min averaged data from all flights, b) N_{acc} profile from flight AC19 together with the profile of N_{CN} from the same flight (1-sec data).

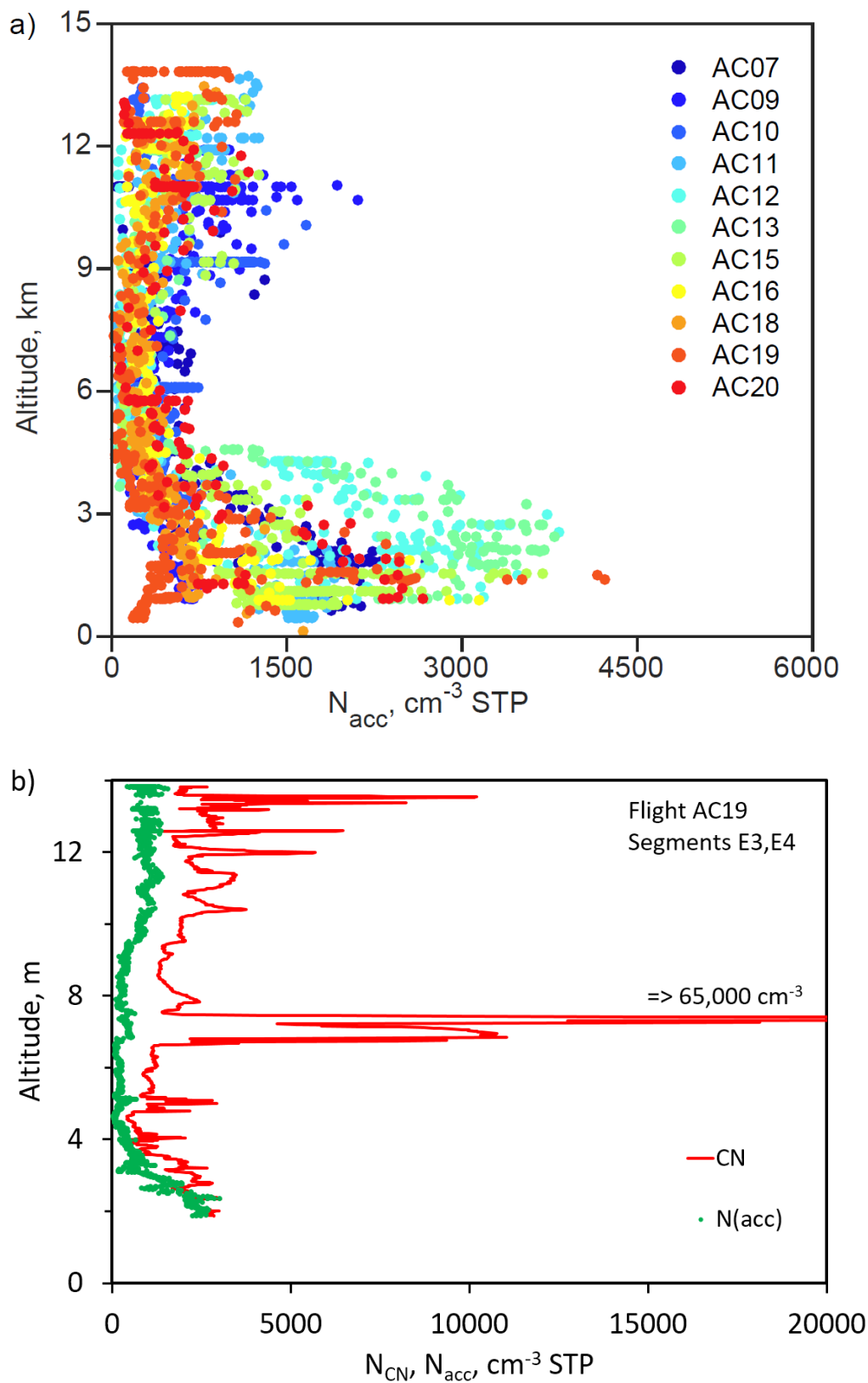


Figure 9: Size spectra: The black line shows the mean boundary layer DMPS size spectrum from a segment in the PBL on flight AC13 (16:55 to 17:18UT). The square black symbols represent the mean, the grey shaded area the standard deviation of the measurements. The line is a logarithmic fit with modal diameters of 74 and 175 nm. The colored lines represent size distributions from 0.65 to 5.8 km from a G1 flight during GoAmazon (Wang et al., 2016a).

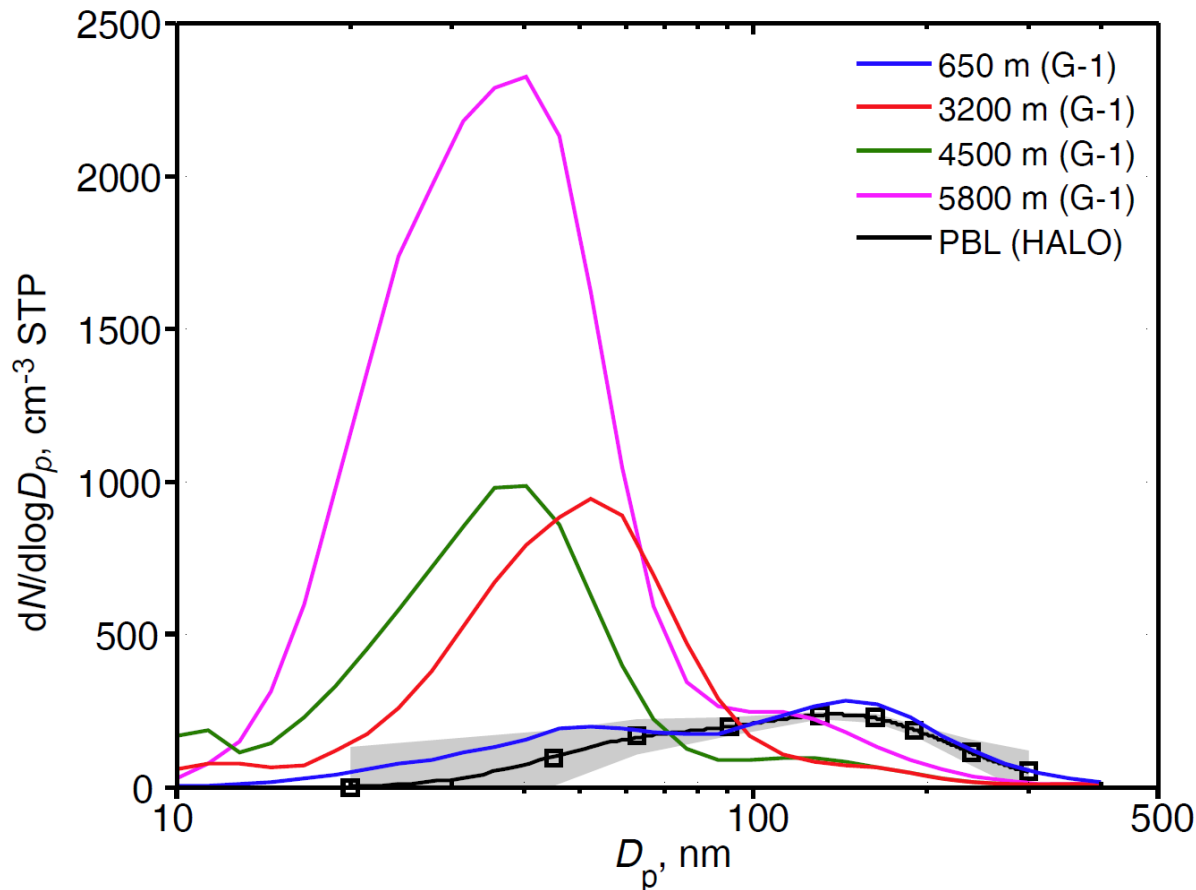


Figure 10: Vertical profiles of the ultrafine fraction (UFF); a) overall statistics from all flights, b) examples from individual profiles on flight AC18.

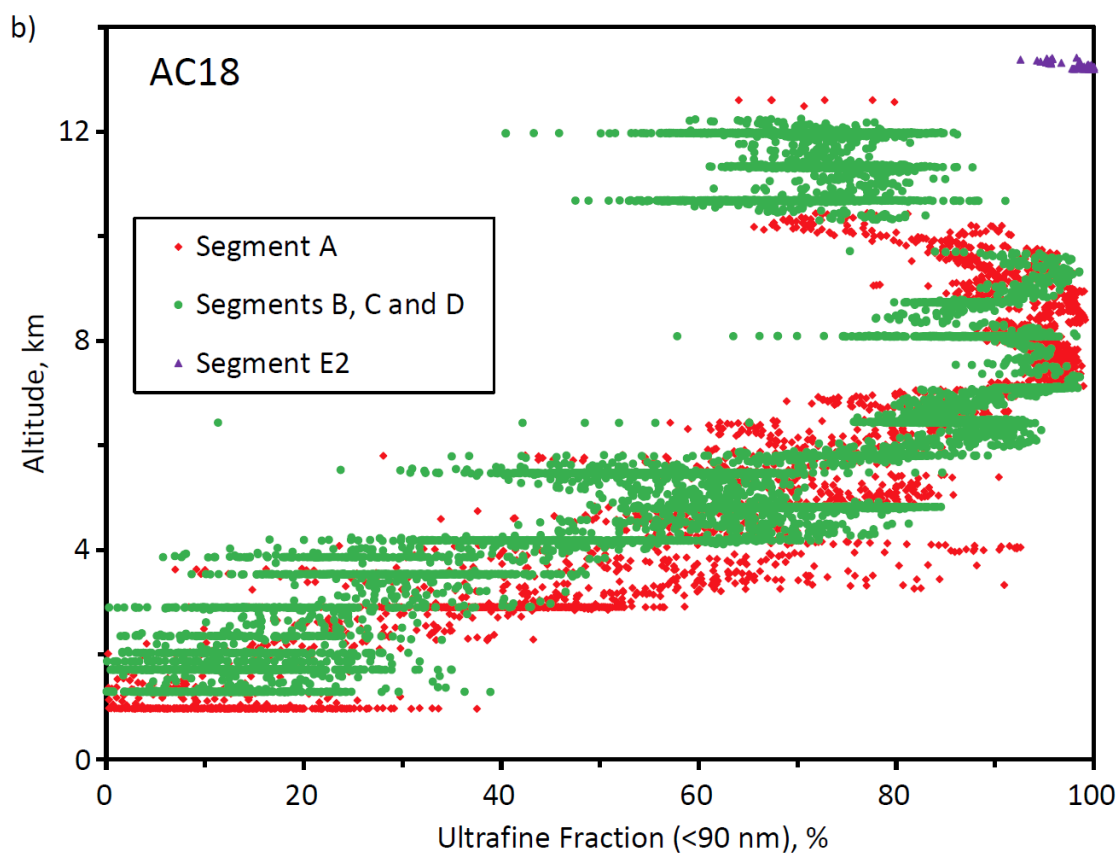
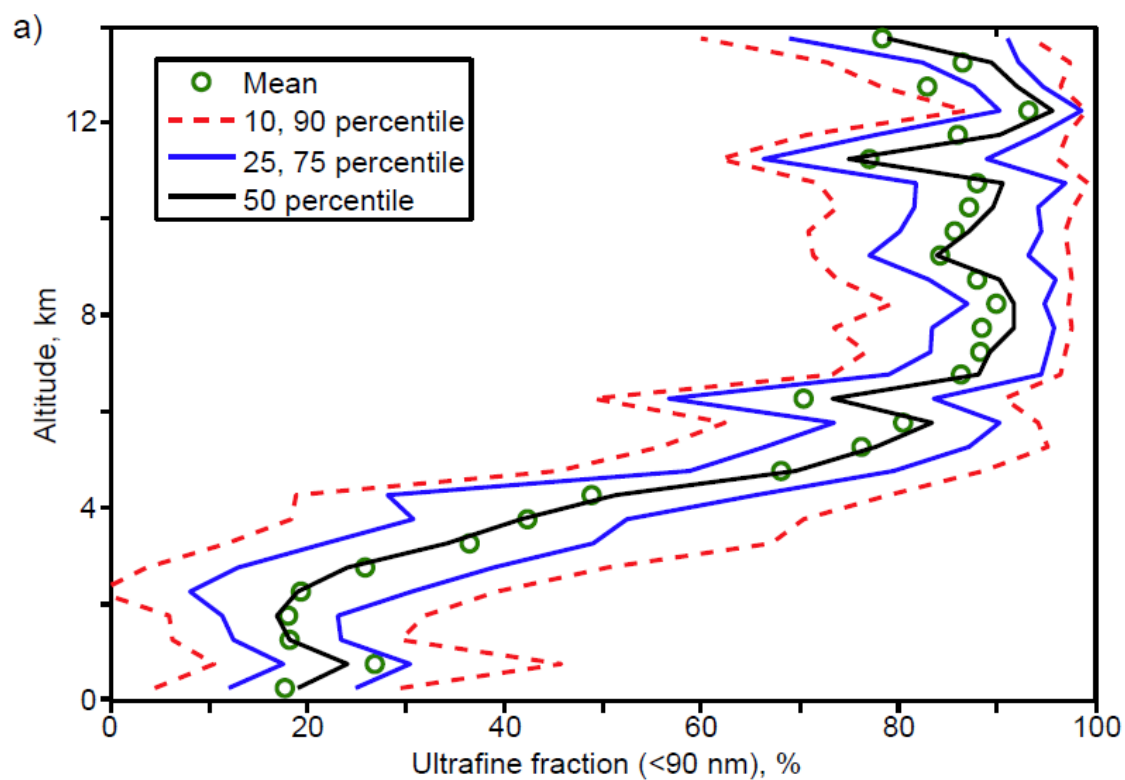


Figure 11: Vertical profiles of CCN concentrations at 0.52% supersaturation; a) overall statistics from all flights (1-min averages), b) examples from individual profiles on flights AC09 (green) and AC12+13 (red). Flights AC12 and AC13 were conducted over the same region on successive days.

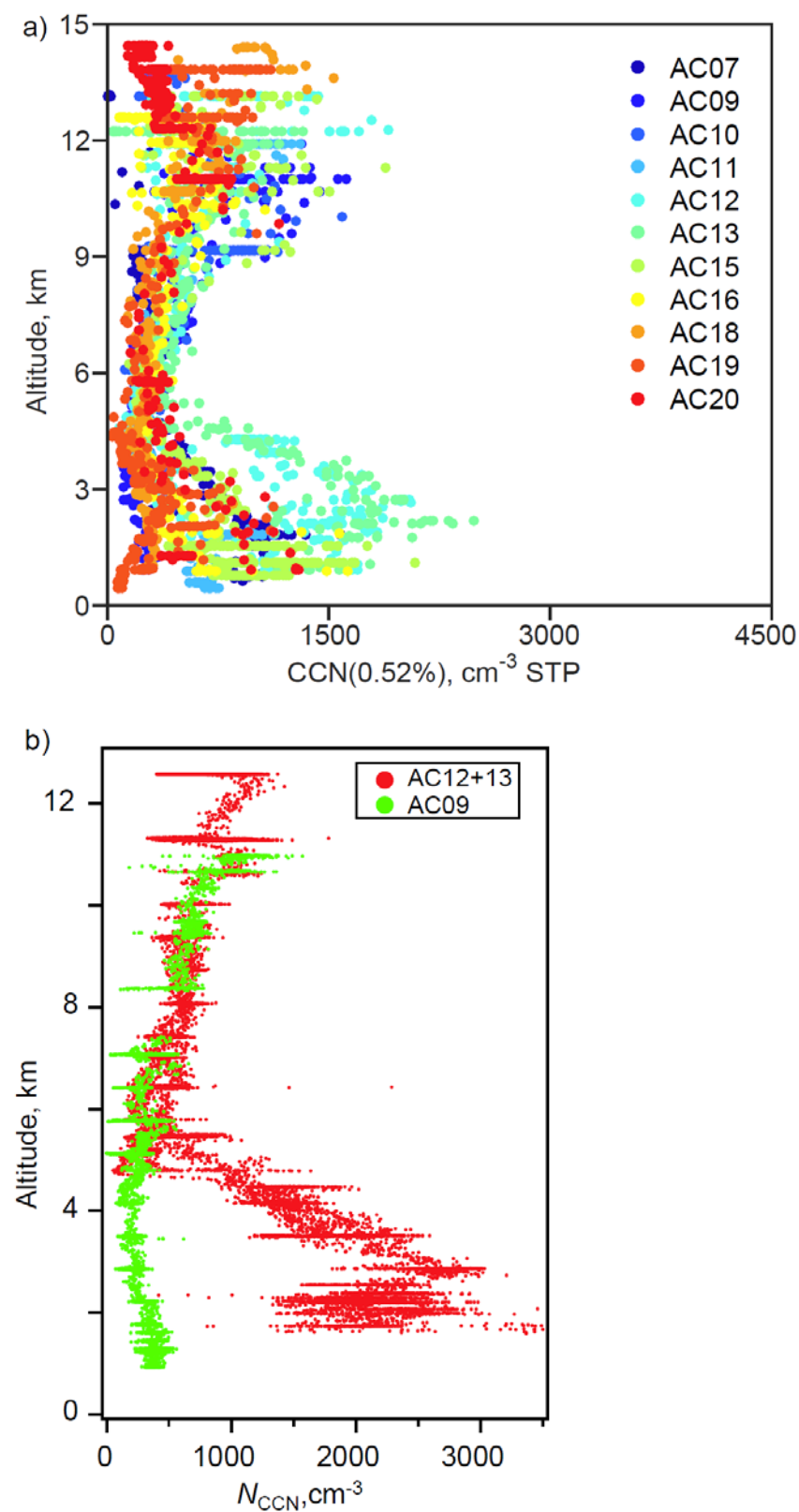


Figure 12: a) CCN fraction vs altitude, all data. The peak at 11 km is caused by the inclusion of a large number of measurements from flight AC20 on a horizontal leg at 11 km, which was influenced by biomass burning (see section 3.6). b) CCN fraction vs. CN concentration for specific segments from flight AC18 (see text).

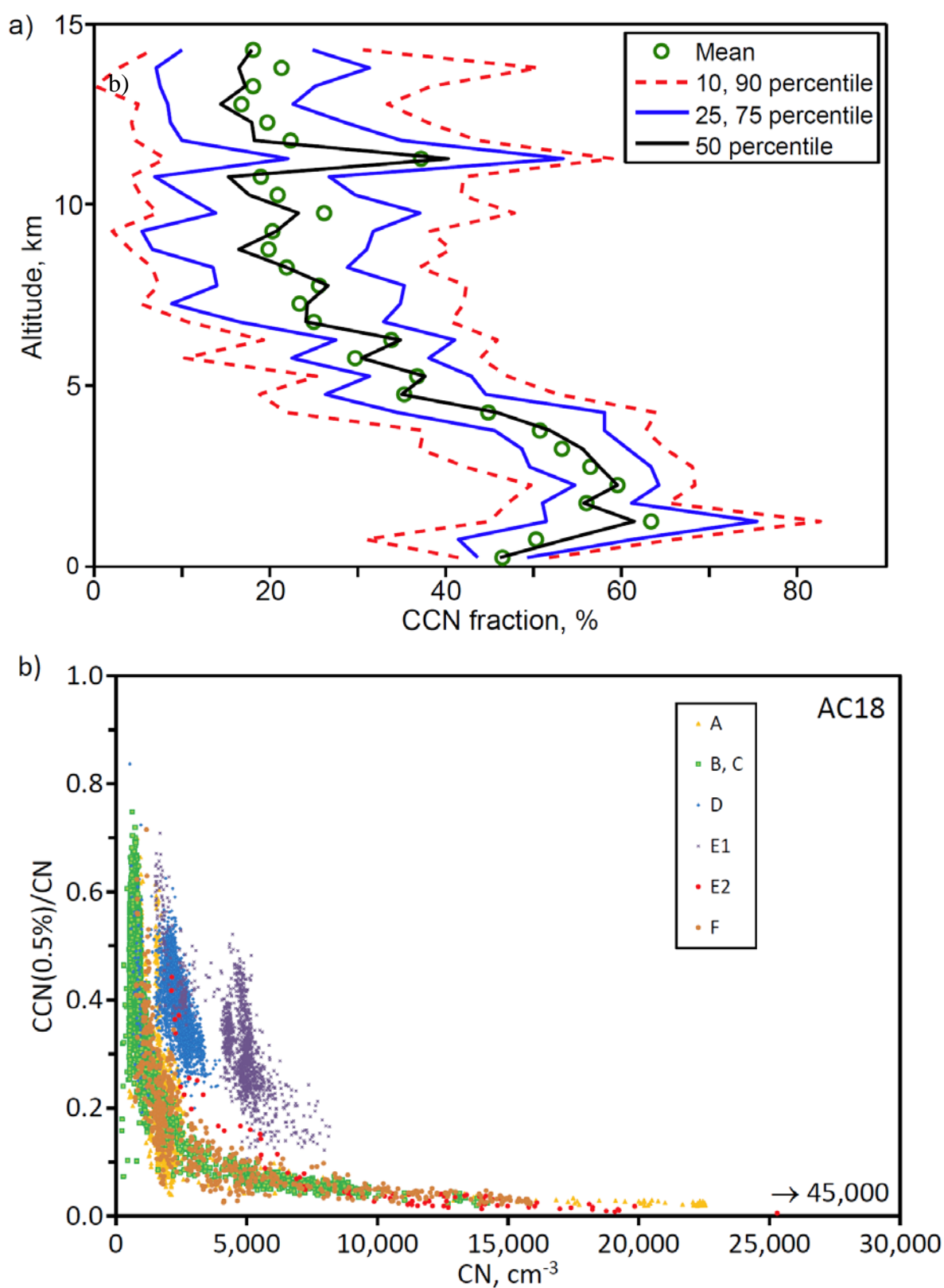
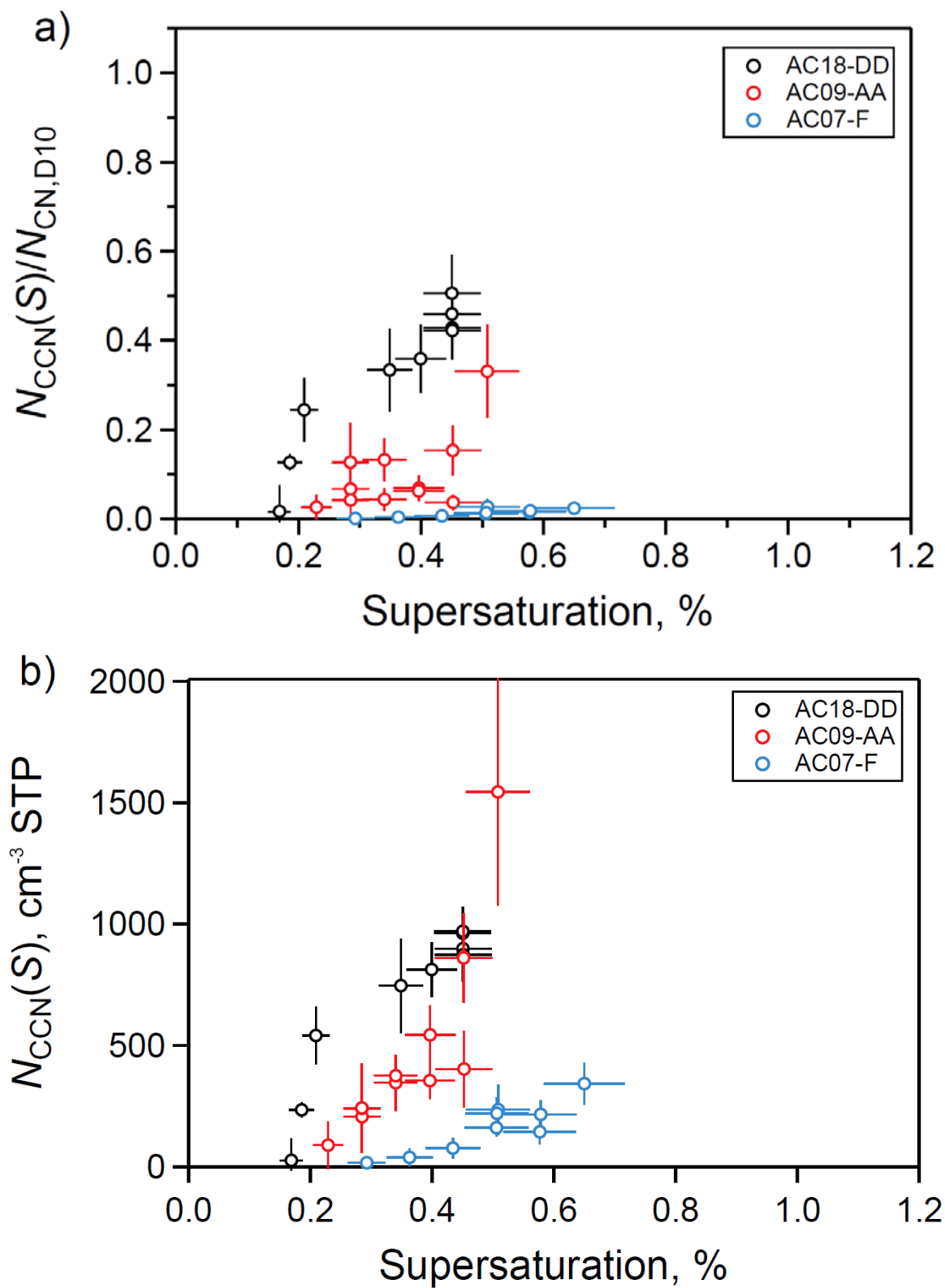


Figure 13: a) CCN fractions ($N_{CCN0.5}/N_{CN}$) and b) CCN concentrations ($N_{CCN0.5}$) vs. supersaturation from selected legs from flights AC07, AC09, and AC18; c,d) data from flights AC12 and AC13 for the LT, MT, and UT.



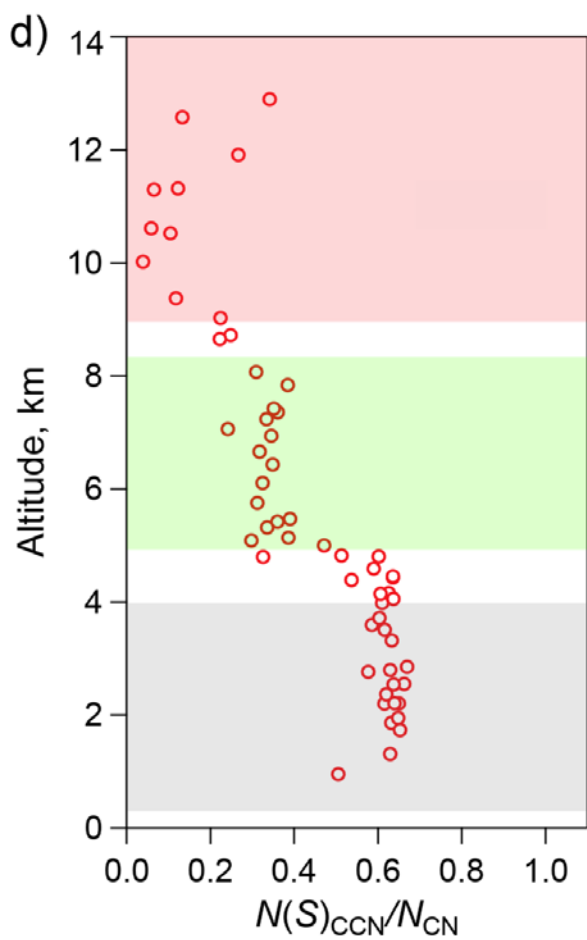
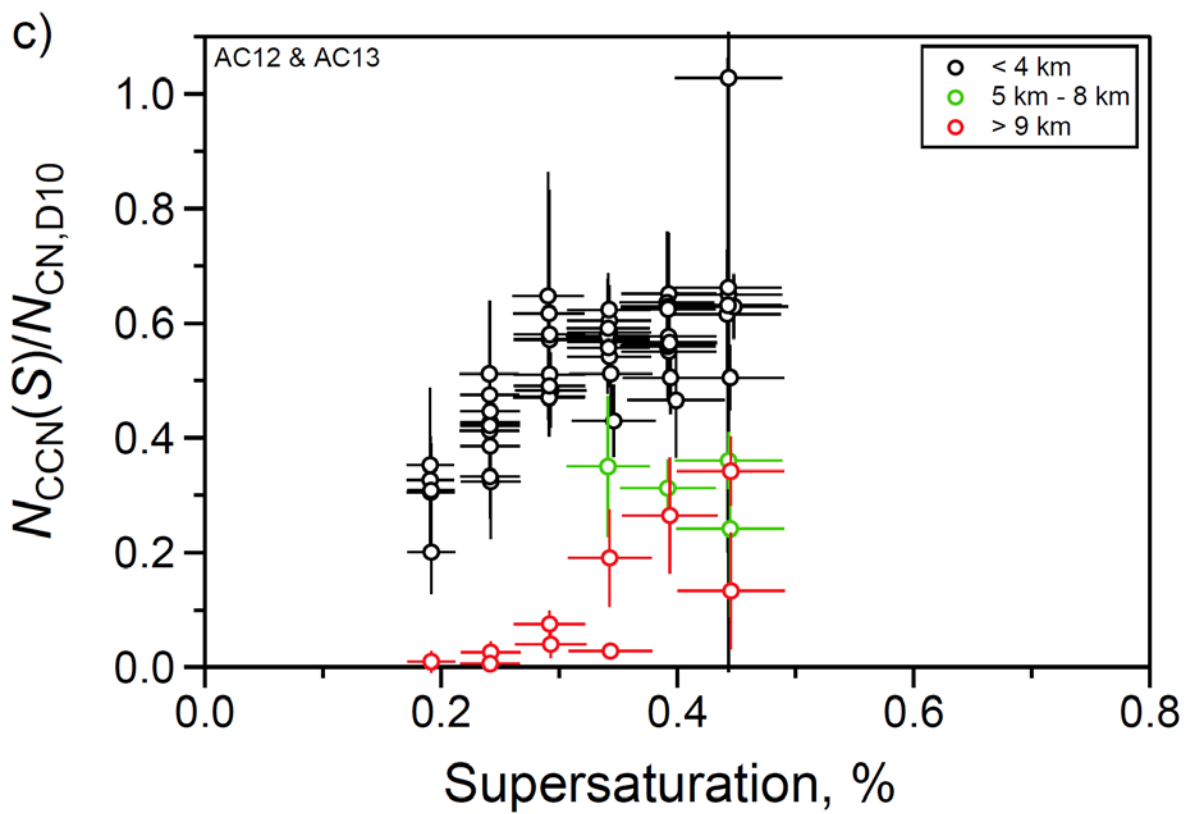


Figure 14: Volatile fraction. a) statistics from all flights; b) individual segments from flight AC18 (see text)

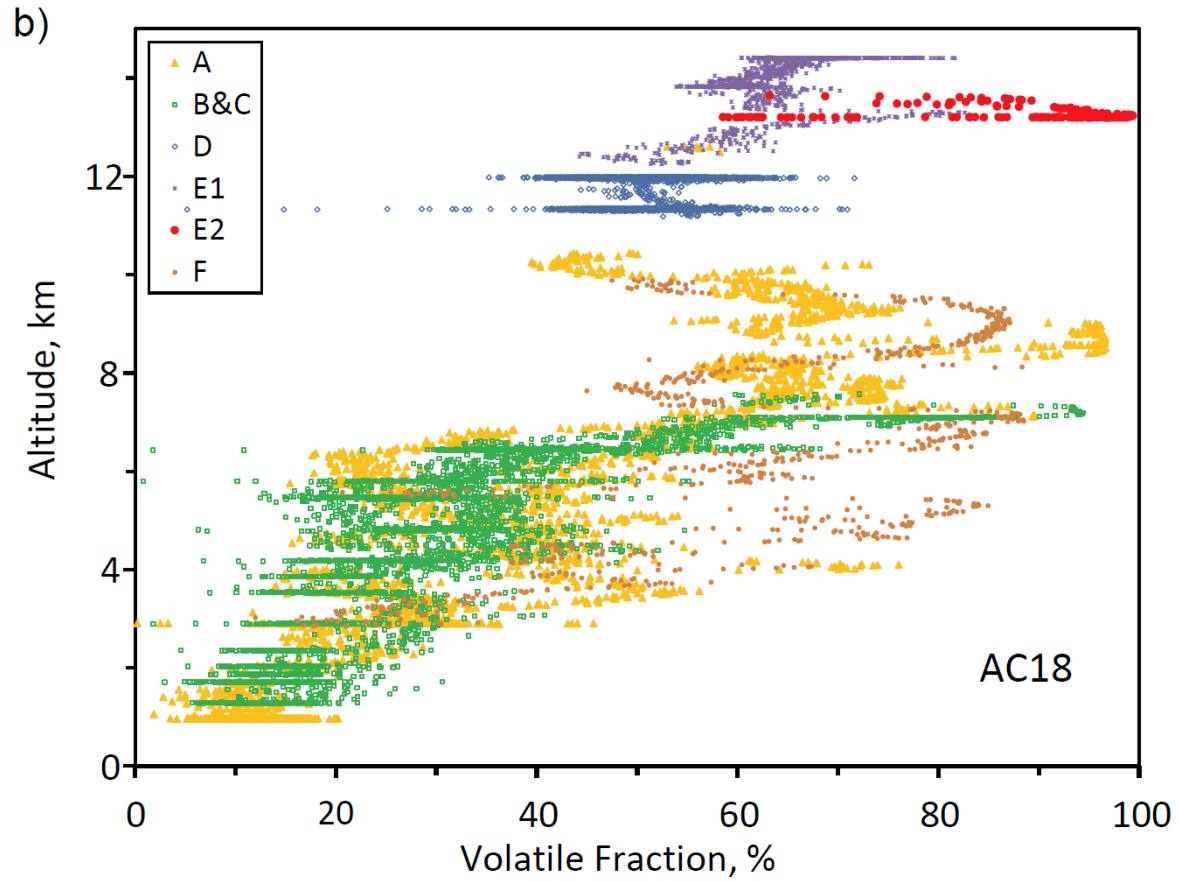
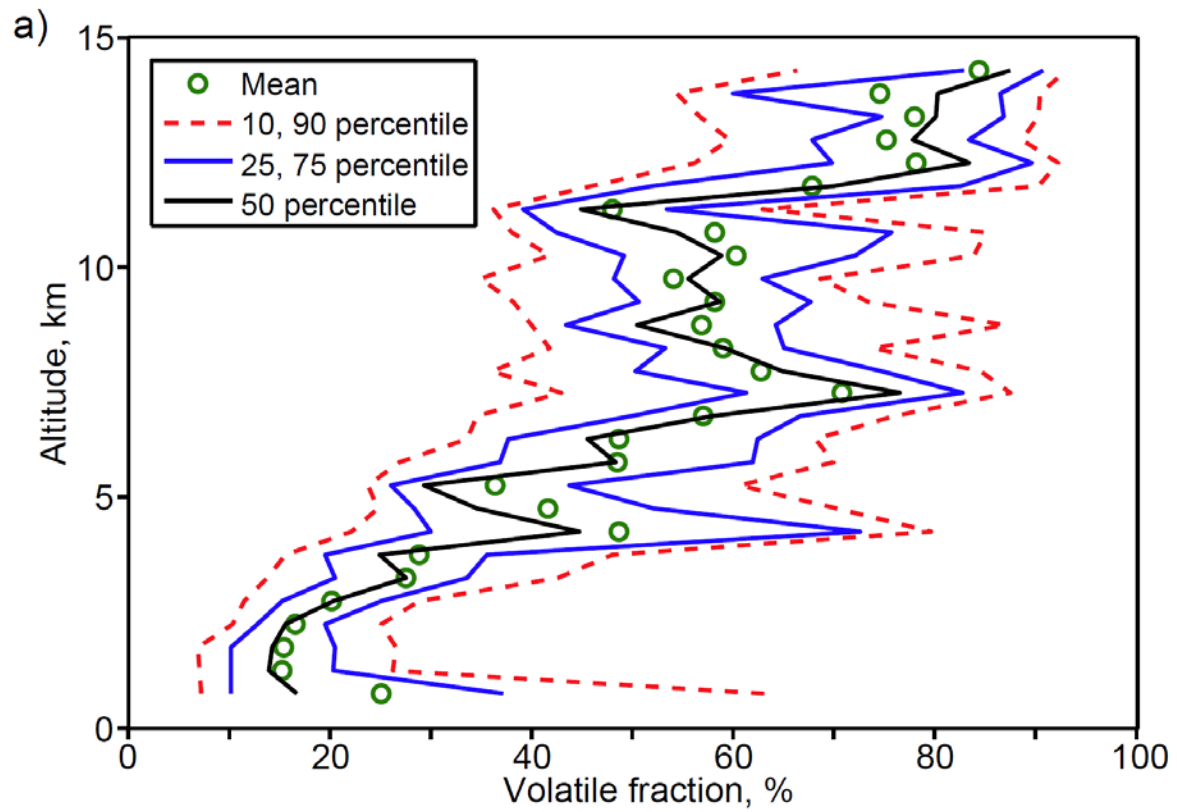


Figure 15: Refractory black carbon vs altitude, all flights, 30-second averages.

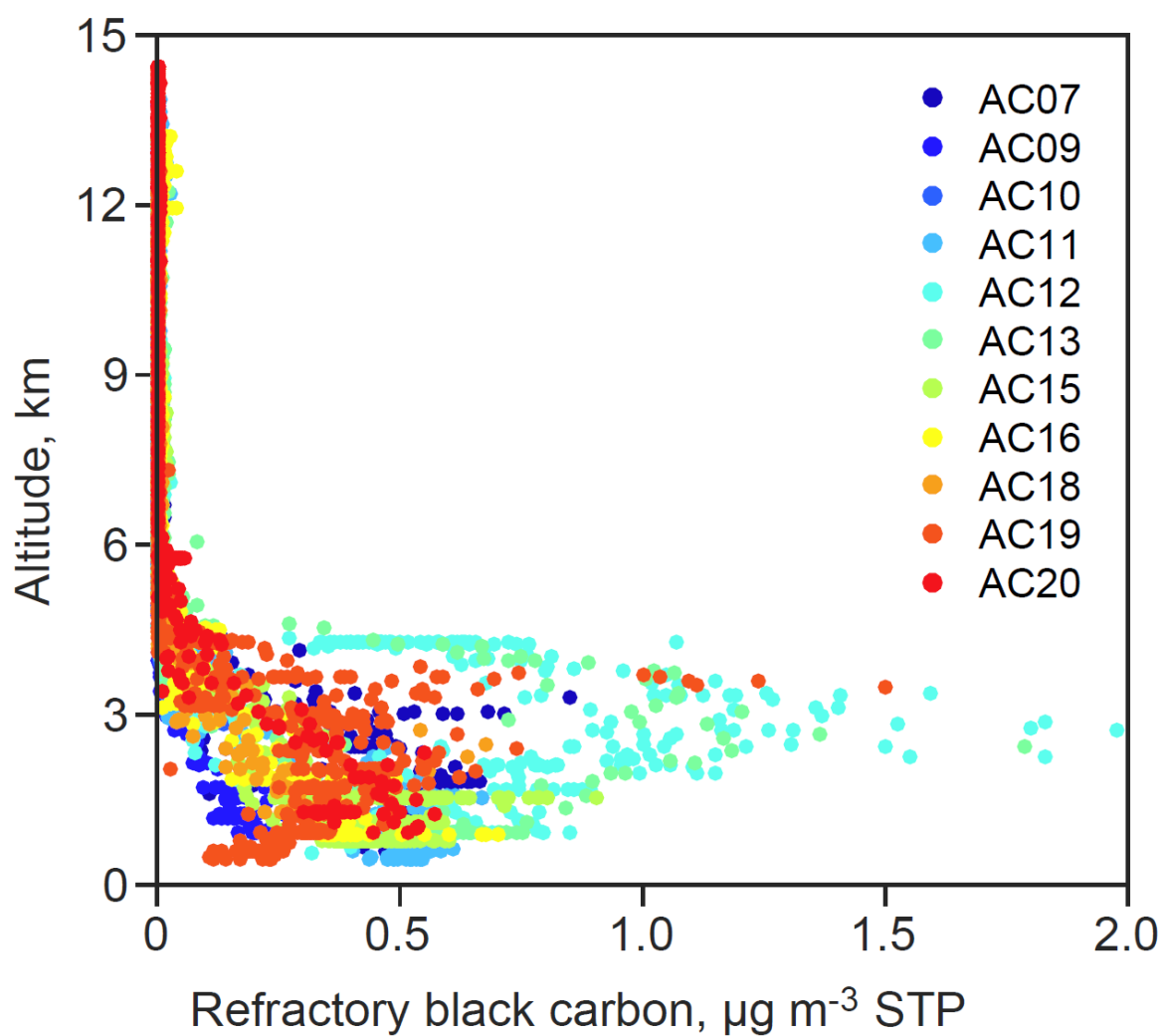


Figure 16: Aerosol chemical composition as determined by AMS and SP2 measurements in the lower, middle and upper troposphere.

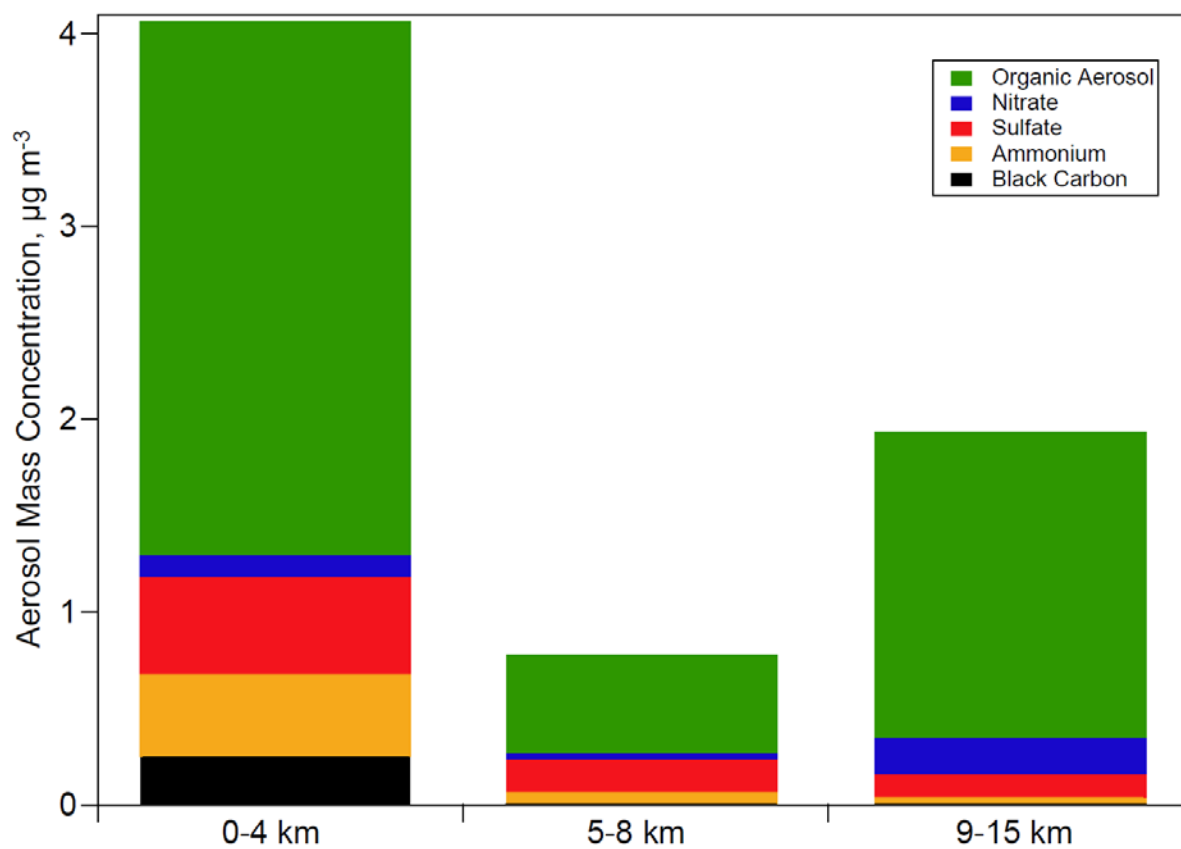


Figure 17: Plot of the AMS factors f_{44} vs. f_{43} , indicating the median values for the LT and UT and values for some UT flight segments with elevated aerosol concentrations. With increasing degree of oxidation, the measurements move to the upper left of the triangle

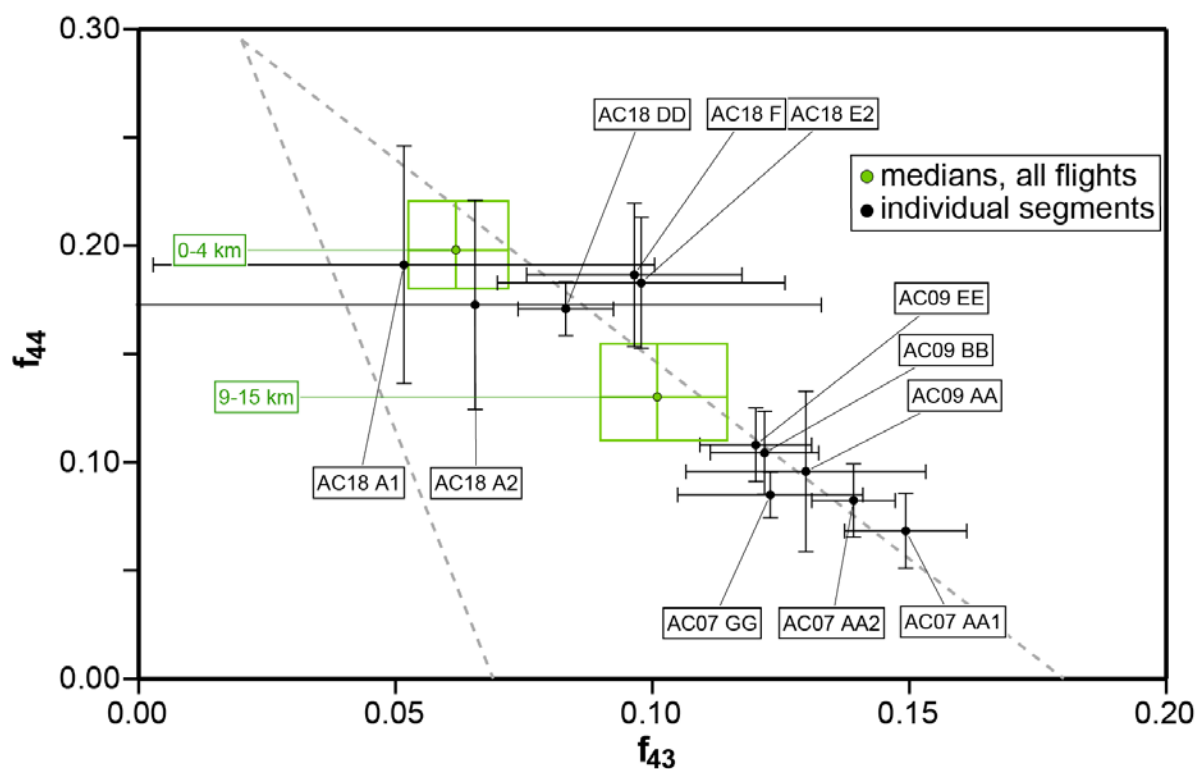


Figure 18: Measurements during passages through cumulonimbus cloud tops and outflow anvils: a) Several cloud top penetrations at 10.7 to 12 km altitude on flight AC18 showing reduced N_{CN} and $N_{CCN0.5}$ inside the cloud top; b) Outflow from a large active cumulonimbus, showing strong aerosol depletion and NO production by lightning.

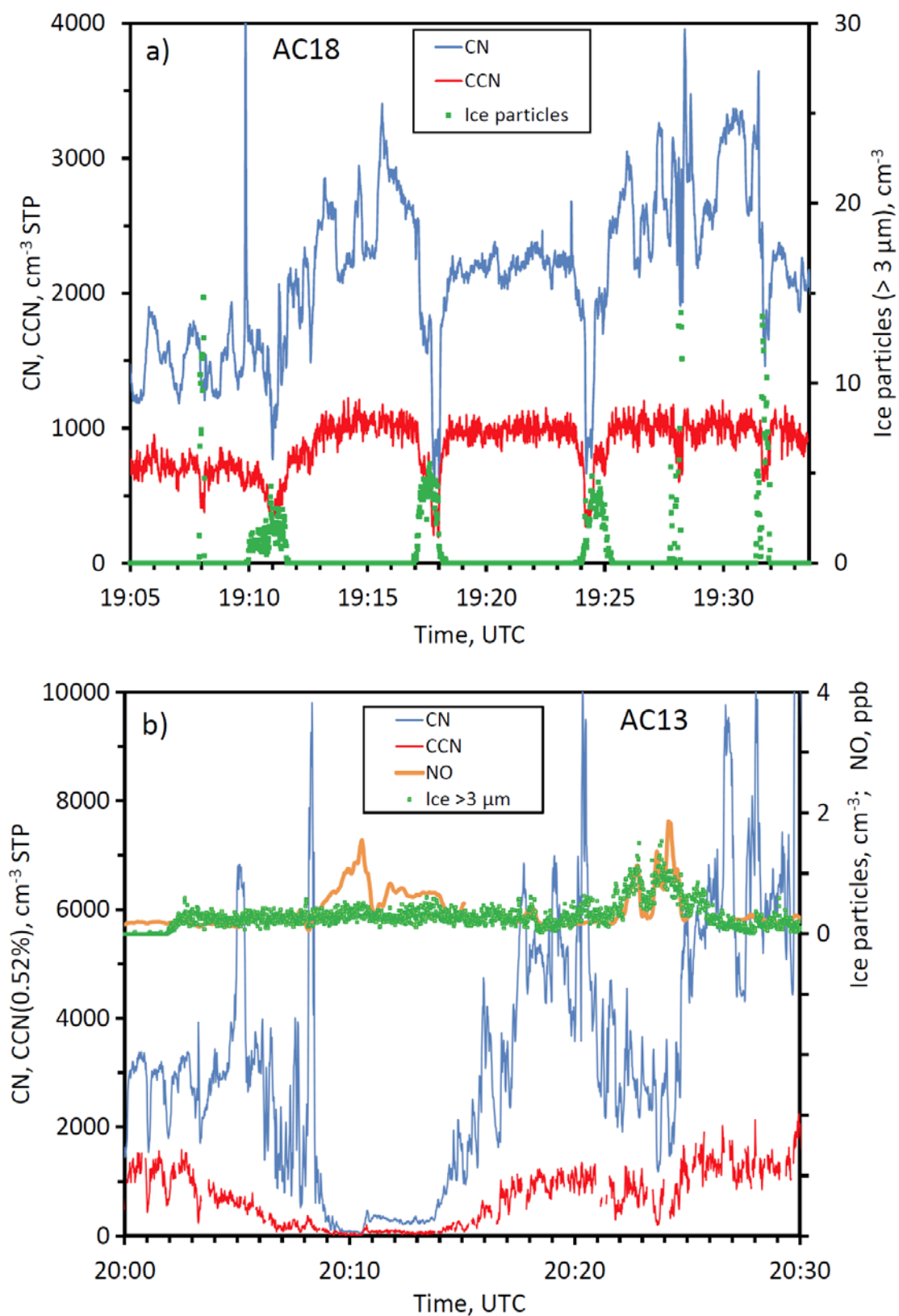


Fig. 19: Airmass contacts with deep convection. The colors indicate the cloud top temperature of the convective system with which the trajectory had the most recent contact. The aircraft altitude at which the airmass was sampled is indicated by the red line. The colored dots are plotted at the altitude at which the airmass crossed the grid cell with the convective system. The dots are only plotted if this altitude is greater than 6 km and if it encountered a DC (i.e., $T_b < -30$ °C). The shaded areas correspond to the flight segments with elevated CN concentrations. a) flight AC09, b) flight AC18.

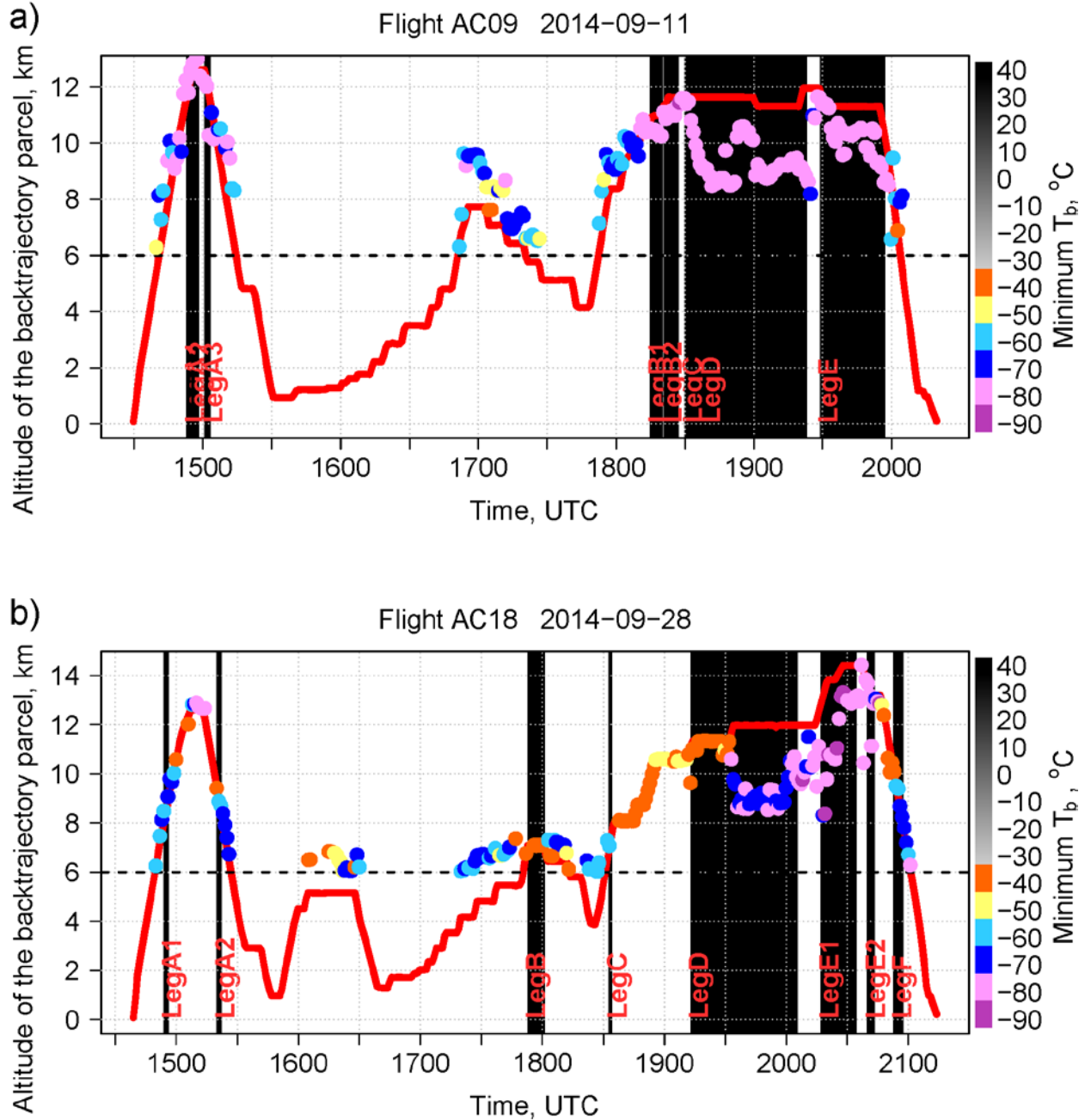
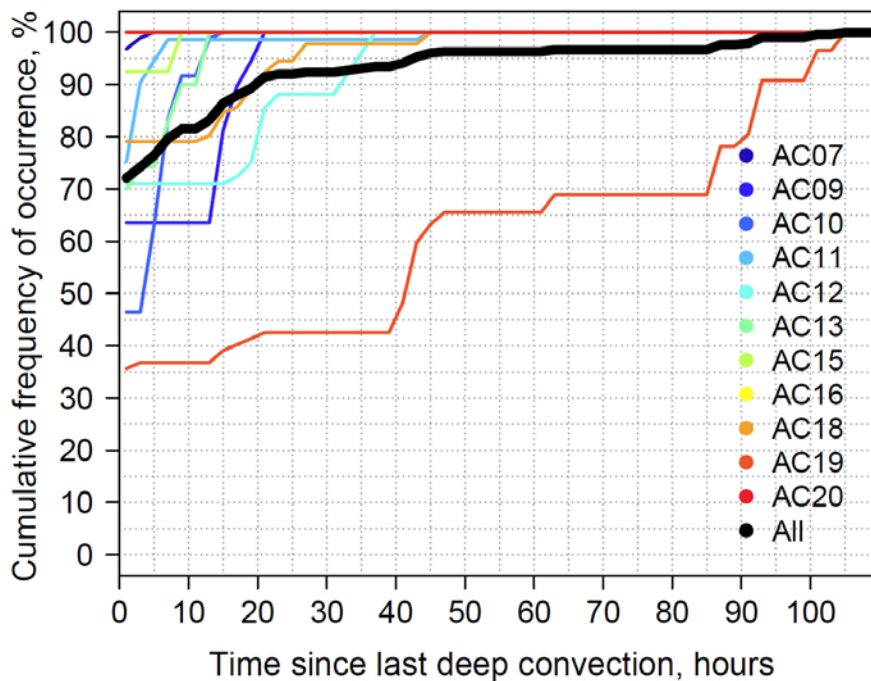


Figure 20: a) Number of hours since last contact with deep convection for flight segments with elevated aerosol concentrations (cumulative frequency, all flights); b) frequency distribution of minimum GOES brightness temperature (T_b) for selected flights legs (within -5 days backward trajectories).

a)



b)

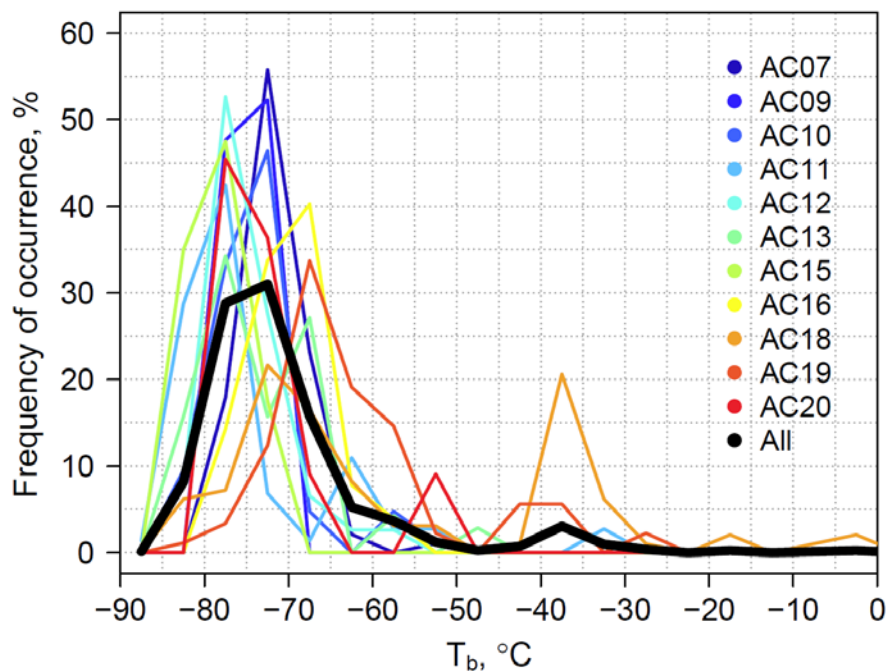


Figure 21: CN vs CO in the upper troposphere above 8 km (15-second averages).

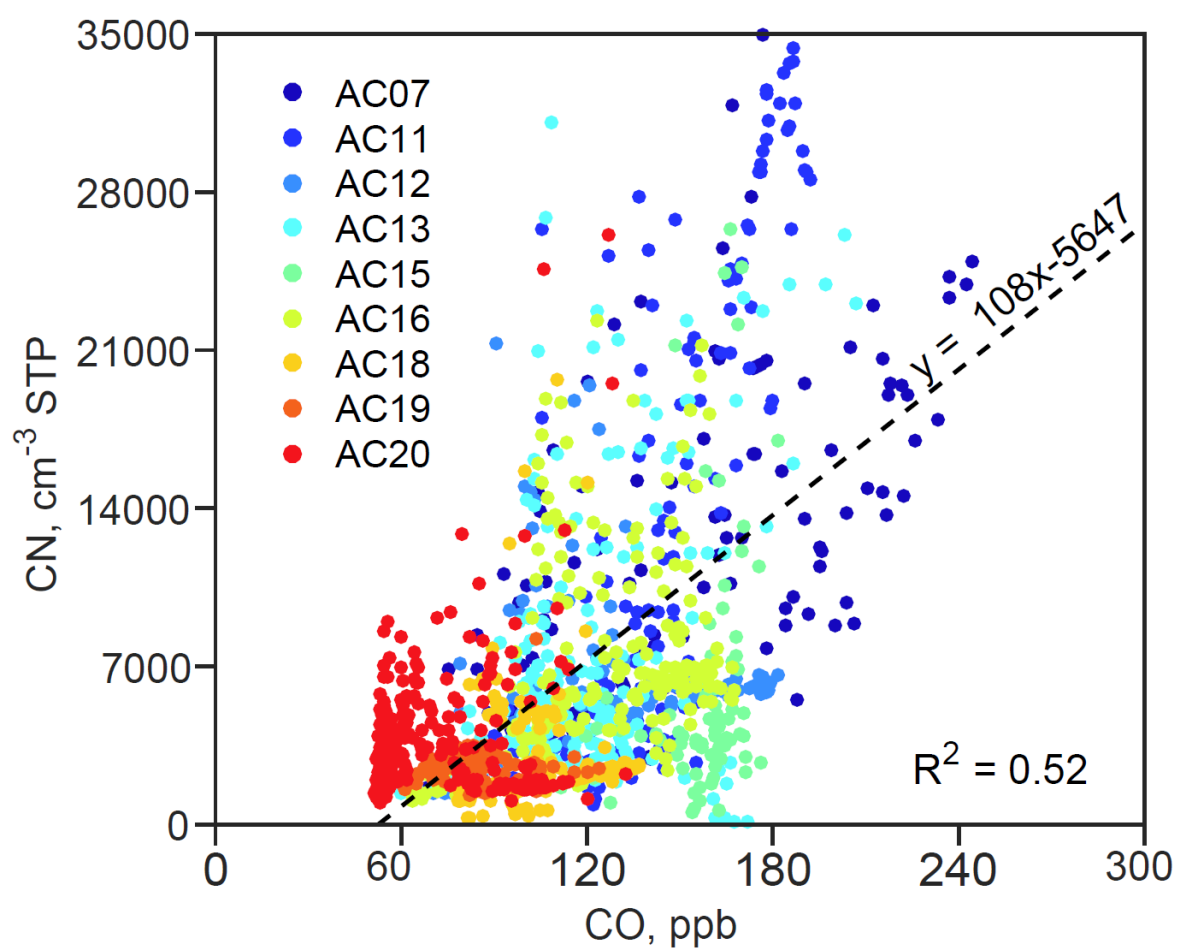


Figure 22: CN, NO and NO_y in a flight segment in the upper troposphere on flight AC07.

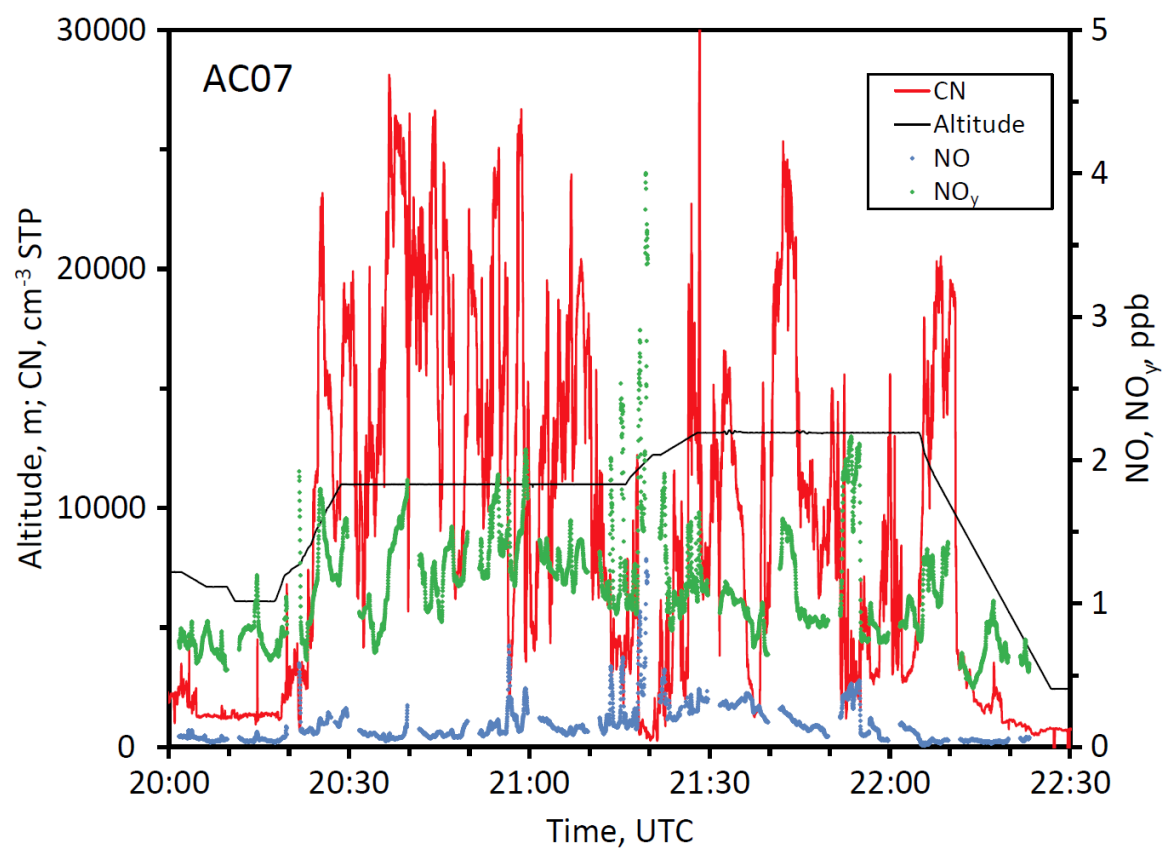
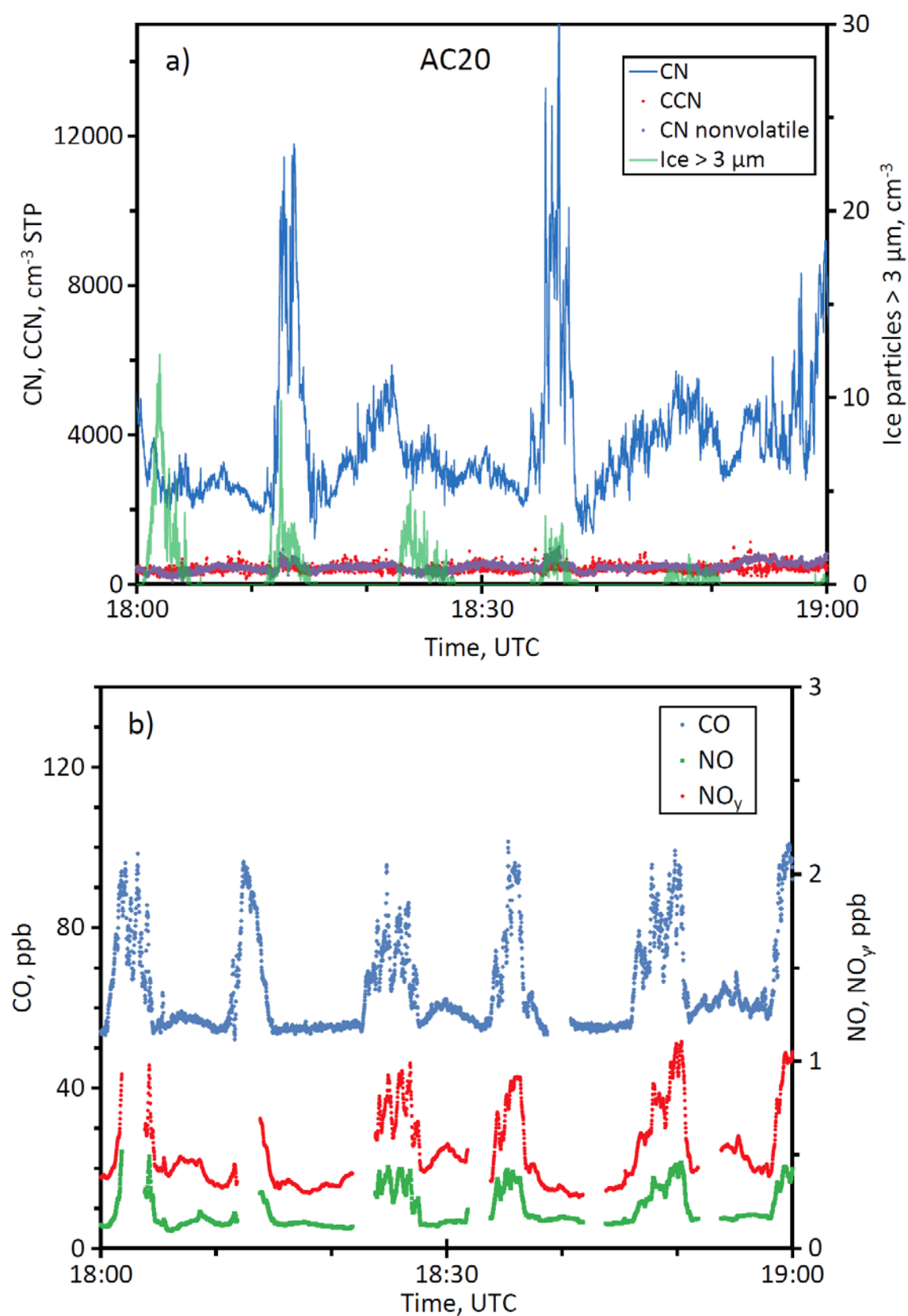


Figure 23: a) Measurements of $N_{CCN0.5}$, N_{CN} , N_{nonvol} , and ice particles during cloud top penetrations on flight AC20 at altitudes between 12.3 and 13.5 km. b) Concentrations of CO, NO, and NO_y on the same flight segments. c) Measurements of N_{acc} , N_{CN} , rBC, CO, and O_3 during the climb from 11.0 to 13.5 km.



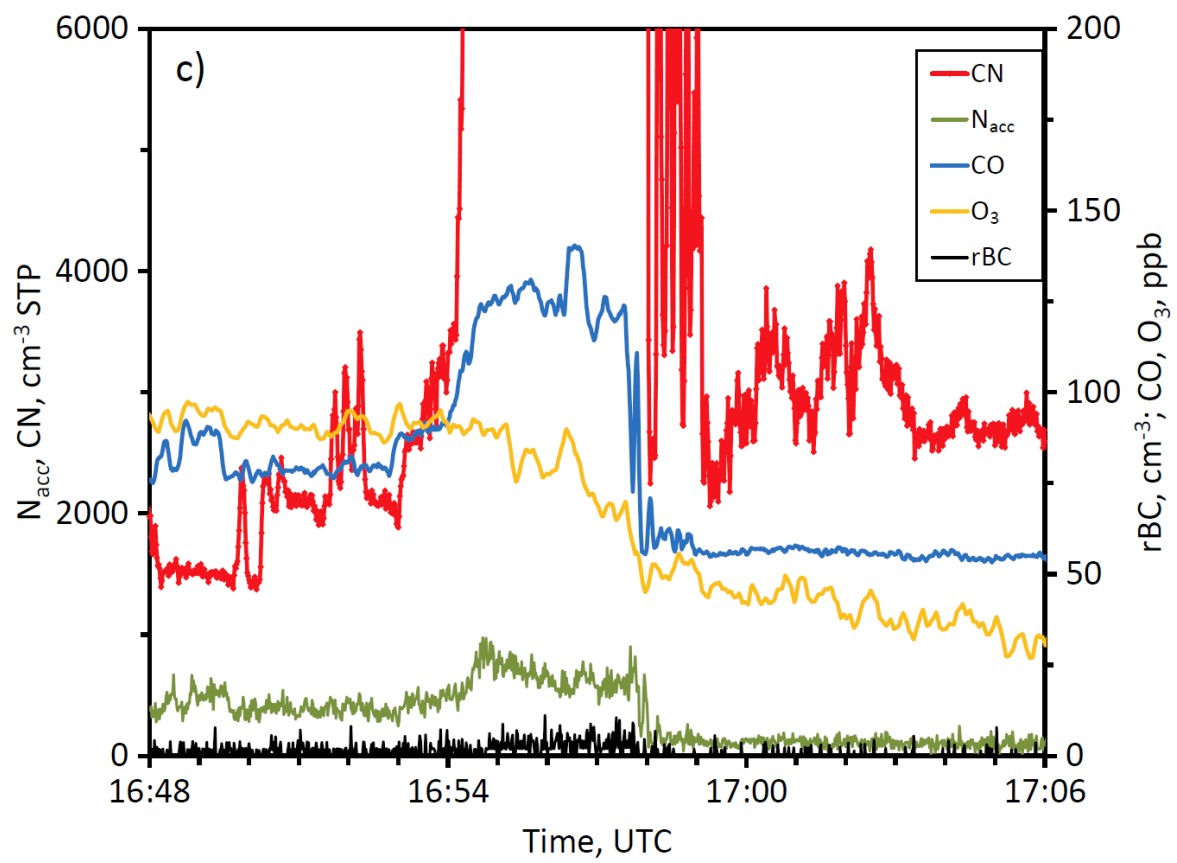


Figure 24: Conceptual model of the aerosol life cycle over the Amazon Basin

